HIGH-PERFORMANCE GE/GESN PHOTODETECTORS IN NEAR- AND MID-INFRARED RANGE

SON BONGKWON

SCHOOL OF ELECTRICAL & ELECTRONIC ENGINEERING

2021

HIGH-PERFORMANCE GE/GESN PHOTODETECTORS IN NEAR- AND MID-INFRARED RANGE

SON BONGKWON

School of Electrical & Electronic Engineering

A thesis submitted to the Nanyang Technological University
in partial fulfilment of the requirement for the degree of
Doctor of Philosophy

2021

Statement of Originality

I hereby certify that the work embodied in this thesis is the result of original research, is free of plagiarised materials, and has not been submitted for a higher degree to any other University or Institution.

30 Jul 2021

Date

Son Bongkwon

Supervisor Declaration Statement

I have reviewed the content and presentation style of this thesis and declare it is free of plagiarism and of sufficient grammatical clarity to be examined. To the best of my knowledge, the research and writing are those of the candidate except as acknowledged in the Author Attribution Statement. I confirm that the investigations were conducted in accord with the ethics policies and integrity standards of Nanyang Technological University and that the research data are presented honestly and without prejudice.

30 Jul 2021

. . . .

Date

. . . .

A/P Tan Chuan Seng

Authorship Attribution Statement

This thesis contains material from three papers published in the following peer-reviewed journals and from one paper accepted at conferences in which I was the first author.

Chapter 3 is published as:

- **B. Son**, Y. Lin, K. H. Lee, Q. Chen, and C. S. Tan, “Dark current analysis of germanium-on-insulator vertical p-i-n photodetectors with varying threading dislocation density,” *Journal of Applied Physics* **127**(20), 203105 (2020), DOI: 10.1063/5.0005112.
- **B. Son**, Y. Lin, K. H. Lee, Y. Wang, S. Wu, and C. S. Tan, “High speed and ultra-low dark current Ge vertical p-i-n photodetectors on an oxygen-annealed Ge-on-insulator platform with GeO_x surface passivation,” *Optics Express* **28**(16), 23987-23990 (2020), DOI: 10.1364/OE.398199.

The contributions of the co-authors are as follows:

- Prof Chuan Seng Tan suggested a material area and he edited manuscript drafts. In addition, he provided technical supports and solutions on the demonstration and characterization of devices.
- I led and carried out the demonstration and the characterization, and data analysis of photodetectors. Also, I did data analysis and prepared manuscript drafts.
- Dr. Yiding Lin supported device fabrication and idea development, and he commented on manuscript drafts.
- Dr. Kwang Hong Lee and Dr. Yue Wang fabricated and characterized wafers.

- Dr. Qimiao Chen and Dr. Shaoteng Wu helped with manuscript revision.

Chapter 4 is published as:

- **B. Son**, H. Zhou, Y. Lin, K. H. Lee, and C. S. Tan, "Gourd-shaped hole array germanium (Ge)-on-insulator photodiodes with remarkable responsivity and specific detectivity at 1,550 nm," *Optics Express* **29**(11), 16520-16533 (2021), DOI: 10.1364/OE.422931.

The contributions of the co-authors are as follows:

- Prof Chuan Seng Tan suggested a material area and he edited manuscript drafts. In addition, he provided technical supports and solutions on the demonstration and characterization of devices.
- I led and carried out the demonstration and the characterization and data analysis of photodetectors. Also, I did data analysis and prepared manuscript drafts.
- Dr. Yiding Lin supported me on the device fabrication and the idea development, and he commented on the manuscript drafts.
- Mr. Hao Zhou shared his fabrication recipe and provided the optimized hole array structure parameters.
- Dr. Kwang Hong Lee and Dr. Yue Wang fabricated and characterized the GOI and GeSnOI wafers at Singapore-MIT Alliance for Research and Technology.

Chapter 6 is accepted at a conference as:

- **B. Son**, Y. Lin, W. Li, K. H. Lee, J. Margetis, D. Kohen, J. Tolle, L. Zhang, T. G. Xin, H. Wong, and C. S. Tan, "Metal-semiconductor-metal photodetectors on a GeSn-on-insulator platform," *Proceeding of SPIE 10914, Optical Components and Materials XVI*, 109141A (2019), DOI: 10.1117/12.2506355.

The contributions of the co-authors are as follows:

- Prof Chuan Seng Tan suggested a material area and he edited manuscript drafts. In addition, he provided technical supports and solutions on the demonstration and characterization of devices.
- I led and carried out the demonstration and the characterization, and the data analysis of photodetectors. Also, I did data analysis and prepared manuscript drafts.
- Dr. Yiding Lin and Dr. Wei Li supported me on the device fabrication and the idea development, and he commented on the manuscript drafts.
- Dr. Yiding Lin, Dr. Wei Li, and Dr. Lin Zhang discussed the idea and commented on the idea.
- Mr. Joe Margetis, Mr. David Kohen, and Mr. John Tolle grew Ge and GeSn epitaxial layers on Si wafers.
- Ms. T. G. Xin and Prof Hong Wong provided technical solutions on the characterization of devices.

30 Jul 2021

. . . .

Date Son Bongkwon

Acknowledgment

My Ph.D. has been a fruitful journey to communicate with, listen to, and interact with my sincerely supportive, creative, and advisable friends. They do not hesitate to help me and support each other so that all of my friends can rely on each other. At the first step of jumping on this arduous Ph.D. degree, I thought this journey would be painful and require me to overcome unexpected challenges alone. However, the astonished supports and pieces of advice from many friends have made my tough Ph.D. period enjoyable and memorable. I am sure that this thesis could not have been possible without all of my brilliant friends. Thus, I'd like to thank my friends.

I could not help to mention my Ph.D. supervisor, Prof. Tan Chuan Seng. He is the best supportive supervisor who I have met in my life. Always he has been supporting me from the standpoint of students in technical, financial, and emotional issues that I have faced during the Ph.D. journey. I have felt that he had put first priority on student's emotions so that the student can readily clear hurdles. Besides, needless to say, his advice on research inspired me and was nutritious all the time. The technical issues that I have struggled with in my Ph.D. have been handled largely by him. The financial supports do not matter for me as long as I have enough passion and convictions for my research, and he has always stood beside me. Beyond the supports related to research, he counsels me individually in the human relationship and the meaningful Ph.D. life. I do not hesitate to say that he is my supervisor, a saivor, and a respected friend for research.

I am also grateful to Group Four Photonics (GFP) group members. Dr. Lin Yiding helped me a lot with settling down and research ideas. The time I spent with him was meaningful because he always encouraged me. Although he graduated from his Ph.D. and left the group, he continually supported me in research. Dr. Li Wei, who moved to Huawei after his graduation, is outgoing and supportive. He gently taught me how to handle equipments. Zhou Hao is approachable to share a small talk. He sometimes worries about what he is doing, and he is anxious about his future. But, I firmly believe he is better than what he thinks of himself. This gratitude also includes postdocs in our group. Dr. Zhang Lin helped me with providing high-quality Ge and GeSn samples to realize my ideas. Dr. Qimiao Chen also advised me on research ideas. Dr. Shoateng Wu gave me a piece of advice on my works. Also, Dr. Chun Kiat Simon Goh helped me with the technical issues and had fun chats in an office.

Besides, I should mention Assistant Prof. Donguk Nam, who suggested a good opportunity and counseled me for the Ph.D. journey in NTU. He motivated me to be a better researcher and he encouraged me to be energetic and excited about exploring undiscovered things. Daniel also came up with fancy ideas and shared them with me. I wish Yongduck and Youngmin all the best for the rest of their Ph.D. journey. Members of Centre for Micro- & Nano-Electronics (CMNE) should be mentioned for technical support and equipment sharing. Ms. Tina Guo Xin is always supportive and was willing to teach me how to handle equipment friendly and share the equipment for my device testing. Dr. Brian and Dr. Xiang Li had told me about their Ph.D. life so that I could feel their passion and goals to achieve indirectly.

Dr. Xincai Wang, who is my co-supervisor at Singapore Institute of Manufacturing Technology (SIMTech) from Agency for Science, Technology and Research (A*STAR), allows me to use the excimer laser to investigate the laser annealing on GeSn and Ge. I would like to thanks the cleanroom staff at Nanyang Nano Fabrication Centre (N2FC) from EEE in NTU. They keep providing the use of equipment in the best condition for researchers to be able to conduct their works properly.

Lastly, I am very thankful to my parents and my brother for their unwavering strong belief and unconditional support. My Ph.D. would not have been successfully finished without their patience. The strong supports from my family make me be able to concentrate on the research. I sincerely thanks them for being healthy and staying beside me always. I humbly dedicate this work to my family.

I appreciate National Research Foundation Singapore Competitive Research Programme under Grant NRF-CRP19-2017-01, which has supported this thesis financially. Also, SIMTech should be mentioned for acknowledgment because they allow me to use the excimer laser as a Ph.D. student attached to SIMTech.

Table of Contents

Summary

Demand for Near- (NIR) and Mid-infrared (MIR) range detection has increased drastically for practical applications in optical sensing, imaging, and communications. Silicon (Si)-based photonic integrated circuits (PICs) have drawn attraction for such applications with cost-effectiveness, low power consumption, ultra-compact device footprint, and complementary metal-oxide-semiconductor (COMS) compatibility. However, Si is an indirect bandgap material with a bandgap of 1.12 eV, which makes it challenging to cover the wavelength beyond 1,100 nm. Although numerous efforts have been put into extending its cut-off wavelength, the large Si bandgap even restricts the whole NIR range photodetection.

Germanium (Ge), a Group IV element, is CMOS compatible with an indirect bandgap of 0.66 eV. Since the direct conduction band of Ge bulk is located only 140 meV higher than the indirect band, a Ge photodetector is able to do NIR photodetection. Germanium-tin (GeSn) photodetectors have been introduced for MIR range photodetection, taking advantage of its bandgap tunability and excellent optical and electrical properties. An increase in Sn content shrinks GeSn bandgap and improves carrier mobility. In addition, GeSn lasers have been reported with direct bandgap properties, accelerating the development of the monolithic integration of Group IV-based optoelectronic integrated citcuits in the MIR range. As such, Ge and GeSn optical components are primarily attractive to NIR and MIR range applications, respectively.

Nevertheless, III-V compound semiconductor photodetectors, e.g., indium gallium arsenide (InGaAs) photodetectors, dominate the industry despite their CMOS incompatibility, high complexity, and high cost. In order to utilize Ge/GeSn material systems for low-cost and CMOS compatible photodetectors, a low dark current and a high photon collection efficiency are required. During the epitaxial Ge/GeSn growth on a Si substrate, high density defects/dislocations are generated due to the large differences in the thermal expansion coefficient and lattice constants. The dislocations/defects act as trap states that degrade optical and electrical properties in Ge/GeSn material systems. Therefore, mitigation of defects in Ge/GeSn material systems should be implemented to improve optical performances. Direct wafer bonding (DWB) and layer transfer techniques enable a transfer of Ge/GeSn epitaxial layers directly on insulator platforms. The insulator platform improves not only optical confinement but also provides electrical isolation. In addition, defective Si/Ge/GeSn interfaces can be readily eliminated with the techniques, leading to enhanced photodetection in terms of dark currents and optical responsivities.

This thesis explores high-performance Ge/GeSn photodetectors, which are fabricated on insulator platforms. In addition, furnace annealing in oxygen (O_2) ambient and germanium-oxide (GeO_x) formation via ozone (O_3) oxidation are conducted to achieve a sub-mA/cm^2 dark current for a Ge photodetector. Also, optical responsivity for the Ge photodetector is improved by gourd-shaped hole array structures. With these advanced techniques, improved detectivity is obtained, comparable to commercial Ge bulk and extended III-

V photodiodes. GeSn alloys are investigated for MIR range photodetection. It is revealed that trap states near a Ge/GeSn interface degrade electrical and optical properties in GeSn material systems. In order to mitigate the trap-related carrier dynamics, waveguide GeSn photodetectors are demonstrated on an insulator platform. DWB and layer techniques enable the realization of a GeSn-on-insulator (GeSnOI) platform without the GeSn/Ge interface layer. A demonstrated GeSn photodetector on the GeSnOI platform provides the photodetection beyond 2,000 nm. The proposed Ge/GeSn photodetectors would be widely applicable to Si-based PICs for high-efficiency NIR and MIR range photodetection.

List of Figures

List of Tables

List of Abbreviations

Si	silicon
CMOS	complementary metal-oxide-semiconductor
MPW	multi-project wafer
SOI	silicon-on-insulator
TE	transverse-electric
TM	transverse-magnetic
NIR	near-infrared
MIR	mid-infrared
LiDAR	light detection and ranging
3D	three-dimensional
PIC	photonic-integrated circuit
SEM	scanning electron microscope
ToF	time of flight
FoV	field of view
FPA	focal plane array
LO	local oscillator
N_2O	nitrous oxide
CH_4	methane
CO_2	carbon dioxide
NH_3	ammonia
EHP	electron-hole pair
Ge	germanium
GeSn	germanium-tin
GOI	Ge-on-insulator
GeSnOI	germanium-tin-on-insulator
EQE	external quantum efficiency

TD	threading dislocation
O_2	oxygen
TDD	threading dislocation density
O_3	ozone
InGaAs	indium gallium arsenide
GeO_x	germanium-oxide
CMP	chemical mechanical polishing
CVD	chemical vapor deposition
H_2	hydrogen
As	arsenic
SRB	strain-relaxed buffer
SnD_4	Tin deuteride
UHV-CVD	ultra-high vacuum chemical vapor deposition
$SnCl_4$	Tin chloride
Ge_2H_6	digermane
MBE	molecular beam epitaxy
FDTD	finite-difference time-domain
LED	light-emitter diode
SOI	Si-on-insulator
EL	electroluminescence
GOS	Ge-on-Si
GON	Ge-on-silicon nitride
SEM	scanning electron microscope
TEM	transmission electron microscopy
PL	photoluminescence
MOS	metal-oxide-semiconductor
FEOL	front-end-of-line
NB	nanomembrane
BOX	buried oxide

DWB	direct wafer bonding
BEOL	back-end-of-line
Gd_2O_3	gadolinium oxide
2D	two-dimensional
MSM	metal-semiconductor-metal
MQW	multi-quantum well
RCEPD	resonant cavity-enhanced photodetector
NEP	noise equivalent power
SRH	Shockley-read-hall
TAT	trap-assisted tunneling
PECVD	plasma-enhanced chemical vapor deposition
DI	deionize
OH	hydroxyl
TMAH	tetramethyl-ammonium hydroxide
RMS	root mean square
HRXRD	high-resolution X-ray diffractometry
EPD	etch pit density
SIMS	secondary ion mass spectroscopy
SRP	sheet resistance profile
Cl_2	chlorine
RIE	reactive ion etching
BOE	buffered oxide etch
CHF3	trifluoromethane
Ti	titanium
TiN	titanium nitride
Al	aluminum
FIB	focused ion beam
ALD	atomic layer deposition
XPS	X-ray photoelectron spectroscopy

BTBT	band-to-band tunneling
MOS	metal-oxide-semiconductor
P	phosphorus
EBL	electron-beam lithography
SF_6	sulphur hexafluoride
ICP-RIE	inductively coupled plasma ion etching
HRTEM	high-resolution transmission electron microscopy
PC	photoconductivity
RPCVD	reduced pressure chemical vapor deposition
SBH	Schottky barrier height
VRH	variable-range-hopping
EHP	electron-hole pair
MSM	metal-semiconductor-metal
SAM-APDs	separated absorption and multiplication region avalanche photodiodes

List of Symbols

Δt	round-trip time delay
d	distance
c	speed of light
η_{LiDAR}	LiDAR efficiency
T_{f}	transmission of incidence photon
T_{b}	scattered photon
N_{b}	background noise
β	interaction efficiency
λ	wavelength
h	Planck’s constant
ΔE	relevant energy for transition
l	length
w	width
t	thickness
σ_{dark}	conductivity without illumination
q	electron charge
n	free carrier concenctration of electron
p	free carrier concenctration of hole
μ_{e}	electron mogility
μ_{p}	hole mogility
I_{dark}	dark current
E_{x}	electric field
A	cross-sectional area
σ_{photo}	conductivity under illumination
$\Delta\sigma$	change in conductivity after illumination
Δn	excess electron carrier concentration

Δp	excess hole carrier concentration
G_0	net optical negation rate
τ_p	hole lifetime
τ_n	electron lifetime
I_{photo}	photocurrent
ΔI	change in current after illumination
τ_{eff}	effective carrier lifetime
t_e	electron transit time
t_h	hole transit time
η	quantum efficiency
P_{inc}	optical power
ν	frequenct of photon
R	responsivity
W_d	depletion width
ε_0	vacuum permittivity
ε_r	dielectrin constant in semiconductor
V_{bi}	bulit-in voltage
N_A	doping concentration for donor
N_D	doping concentration for acceptor
J_{dark}	dark current density
D_n	minor carrier diffusion constant for electron
n_i	intrinsic carrier concentration
L_n	diffusion length in *n*-type region
D_p	minor carrier diffusion constant for hole
L_p	diffusion length in *p*-type region
k	Boltzmann constant
T	temperature
J_0	saturation current density
J_{photo}	photo current density

α	absorption coefficient
D	diameter
θ	theta
ω	omega
V	voltage
I_{surf}	surface leakage current
I_{bulk}	bulk leakage current
E_{a}	activation energy
B	constant
J_{SRH}	Schottky-read-hall current density
J_{TAT}	trap-assisted-tunealing current density
Γ_{enhan}	trap-assisted-tunealing enhancement factor
e	electron charge
τ	Schottky-read-hall carrier lifetime
I_{diff}	diffusion current
C	capacitance
R	responsivity
P_{in}	output optical power
i-Ge	intrinsic-germanium
t_{Ge}	intrinsic-germanium thickness
h	Planck's constant
r	reflectivity
R_e	resistance
f_{3dB}	3dB bandwidth
f_{T}	carrier transit-limited bandwidth
f_{RC}	resistance-capacitance delay-limited bandwidth
v_{sat}	saturation drift velocity
$R_{e,load}$	load resistance
$R_{e,series}$	series resistance

C_j	junction capacitance
C_p	parasitic capacitance
D^*	specific detectivity
A_{absor}	absorption
R_{reflec}	reflectance
T_{trans}	transmittance
FF	fill factor
Δf	noise bandwidth
I_{rms}	root-mean-square noise current
I_{shot}	shot noise
$I_{thermal}$	thermal noise
R_{shunt}	shunt resistance
$C_{j,hole}$	hole area junction capacitance
$C_{j,no\text{-}hole}$	hole-free area junction capacitance
Γ	direct
L	indirect
$J^{\Gamma}{}_{\mathrm{diff}}$	diffusion current in the Γ-conduction band
$J^{\mathrm{L}}{}_{\mathrm{diff}}$	diffusion current in L-conduction band
$J^{\mathrm{h}}{}_{\mathrm{diff}}$	diffusion current in valence bands
$a^{\parallel}$	in-plane lattice constant
$a^{\perp}$	out-plane lattice constant
$a^{0}{}_{\mathrm{GeSn}}$	geranium-tin lattice constant
x	tin content
$a^{0}{}_{\mathrm{Sn}}$	tin lattice constant
$a^{0}{}_{\mathrm{Ge}}$	germanium lattice constant
b_{GeSn}	bow parameter
v_{GeSn}	germanium-tin poison ratio
v_{Ge}	germanium poison ratio

v_{Sn}	tin poison ratio
I_0	saturation current
n_{ideal}	ideal factor.
A^*	Richardson constant
ϕ_b	Schottky barrier height
$\Delta\omega$	Raman spectral shift
ε_{strain}	strain
V_{bi}	built-in potential
ε	germanium-tin permittivity
σ_0	a fitting parameter of the conductance
T_1	characteristic temperature

Chapter 1. Introduction

1.1 Background: Si Photonics

Electro-optical effects in silicon (Si) were first reported in 1987 [1]. Since then, Si photonics has been investigated in many universities, research institutes, and foundries. The capability of complementary metal-oxide-semiconductor (CMOS)-compatible process, which is provided by current Si markets, accelerates its development despite the early commercial stage. Advanced Si photonics is employed in data communications and telecommunications to replace conventional metal-based communication. In addition, Si photonics has been introduced in the fields of quantum computing as well as artificial intelligence.

Si photonics companies and start-ups are able to launch their products with the help of various Si photonic foundries. Such an ecosystem enables massive investments so that diverse Si photonics products become available. Figure 1 displays available foundries that support customers to achieve their goals in Si photonics. The services include prototype lines, CMOS pilot lines, fabrications, and packaging. Brokers provide customers with the information of appropriate processes and companies to get their own values.

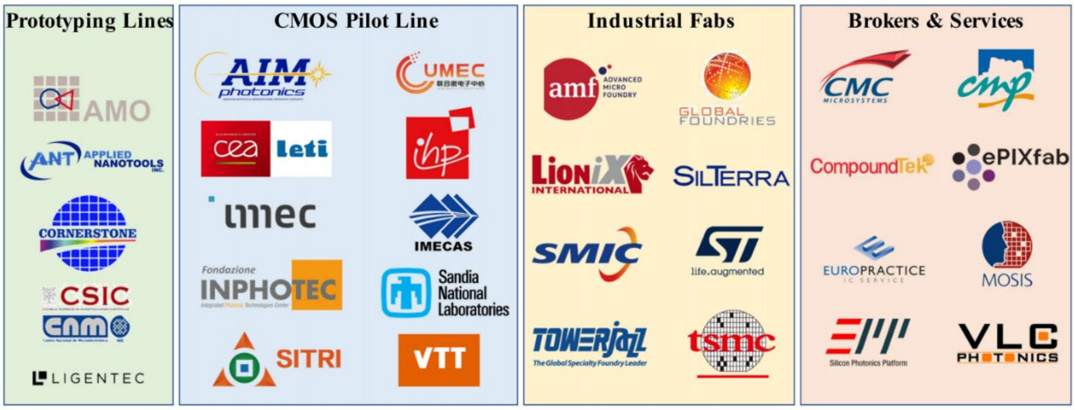

Figure 1. Si photonics foundries that provide open access fabrication services [2].

Multi-project wafer (MPW) service, volume production, and customized service are provided by most foundries. The MPW process allows customers to design products based on provided modules. This process is a mature process in foundries to share their design to conduct multiple projects per wafer [3]. The photograph of a demonstrated MPW is illustrated in Figure 2(a). Inset in Figure 2(a) shows the single cell of a fabricated chip.

The mainstream of Si photonics is developed on insulator substrates. Thanks to high refractive index contrast and high CMOS compatibility, silicon-on-insulator (SOI) wafers have been utilized to demonstrate active and passive optical devices, e.g., waveguides, modulators, receivers, gratings, etc. [2]. The cross-sectional schematic view of Si photonics components is illustrated in Figure 2(b).

(a)

(b)

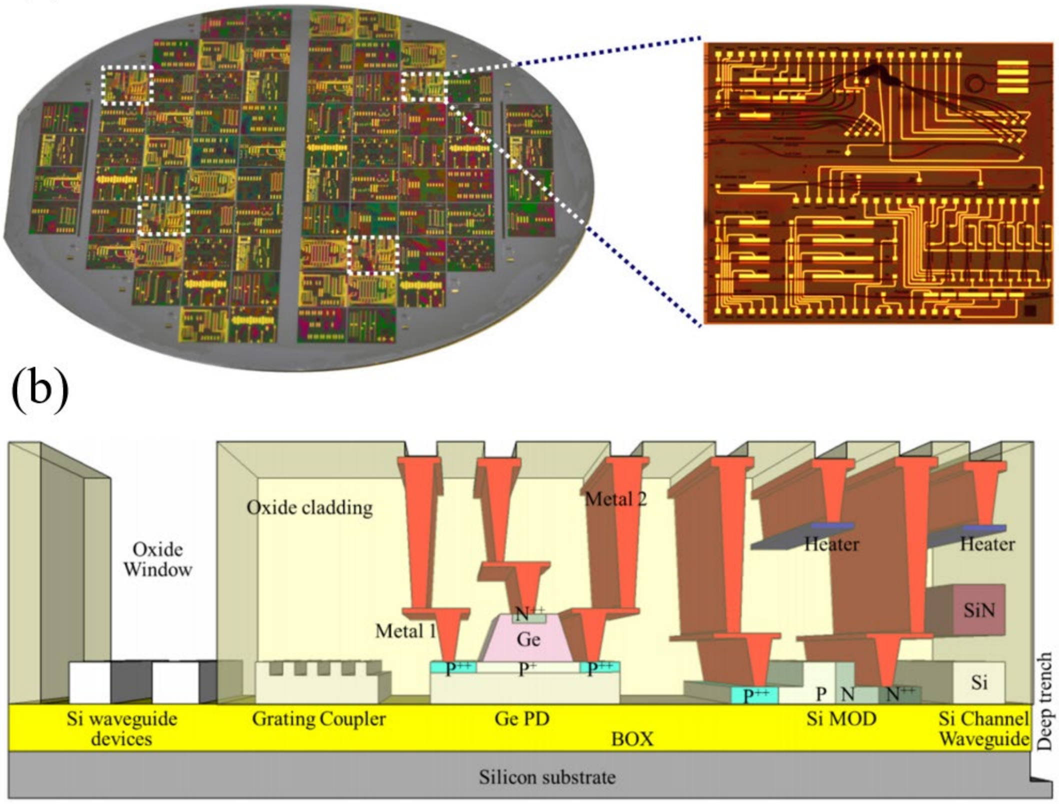

Figure 2. (a) The photograph of a demonstrated MPW in wafer-scale. Inset in Figure 2(a) displays the top view of a fabricated single-chip [3]. (b) The cross-sectional schematic view of Si photonics components [2].

Si waveguides are typically on a few μm of silica cladding layers with 220 nm silicon core layers in a 200 mm wafer-scale. Such structures allow low propagation loss and low bending radius. A thin Si core layer is required for optical single-mode conditions. The Si waveguide displayed the propagation losses of ~0.59 and ~2.4 dB/cm for transverse-electric (TE) and transverse-magnetic (TM) modes at 1,550 nm, respectively [4]. Waveguides can be directly connected with optical fibers so that the light signal travels through them without a grating.

A grating consists of the different materials or structures. Among them, SOI platforms enhance diffraction effects, leading to high coupling efficiency.

The peak coupling efficiency for a grating was achieved to be -1.3 dB at 1,550 nm experimentally [5].

An optical modulator is a device that manipulates the phase, amplitude, or polarization of light. Heating up or applying an electric field alters *n* and *k* indices, changing its optical properties. Recent modulators achieved a high data rate of 20 Gbit/s at 2,000 nm [6]. Typically, the modulator is linked with waveguides so that light is modulated in traveling waveguides.

A photoreceiver is a device that converts light signals into electrical ones. Diverse photoreceivers are present, such as a photodiode, a phototransistor, a superconducting nanowire photodetector, etc. A photodiode typically contains an absorption region. The photoexcited carriers are generated by transiting light energy into electrical energy. By sweeping out the carriers, photocurrent increases. Si photodetectors have been investigated for visible or short-wave infrared range photodetection. Recent discoveries develop cut-off wavelength extension beyond Si bandgap, suitable for diverse applications [7].

1.2 Applications for Si Photonics

Si photonics has diverse applications operating in the NIR (near-infrared, wavelengths from 0.7 to 2.0 μm) and MIR (mid-infrared, wavelengths from 2.0 to 20.0 μm) ranges. In this section, various applications for Si photonics are discussed. In Chapter 1.2.1, fiber-optics communications will be described. Chapter 1.2.2 addresses Light Detection and Ranging (LiDAR) for three-dimensional (3D) imaging. A gas sensor will be elucidated in

Chapter 1.2.3. This section aims to propose the promising applications, which Si photonics have seeped into for the past years.

1.2.1 Communication: Optical Fiber Communication

Optical fiber communications have led to technological advances for high bandwidth infrastructure due to increased demand for numerous data transfer and processing. Particularly, digital optical network, network domain between optical-electronic-optical signals is minimized via Si-based photonic-integrated circuits (PICs), can be achieved with low-cost, high compact, and high sustainability [8]. Figure 3 displays the schematic image of Si photonic transceivers with a fiber optics cable. Electrical signals are converted into optical signals in the light source. The generated lights pass through waveguides, modulators, fiber optical cables. The optical signals arrive at the opposite transceiver so that the photoreceivers can read the optical information. For efficient signal transmission, spectral windows should be properly defined for efficient data communication.

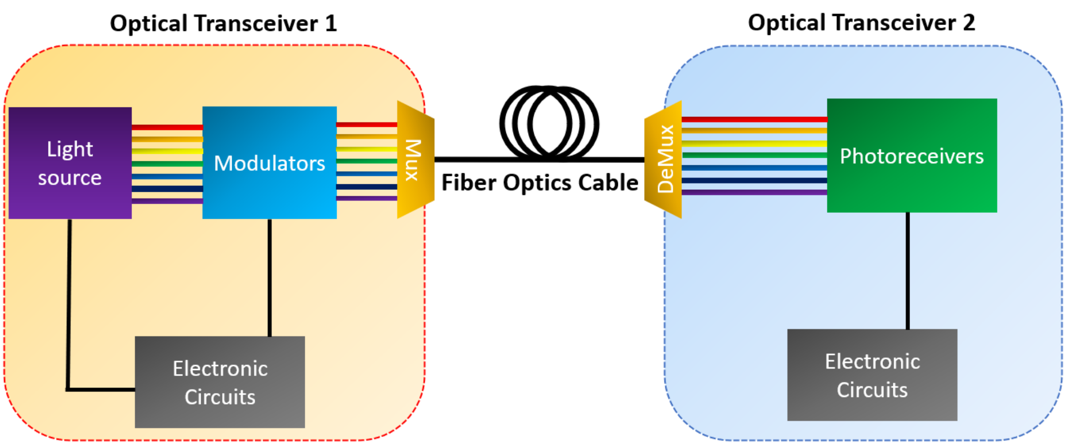

Figure 3. The schematic image of Si photonic transceiver. Rainbow lines represent optical paths. Mux and DeMux mean a multiplexer and a demultiplexer, respectively.

Low attenuation coefficient range near 0.8 (1st window), 1.3 (2nd window), and 1.55 μm (3rd window) are defined as "transmission windows" for standard optical fiber communications (single-mode and multi-mode fibers). Rayleigh scattering and the OH^- absorption in the optical fibers contribute to the 1st, 2nd, 3rd spectral windows. The absorption loss caused by the Rayleigh scattering can be described by the equation of $\alpha_R = A/\lambda^4$ where α_R, A, and λ are the intrinsic loss coefficient of the optical fiber, the constant (0.7-0.9 $dB \cdot km^{-1} \cdot \mu m^{-4}$), and the wavelength, respectively. The loss for the optical fiber caused by the Rayleigh scattering decreases with the wavelength. In addition, the OH^- absorption is predominant at 1,000, 1,400, and 1,600 nm. Since the desirable length of fibers can be more than 50 or even 100 km, low attenuation becomes the key factor in determining the optical fiber's feasibility [9]. Figure 4 shows fiber attenuation spectra as a function of wavelength. All the transmission windows offer a loss of <10 dB/Km. The lowest attenuation of <1 dB/km is observed near 1,550 nm, an attractive wavelength for diverse applications.

Recently, a hollow-core fiber was proposed for low loss and nonlinearity. A hollow-core fiber consists of distributed micro-structures or patterns within a core layer. This configuration determines specific propagation modes, which can travel through cladding or air holes. Suppressed Rayleigh scattering in hollow-core fibers draws attention to ultra-low attenuation losses. Two key factors, i) surface scattering at glass/air interface and ii) infrared absorption in glass matrix defines the lowest attenuation spectral window. Figure 4(b) shows the cross-sectional scanning electron microscope (SEM) images of hollow-core fibers. The loss for the fabricated fibers and for the expected loss for the ideal fibers are displayed in Figure 4(c). The estimated spectral window shifts from 1,550 to 1,900-2,100 nm. The lowest attenuation was obtained to be < 0.1 dB/km. It should be noted that wavelength spectral windows near 1,550 and 2,000 nm are high-demand spectral windows for optical fiber communications.

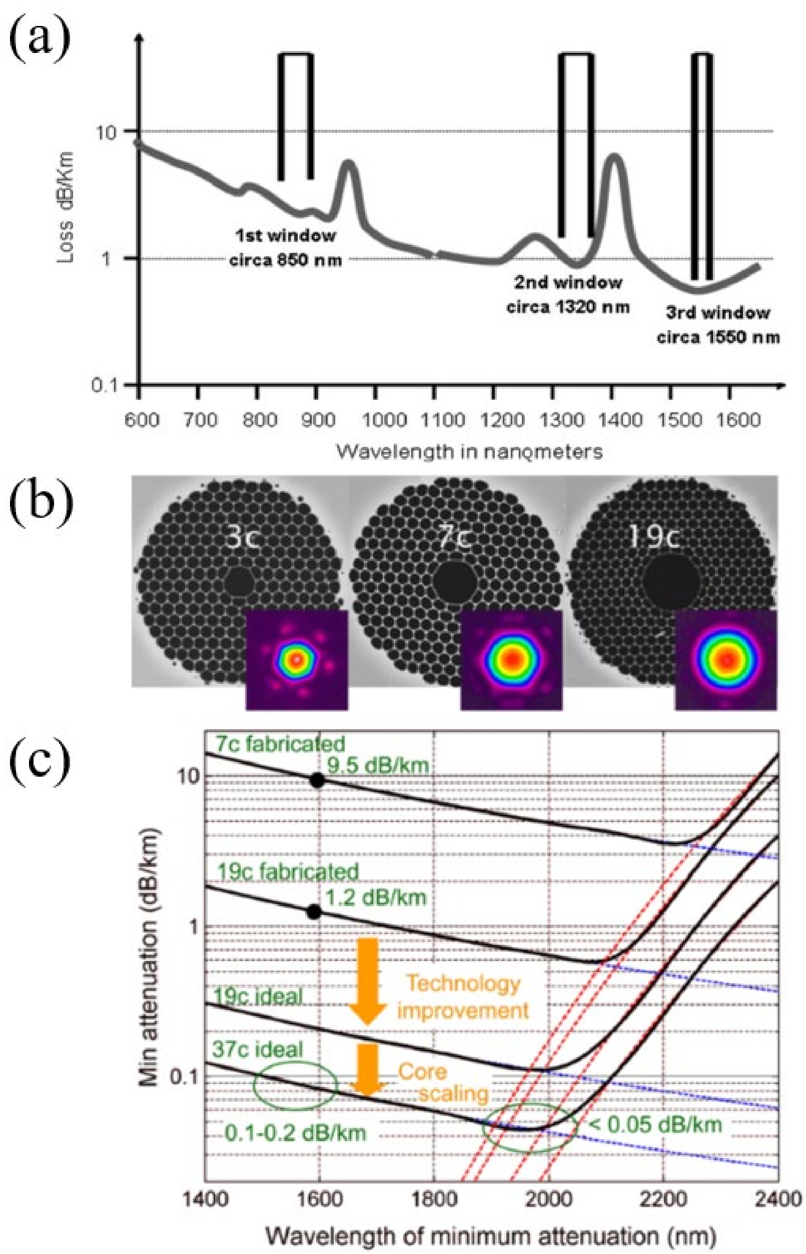

Figure 4. (a) Total fiber attenuation as a function wavelength [10]. (b) SEM images of photonic bandgap fibers with varying core sizes and corresponding fundamental mode images [11]. (c) The fundamental mode loss as a function of wavelength for the varying core sizes [11].

1.2.2 Remote and Imaging Sensing: LiDAR

Remote sensing is the acquisition of information about an object by detecting signals that reflect from an object. Remote sensing has been widely applied in archaeology, agriculture, cartography, and geographic information because a remote sensor provides a wide range of depth and imaging information. Thus, the demand for a remote sensor has increased for technological advances.

LiDAR technique is one of the remote sensing methods that has been recently emerged along with its brothers, e. g., radio detection and ranging, camera vision remote sensing, and ultrasonic sensing techniques. LiDAR has been for a rich history of over 60 years, starting its development in the early 1960s once a laser was invented [12]. By receiving the pulsed photon, the particle of light LiDAR measures the distance between a sensor and a target object based on how long it takes for the photon to return back to the sensor, named the Time of Flight (ToF) technique. By repeating this process, a 3D image can be reconstructed, as shown in Figure 5.

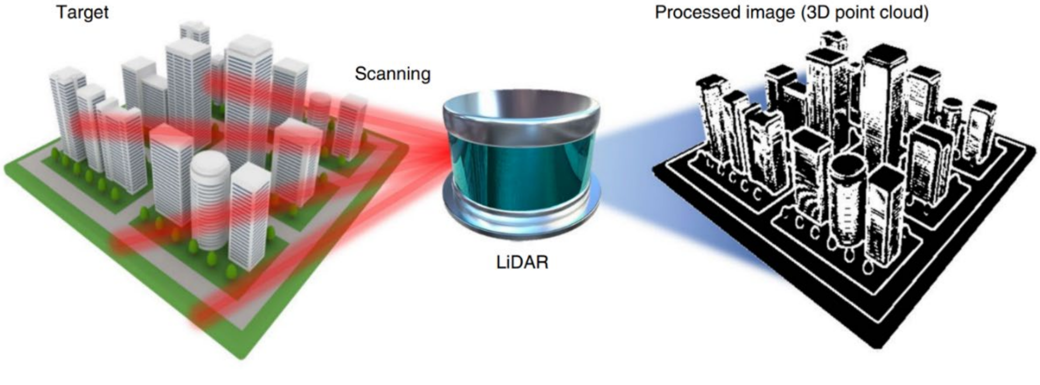

Figure 5. The schematic image of LiDAR for scanning and 3D depth recognition [13].

Conventionally, a direct ToF technique has been adopted as the most common ranging system. The ToF technique measures round-trip time delay (Δt), how long an emitted photon takes until it returns back after bouncing off an object. By doing so, the distance (d) can be obtained by $d = c\Delta t/2$, where c is the speed of light.

LiDAR performance is determined by some parameters. Pulse width mainly determines spatial depth resolution. With the assumption that pulse period is consistent, narrow pulse width provides high resolution. The pulse period is the main contributor to determine a detection range. A single pulse signal must not be mixed up with the next signal to avoid mixing data. Scattering rate during the range sensing is one of the crucial factors to determine the remote sensing performance. LiDAR scattering form equation is expressed by the following equation [13],

$$N_{LiDAR} = N_{laser} \times \left[\beta \times \frac{A}{R^2} \times T_f(R) \times T_b(R) \times \eta_{LiDAR}\right] + N_b \quad (1)$$

where η_{LiDAR} is LiDAR efficiency and T_f and T_b represent the transmission of incidence photon and scattered photon, respectively, and N_b is background noise, and β is the interaction efficiency with the object. Extra physical processes should be considered additionally, such as Doppler shift, resonant scattering, and so on. The overall working sequence of LiDAR is shown in Figure 6.

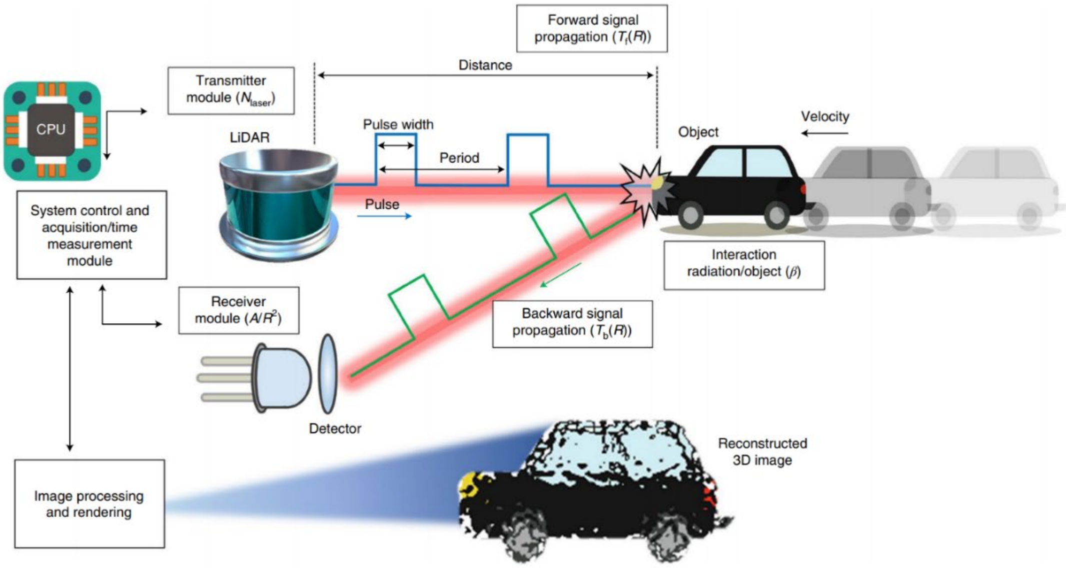

Figure 6. Schematic description for direct ToF measurement method [13].

Focal plane array (FPA) has been widely adopted for a LiDAR receiver part. The main concept is to use a lens to collect a scattered light into a receiver array. A proper lens can be changed to tune the field of view (FoV).

The schematic views of FPA and a single-pixel receiver on SOI platforms are shown in Figure 7 and inset in Figure 7, respectively. Local oscillator (LO) light travels in waveguides heading to each pixel. Scattered light bounced off an object also reaches a grating coupler in each pixel. The received signals are electrically amplified by a transimpedance amplifier. Then a row amplifier transmits the electrical signals to a signal processor, reconstructing a 3D image with distance and velocity information.

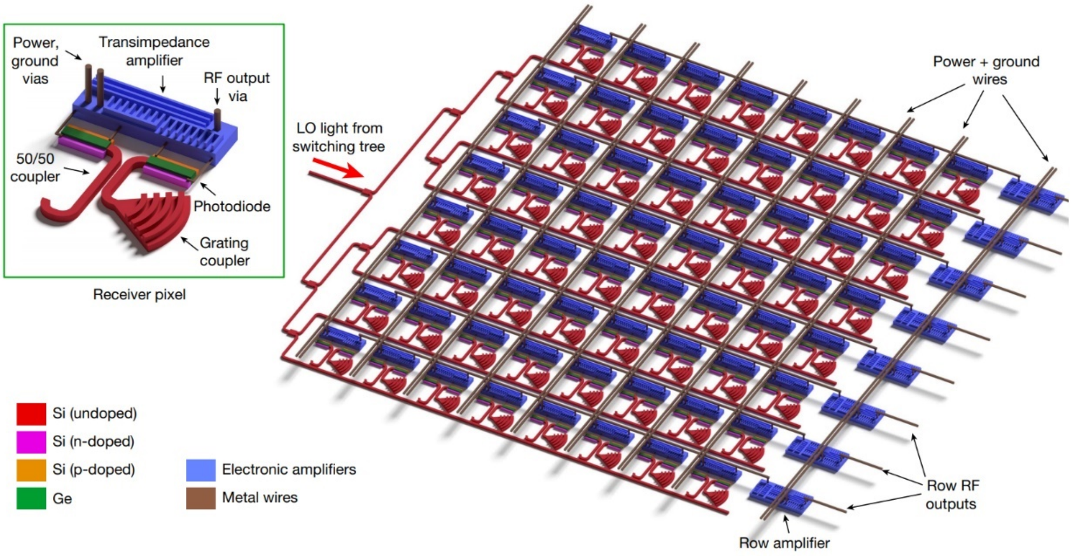

Figure 7. The schematic image of a receiver array. Inset represents each receiver pixel. RF is a radio frequency [14].

Figure 8(a) displays the reconstructed 3D image with the depth and the velocity information of a basketball at 17 m distance rotating its vertical axis at 1 rpm, and Figure 8(b) shows the photograph of a rotating basketball setup. Figure 8(c) represents measured velocity information using LiDAR. Each FPA pixel can collect the depth and velocity information at a single point and assemble all the information collected via pixels so that the high-resolution 3D image along with the velocity of the object can be obtained. It should be noted that the velocity information is extracted via the Doppler effect.

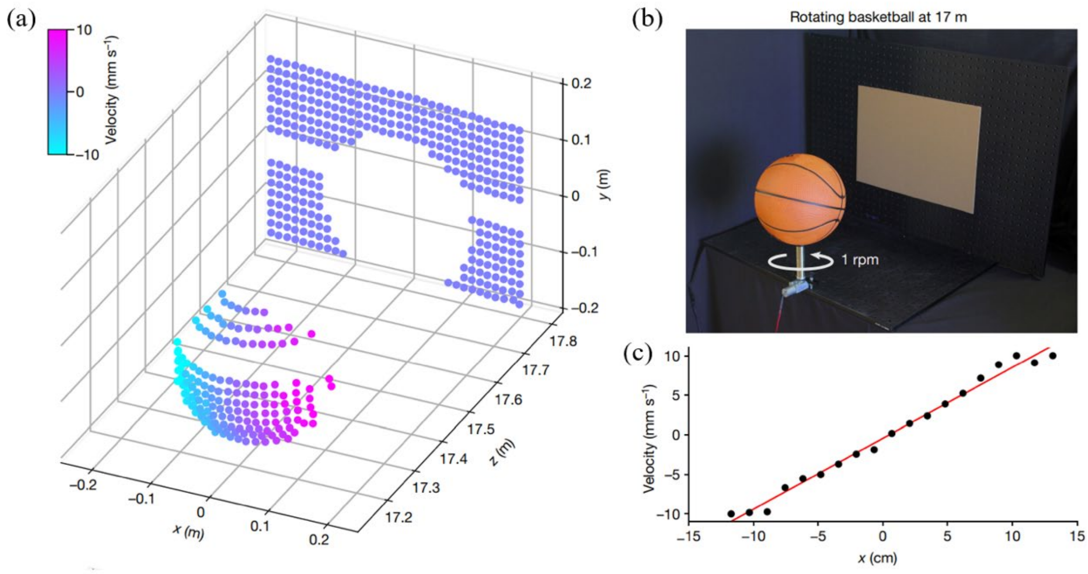

Figure 8. (a) The point cloud of depth- and velocity-information of a basketball at 17 m depth rotating by 1rpm. (b) The photograph of a rotating basketball setup. (c) Measured velocity variation as a function of the x-axis position [14].

1.2.3 Molecular Sensing: A Gas Sensor

On-chip gas sensing is required for a multitude of applications, e.g., climate sensing, agricultural industry, chemical industry, and medical industry. Sensitivity is the key factor to determine the performance of low concentration detection. Thus, diverse methods have been proposed to obtain high-efficiency molecular sensing. Among them, PICs have attracted attention due to their low-cost and footprint [15].

NIR and MIR ranges have been selected as spectral windows for molecular sensing, widely utilized in optical communications and 3D imaging fields. Detectable molecules in the wavelength ranges are nitrous oxide (N_2O), methane (CH_4), carbon dioxide (CO_2), ammonia (NH_3), etc. Figure 9(a) displays the 3D schematic image of an on-chip molecular sensor for CH_4 sensing. SOI wafers are selected for the demonstration of a molecular sensor.

Figure 9(b) and (c) represent a cross-sectional view and electric field distribution in a waveguide. The Si waveguide can confine the light due to its high index contrast with insulators, and an evanescent field in waveguides reacts with molecules on waveguides. Lights traveling waveguides are modulated due to the absorption properties of each molecule, as shown in Figure 9(d). Although Si-based or InP-based PICs for gas sensing still have not approached the sensitivity of bulk optics, Si-based PICs are promising in terms of manufacturing price, sustainability, and footprint.

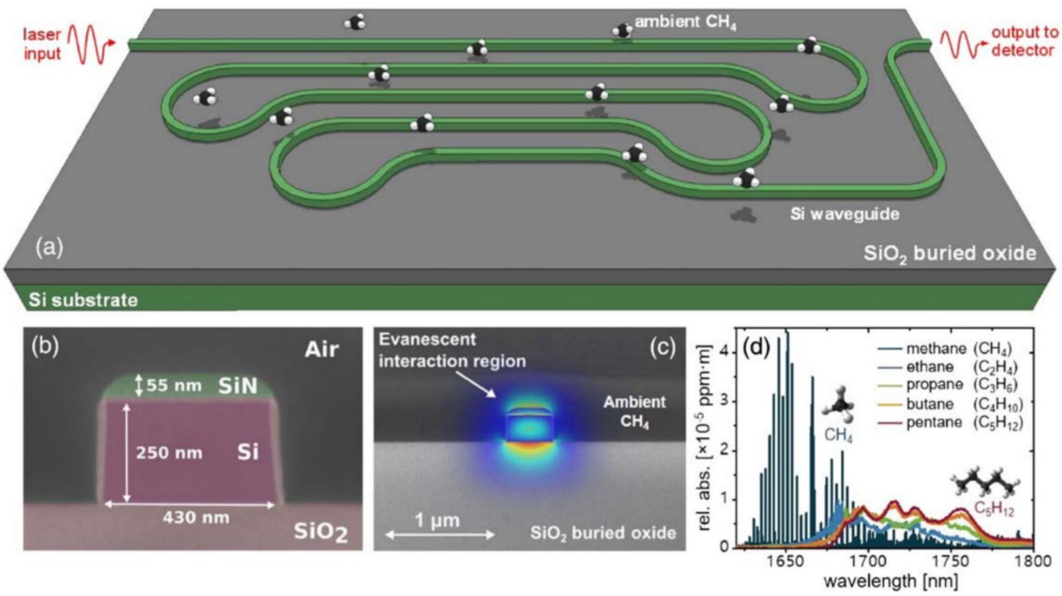

Figure 9. (a) The 3D schematic image of a waveguide on-chip for molecular detection via evanescent sensing. (b) The cross-sectional view of a Si waveguide. (c) Electric-field distribution for a waveguide. (d) Absorption spectra for various CH_4 constituents. (e) The 3D schematic image of an on-chip gas sensor [15].

1.3 Background of Photodetectors

Diverse Si photonic applications, in general, involve light-emitting and light-receiving processes. The light-emitting process is to convert an electrical signal into an optical signal. On the contrary, the light-receiving process is to convert an optical signal into an electrical signal. This thesis focuses on the light-receiving part mainly. In the light-receiving process, the incident light excites the carriers in an absorption region, which satisfies Eq. 2. Subsequently, photo-excited carriers are swept to the electrodes. The extraction of the excited carriers can be read out as photocurrent in the external circuit. Photodetectors are the key building blocks to enable this light-receiving process. They are of many types but they can be divided into two main schemes: i) thermal detectors detecting the optical signal to rise temperature when the light is absorbed, and ii) photon detectors to generate electron-hole pairs (EHPs) when the incident radiation is absorbed. Typically, the excited carrier concentration is proportional to the intensity of the incident radiation. In this thesis, photon-based detectors will be mainly investigated. In order to detect a photon, the active region in photodetectors should be satisfied with the following equation,

$$\lambda = \frac{hc}{\Delta E} \tag{2}$$

where λ, h, c, and ΔE are the wavelength of the photon, Planck constant (6.62×10^{-34} m^2kg/s), the speed of the light (3×10^8 m/s), and the relevant energy for transition, i. e., interband absorption, interband impurity absorption, and barrier height absorption.

1.3.1 Photoconductors

Photoconductors are photodetectors that exhibit a reduction in electrical resistance caused by incoming light. Typically, they consist of a slab of a semiconductor with electrodes at either end, which forms an ohmic contact with the semiconductor, as shown in Figure 10. Once the light is absorbed in a semiconductor, excess EHPs are generated and collected by the electrodes under applied voltage, which produce the photocurrent.

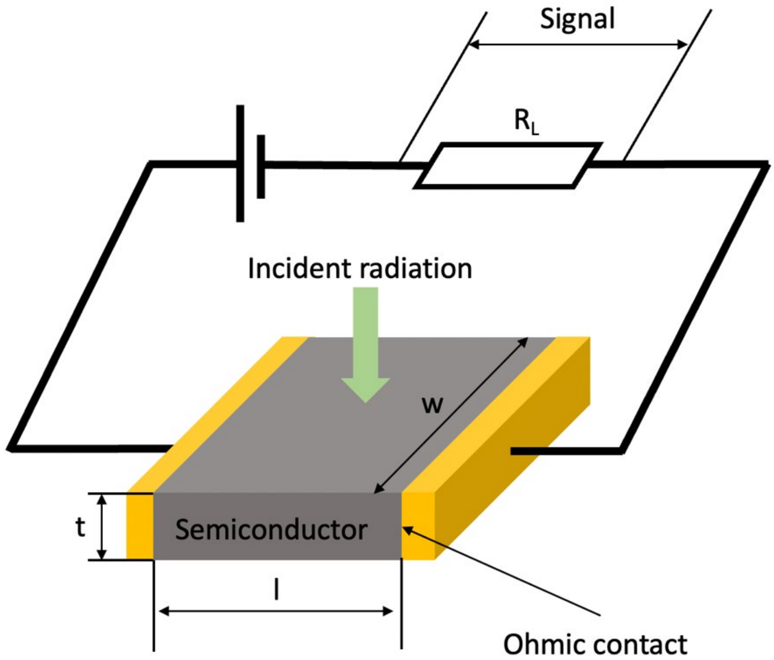

Figure 10. The schematic structure of the photoconductor.

The conductivity (σ_{dark}) for photoconductors without illumination can be expressed by,

$$\sigma_{dark} = q(n\mu_e + p\mu_h) \tag{3}$$

where q is the electronic charge (1.6×10^{-19} C). μ_e, and μ_p are the electron and hole mobilities, respectively. n and p are the free carrier concentration of electrons and holes (cm^{-3}). The dark current (I_{dark}) can be expressed by,

$$I_{\text{dark}} = \sigma_{dark} E_x A = q(n\mu_e + p\mu_h) E_x A \tag{4}$$

where A is the cross-sectional area (A=tw) and E_x is the electric field.

Under illumination, the conductivity (σ_{photo}) for photoconductors can be changed as follows,

$$\sigma_{photo} = \sigma_{dark} + \Delta\sigma = q(n\mu_e + p\mu_h) + q(\Delta n\mu_e + \Delta p\mu_h) \quad (5)$$

where $\Delta\sigma$ is the change in the conductivity under illumination. Δn and Δp are the excess electron and hole carrier concentrations under illumination, respectively, which can be described by $\Delta n = G_0\tau_n$ and $\Delta p = G_0\tau_p$, where G_0, τ_n, and τ_p are the net optical generation rate and electron and hole lifetimes, respectively. The photocurrent (I_{photo}) can be expressed by the following expression,

$$I_{\text{photo}} = I_{\text{dark}} + \Delta I = I_{\text{dark}} + qG_0(\mu_e + \mu_h)E_xA \quad (6)$$

or

$$I_{\text{photo}} = I_{\text{dark}} + qG_0\tau_{eff}\left(\frac{1}{t_e} + \frac{1}{t_h}\right)EA \quad (7)$$

where ΔI, τ_{eff}, t_e, and t_h are the change in current after illuminatioin, the carrier effective lifetime, the transit times for electrons and holes, respectively.

The net optical generation rate can be expressed by the following expression,

$$G_0 = \eta\frac{P_{inc}/hv}{lwt} \quad (8)$$

where η, P_{inc}, and ν are the quantum efficiency, the optical power, and the frequency of the photon, respectively. Then, the responsivity (R) can be expressed by,

$$R = \frac{I_{photo} - I_{dark}}{P_{inc}} = \frac{\Delta I}{P_{inc}} = \eta \frac{q}{h\upsilon} \left(\frac{\tau_{eff}}{t_n} + \frac{\tau_{eff}}{t_p}\right) \tag{9}$$

The gain for photoconductors can be obtained by the following equation,

$$Gain = \tau_{eff}\left(\frac{1}{t_n} + \frac{1}{t_p}\right). \tag{10}$$

1.3.2 Photodiodes

Photodiodes consist of a simple *pn* or *p*-*i*-*n* junction. Once the light is absorbed in the junction, the photo-excited carriers are generated. By sweeping to electrodes, photocurrent is created. The operation types of photodiodes can be classified into i) Schottky photodiode, ii) *pn* photodiode, iii) *p*-*i*-*n* photodiode, and iv) Avalanche photodiode.

The Schottky diode is a semiconductor diode that is formed by the junction of a semiconductor with a metal. It has been widely utilized in both academic and industrial areas due to its easy fabrication. In addition, the diode operates at low forward/reverse bias voltage, allowing high switching action. The *pn* photodiode has taken attention from the current industrial markets for a few decades, although it is not the advanced type comparing with others. The depletion region between *p*- and *n*-type regions, known as the deletion region, acts as the absorption region. However, the deletion region is shallow so that the light signal is not effectively absorbed. Thus, the intrinsic layer is inserted between *n*- and *p*-type regions of the *pn* photodiode, becoming a *p*-*i*-*n* structure. Since the depletion region increases owing to the intrinsic layer, the light can be effectively collected in the absorption layer.

However, at weak light power, the *p-i-n* photodiode would not be sufficient to collect the light signal. In this case, avalanche photodiodes have been introduced. The avalanche photodiode is a highly sensitive photodiode invented by Japanese engineer Jun-inch Nishizawa in 1952. The avalanche photodiode contains the absorption and multiplication layers separately or together. Once the light generates photo-excited carriers in the absorption layer, the carriers start to be accumulated in the multiplication layer, leading to the gain of >1. However, the noise level is high, resulting from the accumulated carriers in the multiplication layer.

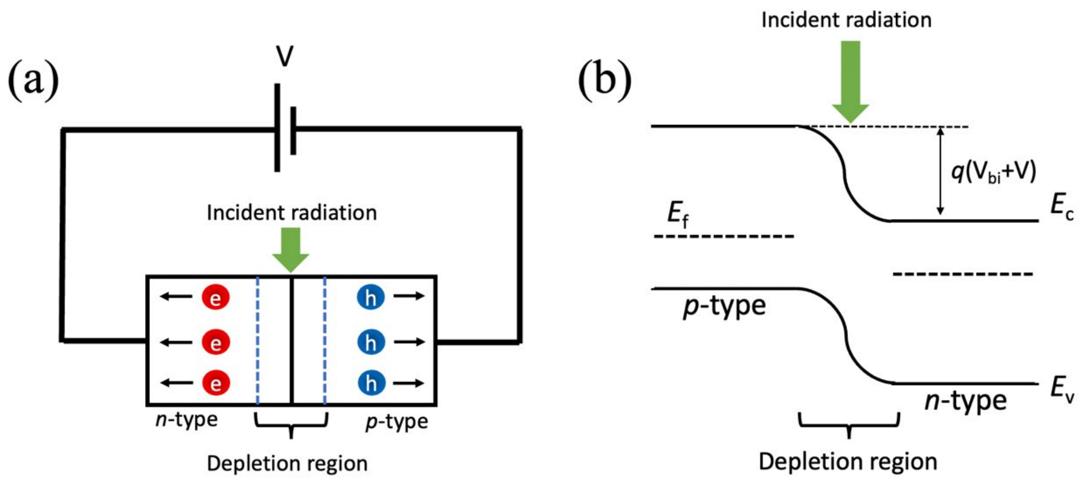

Figure 11. (a) Geometry and bias of a *pn* junction. (b) The band diagram of a *pn* junction.

The geometry and the band diagram of a *pn* junction are shown in Figure 12 (a) and (b), respectively. As mentioned above, the pn photodiode consists of *n*- and *p*-type regions along with the depletion region at the center. The depletion width (W_d) can be defined as follow,

$$W_d = \sqrt{\frac{2\varepsilon_r\varepsilon_0 V_{bi}}{q}(N_A + N_D)/N_A N_D} \quad (11)$$

where ε_0, ε_0, V_{bi}, N_A, and N_D are the dielectric constant in free space and a semiconductor, the built-in voltage, the donor and acceptor doping concentrations, respectively. The dark current can be obtained by the following expression,

$$J_{dark} = q\left(\frac{D_n}{L_n}\frac{n_i^2}{N_A} + \frac{D_p}{L_p}\frac{n_i^2}{N_D}\right)\left(e^{\frac{qV}{kT}} - 1\right) = J_0\left(e^{\frac{qV}{kT}} - 1\right) \quad (12)$$

where D_n, n_i, L_n, D_p, L_p, k, T, and J_0 are the minor carrier diffusion constant for electrons, the intrinsic concentration, the diffusion length in the *n*-type region, the minor carrier diffusion constant for holes, the diffusion length in the *p*-type region, Boltzmann constant, temperature, and saturation dark current density, respectively. Under illumination, the photon current density can be expressed by the following equation,

$$J_{photo} = J_0\left(e^{\frac{qV}{kT}} - 1\right) + q\left(W + L_n + L_p\right)G_0 = J_0\left(e^{\frac{qV}{kT}} - 1\right) + q\eta\frac{P_{inc}}{h\nu}. \quad (13)$$

The responsivity can be obtained by the following equation,

$$R = \frac{I_{photo} - I_{dark}}{P_{inc}} = \eta\frac{q}{h\nu}. \quad (14)$$

1.3.3Phototransistors

The working principle of phototransistors is almost similar to the one for photodiodes but includes an amplifying transistor. The incident photon generated the photo-excited carriers on the base of a phototransistor. Then the carriers are amplified electrically like the normal transistor acts by an electrical signal. Thus, the phototransistor can produce a high responsive gain compared to a photodiode. However, the major constraint is low response time. Since the electrical bandwidth restricts the amplification, low bandwidth mainly constrains the frame rate for a remote sensor. Second, the high leakage current multiplied by the DC current gain of the transistor is not suitable to detect the weak light power signal. Third, the temperature variation modulates the performance unexpectedly, implying that the cooling system might be additionally required to make the output data of phototransistors consistent. The overall features for a photodiode and a phototransistor are compared in Table 1.

Parameters	Photodiode	Phototransistor
Spectra Coverage	Broad	Short
Gain	Low	High
Linearity	High	Low
Dark Current	Low	High
Response speed	High	Low

Table 1. The summarized performance comparison between a photodiode and a phototransistor.

1.4 Motivation and Objectives of the Thesis

The selection of appropriate spectral windows is essential to decide the feasibility of applications. For example, optical fiber communication requires broadband operations, including the NIR and MIR ranges, e.g., 800, 1,300, 1,550, and 2,000 nm, due to the attenuation characteristics of fibers. The wavelengths of 905, 940, and 1,550nm are chosen for LiDAR operation to avoid damage to human eyes. Also, a gas sensor prefers to make use of NIR or MIR ranges for molecular detection. This thesis mainly focuses on the wavelength range of 1,550 to 2,000 nm (or beyond) in which the diverse applications are interested.

Si is an abundant element on Earth, which is required for diverse applications. Up to date, Si is the primary material element to compose memory chips, computer processors, transistors, and all other electronic devices in current industries. Si photonics is also a trending topic because Si has already been studied and investigated in decades. Present technology allows providing high crystalline Si on a large scale. However, Si is an indirect material with a bandgap of 1.1 eV, corresponding to 1,100 nm of wavelength. Although Si can provide a transparent wavelength window beyond 1,100 nm, it is difficult to support photoemission and photodetection in wavelength beyond 1,200 nm. To extend operation wavelength, III-V compound semiconductors are essential. III-V semiconductor systems benefit from their fast carrier dynamic, high absorption coefficient, and direct bandgap characteristics. III-V compound semiconductors dominate the current industry for PICs. However, manufacturing III-V semiconductor for PICs is expensive and CMOS-incompatible. Also, the complexity of fabrication is high, and III-V material systems constraint the efficient integration of electronic and photonic devices on one chip.

Germanium (Ge) is one of the Group IV elements, benefiting from CMOS compatibility and cost-effectiveness. Ge has a direct bandgap (Γ valley) of 0.8 eV along with an indirect bandgap (L valley) of 0.66 eV. The narrow Ge bandgap enables photodetection beyond 1,100 nm. The cut-off wavelength of bulk Ge photodetectors is 1,550 nm, suitable for NIR photodetection. Therefore, Ge is an alternative to replace III-V materials. Figure 12 represents the absorption coefficient for diverse materials as a function of wavelength and energy. Si absorption coefficient remains up to ~1,100 nm while the Ge absorption coefficient sustains beyond 1,100 nm wavelength. In addition, the Ge coefficient values are comparable with those of InGaAs semiconductor systems.

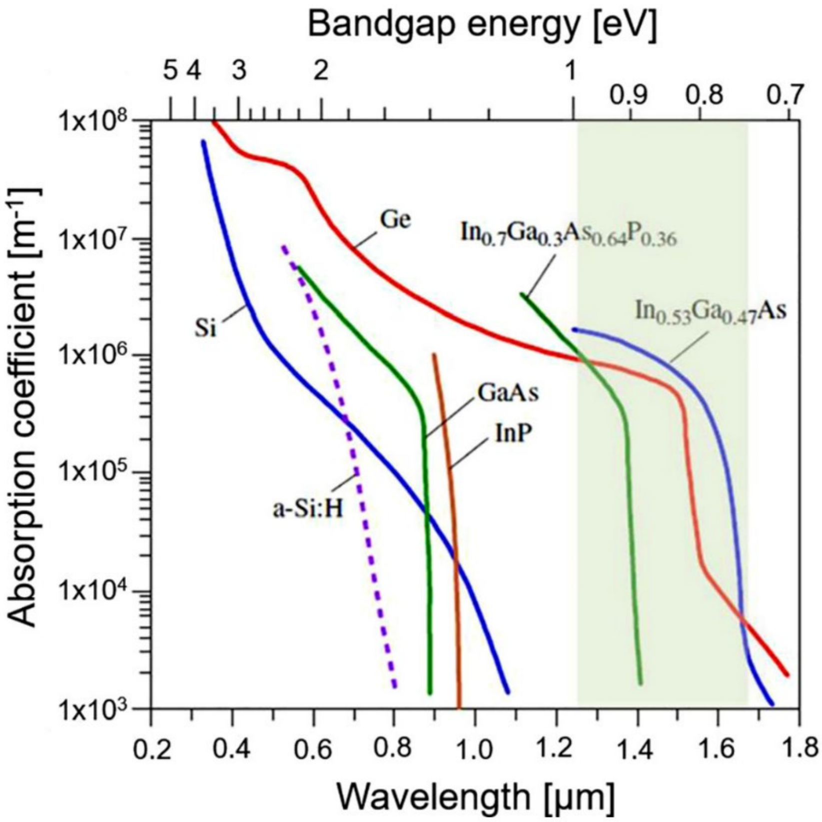

Figure 12. The absorption coefficient for mainstream materials of integrated photonics, e.g., Si, Ge, InGaAs, etc., with respect to wavelength and converted energy [16].

To extend the operation wavelength into the MIR range, germanium-tin (GeSn) alloys composed of Group IV elements have been proposed. The introduction of tin (Sn) into Ge shrinks the bandgap so that the bandgap is tunable depending on the Sn contents in Ge. Moreover, a transition from indirect to direct bandgap is introduced with Sn contents of >8%, opening up the opportunity for a Group-IV monolithic light source, which has lacked for Group IV monolithic electro-photonic integration. Figure 13 displays the absorption coefficients for GeSn alloys along with the Ge reference. The absorption coefficient for Ge decreases at 1,550 nm drastically. As the Sn content increases in GeSn alloys, the absorption coefficient is extended accordingly. A GeSn alloy with the Sn content of 1% shows the bandgap at 1,600 nm and extends beyond 2,000 nm when the Sn content is higher than 8%.

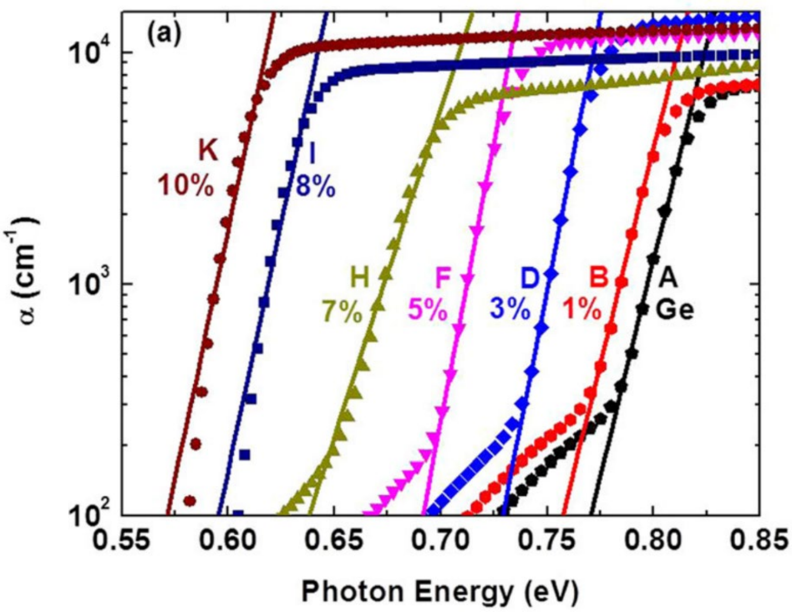

Figure 13. Extracted absorption coefficient (α) for Ge and GeSn alloys with varying Sn contents from 1 to 10% (B to K) [17].

As such, Ge and GeSn material systems are strong candidates for NIR and MIR range photodetection. In addition, Group IV monolithic PICs are low-cost in manufacturing. Therefore, tremendous research on Ge/GeSn-based optical devices has been explored recently. However, the performance of GeSn/Ge photodetectors is away from commercial bulk Ge and III-V semiconductor photodetectors. In general, they suffer from high dark leakage current densities of >10 mA/cm^2 and low responsivities of <0.5 A/W for normal-incidence photodetectors with *i*-Ge/GeSn thicknesses of <500 nm. Thus, lowering dark current densities and enhancing optical responsivities are desirable for high-performance GeSn/Ge photodetectors.

In this thesis, high-performance Ge/GeSn photodetectors will be studied to improve their responsivity, dark current, and frequency response. Ge/GeSn photodetectors will be demonstrated with on-insulator platforms, i.e., Ge-on-insulator (GOI) and GeSn-on-insulator (GeSnOI) platforms. For NIR range photodetection, a Ge photodetector will be introduced. In order to reduce dark current density, the mitigation of dislocations/surface defects and their dependence on photodetector performances will be described in Chapter 3. Furthermore, hole array structures will be addressed to improve optical responsivity for Ge photodetectors in Chapter 4. With the advanced techniques, specific detectivity for proposed Ge photodetectors is comparable to commercial bulk Ge and extended-InGaAs photodetectors. For MIR range photodetection, GeSn alloys with varying Sn contents will be addressed. It is found that GeSn with ~7% of Sn contents allows photodetection beyond 2,000 nm. Also, the mitigation of a GeSn/Ge interface is conducted. First, GeSn layer thickness increases to mitigate trap-related carrier dynamics, leading to improved EQE in Chapter 5. Second, GeSnOI platforms will be introduced to eliminate the GeSn/Ge interface in Chapter 6. The proposed GeSn/Ge photodetectors in this thesis are potentially promising for CMOS compatible and low-cost photodetection for Si-based PICs.

1.5 Major Contributions

The major contributions of this thesis are listed as follows:

- Demonstrated vertical *p-i-n* Ge photodetectors with a dark current density of sub-mA/cm^2 on an annealed GOI platform.
- Reduced bulk leakage current by 300× for vertical *p-i-n* Ge-on-insulator photodetectors by alleviating threading dislocation density (TDD).
- Suppressed surface leakage current from 5.7 to 0.5 μA/cm, which is reduced by 12× for vertical *p-i-n* photodetectors via ozone (O_3) oxidation. 3dB bandwidth was improved from 0.88 to 1.72 GHz, which is enhanced by 2×.
- Improved optical responsivity up to 0.74 A/W with gourd-shaped hole array structures. The gourd-shaped hole array provided high optical absorption compared to cylinder-shaped hole array structures. The estimated specific detectivity was superior to that of commercial Ge bulk and extended-indium galilium arsenide (InGaAs) photodetectors.
- Adopt GeSn alloys to extend cut-off wavelength into the MIR range. It was revealed that GeSn alloys with 7.1% of the Sn content enable photodetection beyond 2,000 nm.
- Revealed that trap states near GeSn/Ge interface contributed to the degradation of EQE and leakage current. The impact of interface defects could be mitigated by increasing GeSn thickness.

- Proposed GeSnOI platforms to improve the optical and electrical performances. The demonstrated photodetectors with 9% Sn content provide the responsivity of 0.06 A/W at the wavelength of 2,003 nm.

1.6 Organization of the Thesis

Chapter 2 describes GOI/GeSnOI platforms and the state-of-the-art GeSn/Ge photodetectors. GeSn/Ge growth will be addressed, and advanced Ge/GeSn layer transfer techniques will be introduced. The advantages of on-insulator platforms will be emphasized, and GeSn/Ge photodetectors will be reviewed in chronological sequence.

Chapter 3 gives a dark current study on the varying TDDs and surface quality in Ge photodetectors. Also, the sub-mA/cm^2 dark current density is realized for Ge photodetection with low TDD GOI and germanium-oxide (GeO_x) surface passivation.

Chapter 4 focuses on improved responsivity and specific detectivity for Ge photodetectors with hole array structures. It reveals that gourd-shaped hole array structures display high optical absorption in comparison with cylinder-shaped ones. A hole array structure is optimized based on various parameters via simulation and photodetectors are demonstrated accordingly.

Chapter 5 lays the introduction of GeSn photoconductors for MIR range photodetection. It is observed that trap-states near GeSn/Ge interface dominate optical/electrical carrier dynamics. GeSn thickness will vary to mitigate trap-related carrier dynamics. The increases in thickness can enhance EQE by 10× comparing with a think one. A systematic study on defect management is conducted.

Chapter 6 elaborates on metal-semiconductor-metal photodetectors on a GeSnOI platform. The photodetectors enable photodetection beyond 2,000 nm.

Chapter 7 summarizes the results in this thesis and proposes future directions.

Chapter 2. On-insulator Platforms for Ge/GeSn Material Systems and their State-of-the-art Photodetectors

In Chapter 2, GOI and GeSnOI platforms are proposed, taking advantage of improved optical and electrical confinements, and the state-of-the-art Ge/GeSn photodetectors are reviewed. Chapter 2.1 will address the Ge/GeSn growth, and the demonstration of on-insulator platforms will be introduced along with benefits of insulators in Chapter 2.2. GeSn/Ge photodetectors will be reviewed in Chapter 2.3. Chapter 2.4 summarizes the contents in Chapter 2.

2.1 Epitaxial Growth of Ge and GeSn Alloys on Si Substrates

This section begins with Ge/GeSn growth methods. Chapter 2.1.1 discusses the Ge growth. GeSn growth methods are addressed in Chapter 2.1.2.

2.1.1 Ge Growth on Si Substrates

Ge growth on a Si substrate was developed with a SiGe graded buffer layer in the 1980s [18]. The graded buffer layer was to minimize damage to a top layer, originated from the large lattice mismatch of 4.2% between Si and Ge. Optimized SiGe buffer layers reduced threading dislocations (TDs) in a Ge film [18]. However, additional chemical mechanical polishing (CMP) process was necessary to smoothen due to a rough surface of Ge films. After that, Ge was grown directly on Si substrate using a two-step deposition technique via a chemical vapor deposition (CVD) process [21]. The two-step growth method requires a low-temperature process to grow a thin Ge seed layer, followed by high-temperature growth to improve crystallinity. Low temperature ranges between ~320-450°C to accumulate misfit defects at seed layers. High-temperature growth requires a temperature ranging from ~600 to 850°C. Extra-step, known as a three-step growth technique, can further reduce TDs by thermal cyclic annealing in hydrogen (H_2) at high-temperature [24]. The three-step growth method can reduce TDD to the order of 10^7 cm^{-2}.

Recently, an arsenic (As)-doped Ge seed layer has been introduced to reduce TDD down to $< 5 \times 10^6$ cm^{-2} [26]. As-doped Ge films enhance the velocity of dislocations so that many dislocations move away to the edge or the surface of a wafer. Other methods for high-quality epitaxial Ge growth have been introduced, such as low-energy plasma-enhanced CVD or selective epitaxial growth, and so on [27]. The proposed Ge growth methods are capable of being used in optoelectronics foundries on a wafer scale.

2.1.2 GeSn Alloy Growth

Alloying Sn with Ge suffers from low solubility of Sn into Ge (~1%). Therefore, low-temperature growth methods have been developed to increase GeSn stability in high Sn contents. In addition, an epi-Ge layer serves as a strain-relaxed buffer (SRB) layer to mitigate the lattice mismatch between GeSn and Si. Menendez and Kouvetak proposed a GeSn film growth via CVD in the early 2000’s [30]. Two types of Sn gas sources, (Ph)SnD_3 (Ph-C_6H_5; phenyl, and D-deuterium) and tin deuteride (SnD_4) via ultra-high vacuum chemical vapor deposition (UHV-CVD), were used to increase epi-GeSn stability. After that, an H_2-diluted SnD_4 source was utilized to induce even higher epi-GeSn stability. In 2011, high-quality GeSn alloys with the Sn content as high as 8 % were grown using tin chloride ($SnCl_4$) and digermane (Ge_2H_6) gas precursors in a CVD reactor [33]. Since then, the $SnCl_4$ and Ge_2H_6 precursors have been widely adopted for GeSn alloy growth with low-cost and wafer-scale growth.

Molecular beam epitaxy (MBE) was used to deposit GeSn alloy films with the Sn content between 0 and 12.5% directly on Si (001) substrates at 160 °C in 2011 [35]. After that, the SRB layer was inserted between GeSn/Si before GeSn alloy growth to minimize dislocation generation. Sputtering epitaxy is one of the promising wafer-scale growth methods for GeSn alloys. This method provides a solid phase epitaxy state for the growth, offering great potential for cost-effective GeSn mass production. Pérez Ladrón de Guevara *et al.* reported that GeSn films were achieved on Ge substrate via sputtering [37]. After that, a GeSn film was grown directly on Si substrates as well [38]. However, the quality of GeSn film via sputtering is still far away from the ones via MBE and CVD. Diverse novel GeSn growth techniques have been developed as well in parallel efforts [39].

2.2 On-insulator Platforms for Ge/GeSn Material Systems

This section aims to review practical values and potential techniques to realize single-crystalline Ge/GeSn on insulator platforms. Chapter 2.2.1

describes the advantages of insulator substrates. Subsequently, various methods for the demonstration of Ge/GeSn-on-insulator platforms will be addressed in Chapter 2.2.2.

2.2.1 Advantages of On-insulator Platforms for Integrated Photonics

Several GeSn/Ge growth methods were discussed in the previous section. The next question becomes what efficient substrates are to utilize high-quality GeSn/Ge materials. Among diverse approaches, on-insulator substrates are largely investigated in this section. Insulators under GeSn/Ge produce the isolation of electrical carrier dynamics and improved optical confinement due to their large bandgap and low refractive index.

The improved optical confinement for on-insulator platforms has been reported in integrated photonics fields [41]. Vertical-cavity resonance modes in on-insulator platforms enhance photodetection and photoemission. Soumava Ghosh *et al.* observed vertical-cavity effects on a photodetector [41]. Figure 14(a) and (b) display simulated reflectivity and responsivity for GOI and Ge-on-Si (GOS) photodetectors. Electric field distribution in GOS and GOI platforms is illustrated in Figure 14(c) and (d), respectively. Highly-confined electric field distribution in GOI platforms is observed in Figure 14(c), resulting from vertical resonance modes.

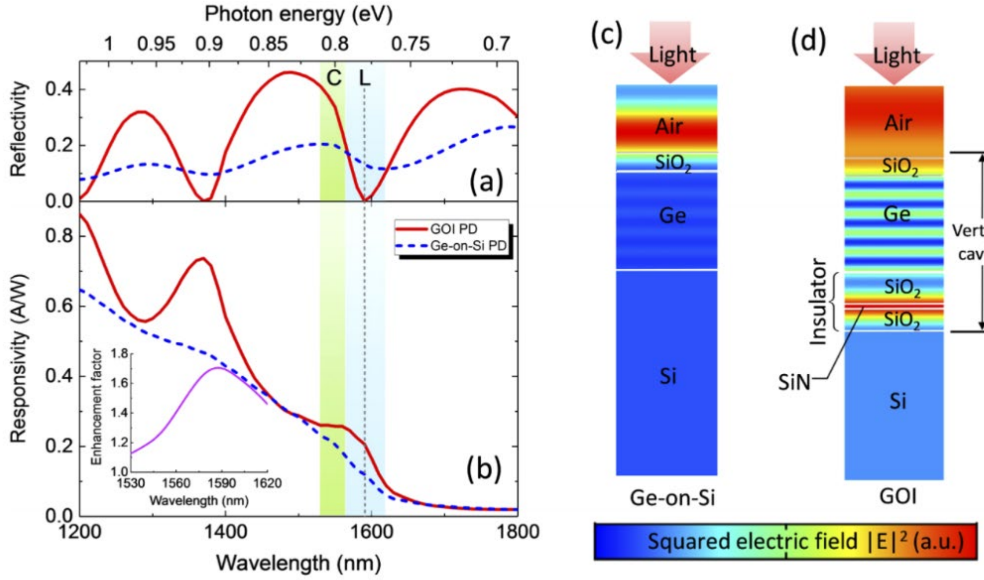

Figure 14. (a) Simulated reflectivity and (b) responsivity spectra for GOI and GOS photodetectors via finite-difference time-domain (FDTD) simulation. Inset in Figure 14(b) displays the responsivity improvement for the GOI photodetector. Simulated electric field distribution in (c) GOS and (d) GOI platforms [41].

Vertical resonance modes in on-insulator platforms can improve the performance of light-emitting devices. Bo-Jun Huang *et al.* reported the vertical GeSn light-emitter diode (LED) on the insulator platform [43]. Figure 15(a) and (b) display electroluminescence (EL) spectra along with the reflectivity spectra of the GeSn on SOI and the GeSn-on-Si platforms, respectively. The EL study revealed that EL peak intensity was improved by ~6.31×, signifying that vertical-cavity effects improved optical confinement, leading to enhanced radiative recombination rate.

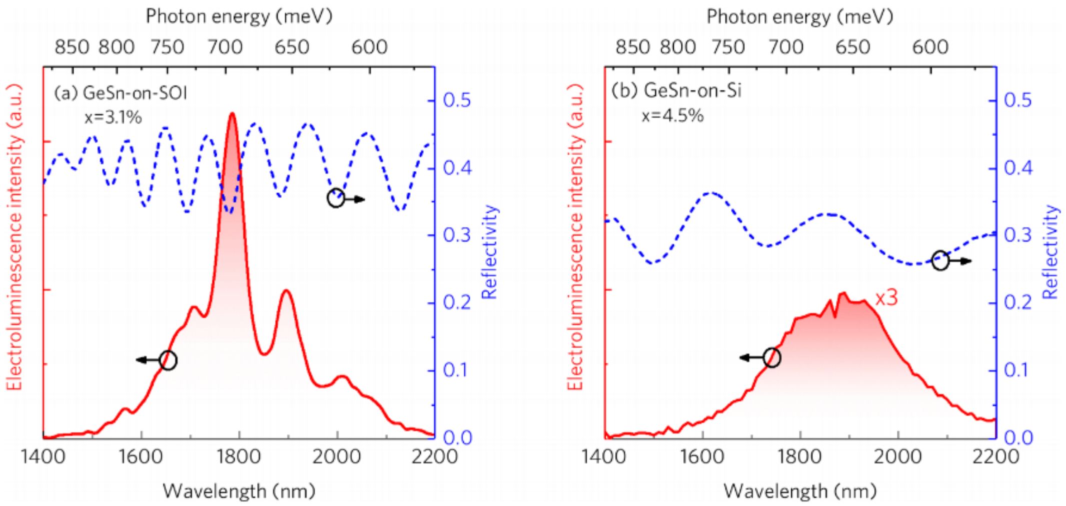

Figure 15. EL and reflectivity spectra for GeSn (a) on-insulator platform and (b) on-Si platforms [43].

On-insulator platforms are good candidates for waveguide construction due to the large refractive index gap between a semiconductor and an insulator. Waveguide propagation loss is partially determined by core-index contrast [44]. Figure 16(a) displays propagation losses for GOS and Ge-on-silicon nitride (GON) waveguides. The estimated losses for the GON and the GOS waveguides were 7.86 and 7.28 dB/cm, respectively, despite a high evanescent field fraction. Insets in Figure 16(a) display optical density distribution in waveguides. The GOS waveguide provides a low core-clad index contrast. In contrast, GON platforms provide high core-clad index contrast, promising for a low loss waveguide. Figure 16(b) represents the cross-sectional SEM view for GON waveguides.

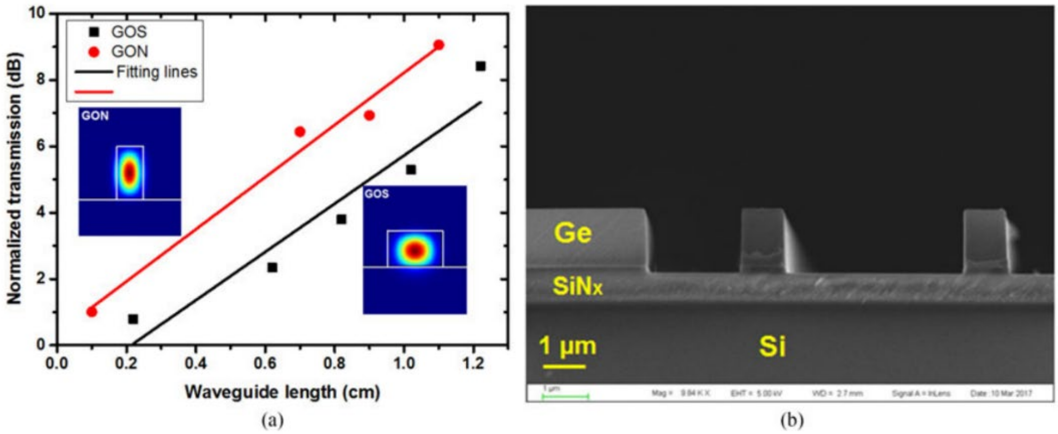

Figure 16. (a) The transmission loss for Ge waveguides on Si and SiN platforms. The insets display the electric field distribution in the cross-sectional dimension of waveguides. (b) The cross-sectional SEM image of the GON waveguides [45].

Electrically pumped GeSn/Ge light sources are the missing parts to realize the Si-based Group-IV monolithic integration. Electrically pumped Ge laser was first demonstrated on Si substrate by R. E. Camacho-Aguilera *et al.* in 2012 [46]. The key concept was to fill up electrons in *L* valley through heavily *n*-type doping, resulting in enhanced radiative recombination in *Γ* valley. Since then, electrically pumped GeSn lasers were first demonstrated on Si substrate by Yiyin Zhou *et al.* in 2020 [47]. GeSn with direct bandgap serves as a gain medium, and the edge of the gain medium severs as mirrors to support stimulated emission modes. Ge/GeSn lasers suffered from a high threshold current for lasing (~300 kA/cm^2 for Ge, 598 A/cm^2 for GeSn). Therefore, numerous efforts have been put to obtain ultra-low or III-V laser comparable threshold current. One of the most representative cases for low threshold current GeSn lasers was demonstrated on suspended and insulator-surrounding structures, as shown in Figure 17(a) [48]. An indirect bandgap GeSn medium is transited to a direct bandgap by employing strain engineering using a SiN stressor in Figure 17(c). As a result, the PL peak shifted and the intensity of the PL peak was significantly enhanced in Figure 17(b). It should be noted that the removal of a defective region near a GeSn/Ge interface contributed to the ultra-low threshold current for lasing.

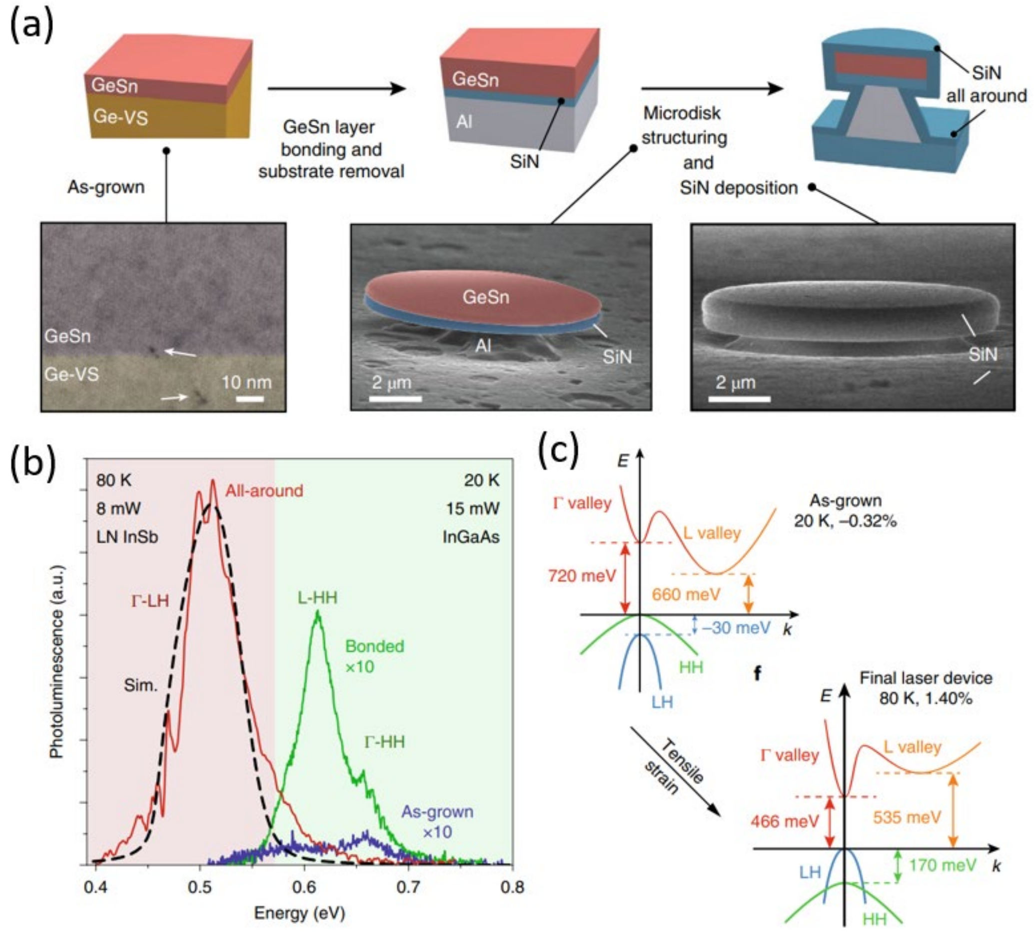

Figure 17. (a) Top: schematic images of as-grown GeSn, GeSn on insulator, and complete GeSn disk laser. Bottom: transmission electron microscopy (TEM) image for as-grown GeSn and SEM images for under-etched GeSn and the final laser structure with SiN_x all around. (b) PL (photoluminescence) spectra at 20 K for as-grown, bonded layer and the final GeSn micro-disk laser with the all-around stressor at 80K. (c) Top: band structure for as-grown GeSn. Bottom: bandgap structure for strained GeSn layer with all-around stressor [48].

Shuyu Bao *et al.* claimed that GOI benefited from the isolation of electrical dynamics [49]. Figure 18 represents the current density-voltage (*J*-*V*) curve for metal-oxide-semiconductor (MOS) structures on GOI in comparison with GOS platforms. Leakage currents are reduced for the GOI platform. Al_2O_3 layers have a bandgap of 6.36 eV, meaning that the insulator acts as a barrier layer to avoid carrier diffusion from Si to Ge.

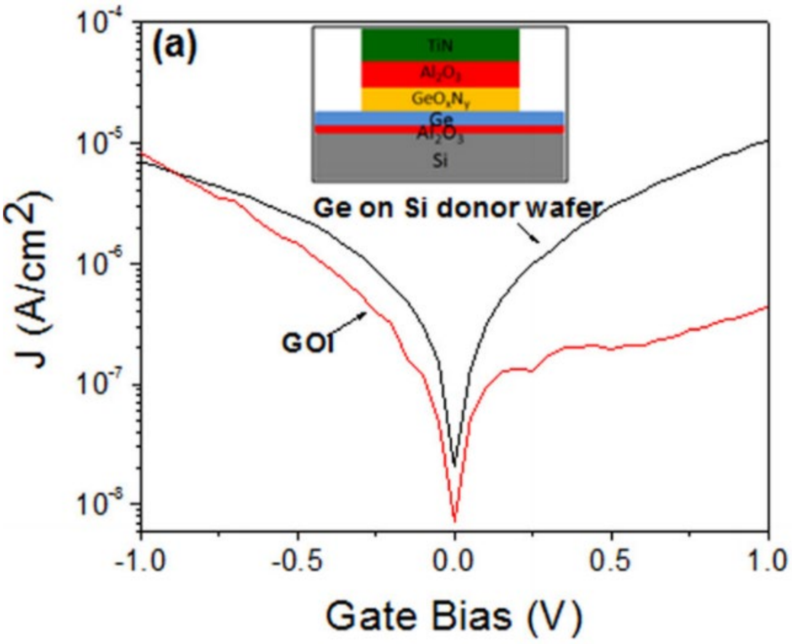

Figure 18. The *J-V* curve characteristic for MOS structures demonstrated on GOI comparing with the one on a Si substrate [49].

2.2.2 Demonstration of On-insulator Platforms for Ge/GeSn Material Systems

Since numerous optical devices demonstrated on insulator platforms improve their optical and electrical properties, it is essential to focus on methods for the demonstration of on-insulator platforms with high-quality Ge/GeSn. Up to date, epitaxial Ge/GeSn layers have been grown directly on Si-on-insulator platforms [42]. This method takes advantage of easy growth and its compatibility with front-end-of-line (FEOL) integration. Because GeSn/Ge growth directly on Si substrate had been investigated for more than decades, the same growth on an SOI platform is straightforward to achieve. However, recently trap states near GeSn/Ge/Si interfaces have been observed to degrade the performance of optical devices [48]. Therefore, epi-

GeSn/Ge on insulator platforms with the removal of interface defects is required. Ge condensation, rapid melting growth, lateral over-growth, bonding, and layer transfer have been introduced to demonstrate GOI platforms [39]. Most methods require a high-temperature process except for bonding and layer transfer techniques, and the smart cut methods, which are conducted in the temperature range from 300 to 600°C. Although the methods are widely investigated for the GOI platforms, it challenges to directly employ the GeSnOI platform due to the low thermal budgets of GeSn. The thermal stability of GeSn alloys is determined by various parameters, e.g., Sn content, crystal quality, and stain. Therefore, the low temperature process should be conducted to avoid Sn segregation/ precipitation. It should be noted that GeSn alloy with the Sn content of 7.82% was degraded after the thermal annealing at > 400°C [50].

A transfer-printing technique is favorable in terms of excellent mechanical flexibility and material quality. Figure 19 displays the overall transfer-printing technique process for GeSn nanomembrane (NB) formation. The transfer technique requires a buried oxide (BOX) layer as a sacrificing layer for an undercutting process. In addition, a hole pattern in GeSn is required for wet etching of a BOX layer. This method can be conducted at room temperature fabrication steps to achieve strain-free GeSn. Furthermore, a transferred GeSn layer is implemented by an additional process such as CMP or RIE processes to remove a defective region between GeSn/Ge. However, the transfer-printing technique for the GeSn film transfer has been mainly conducted on a chip scale. There is still room for further research on transfer-printing technique in wafer-scale for GeSn films.

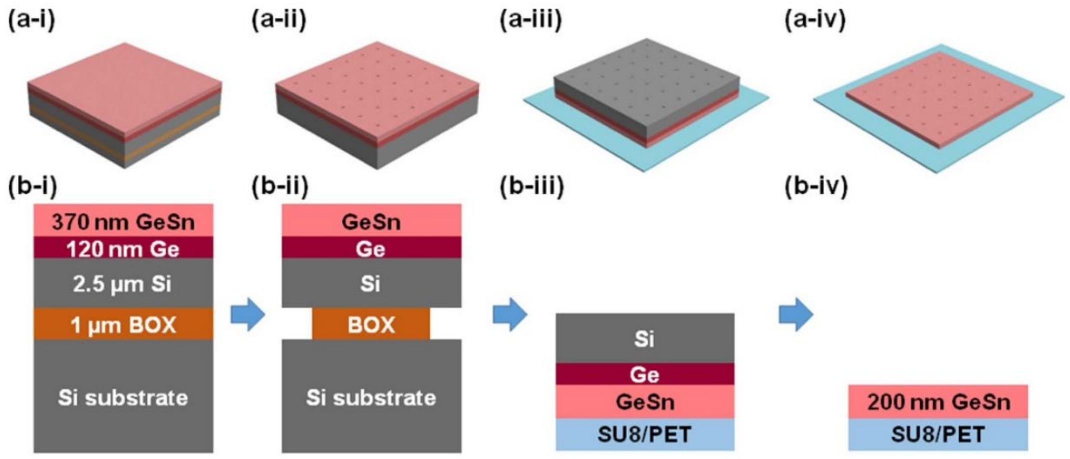

Figure 19. (a) The schematic images for fabrication flows of GeSn NMs; (a-i) Growth of GeSn, (a-ii) Patterning NMs with a hole array for undercut process., (a-iii) Flip-transferring of 3 × 3 mm^2 sized GeSn NMs on SU-9 2002 coated PET substrates, (a-iv) Preparation of GeSn NMs by etching down all the wat to the GeSn layer. (b) Corresponding cross-sectional view for each fabrication steps [51].

DWB and layer transfer techniques are promising for realizing a GeSnOI platform on a wafer scale [52]. This method requires two Si wafers, i.e., a handle wafer and a donor wafer. Ge/GeSn is grown on the donor wafer and insulators are deposited on the wafer pair. Subsequently, they are attached via a bonding process. After that, the sacrifier layer is removed away. This method requires low temperature (~300 °C), meaning that Sn segregation can be avoided. More importantly, a wafer-scale layer transfer is available, which is favorable to optoelectronic foundries. For integration on a chip, back-end-of-line (BEOL) integration is preferred. The detail in schematic flows for the transfer process is shown in Figure 20. The proposed photodetectors in this thesis were demonstrated by using the DWB and layer transfer techniques, taking advantage of the wafer scale method and low temperature process.

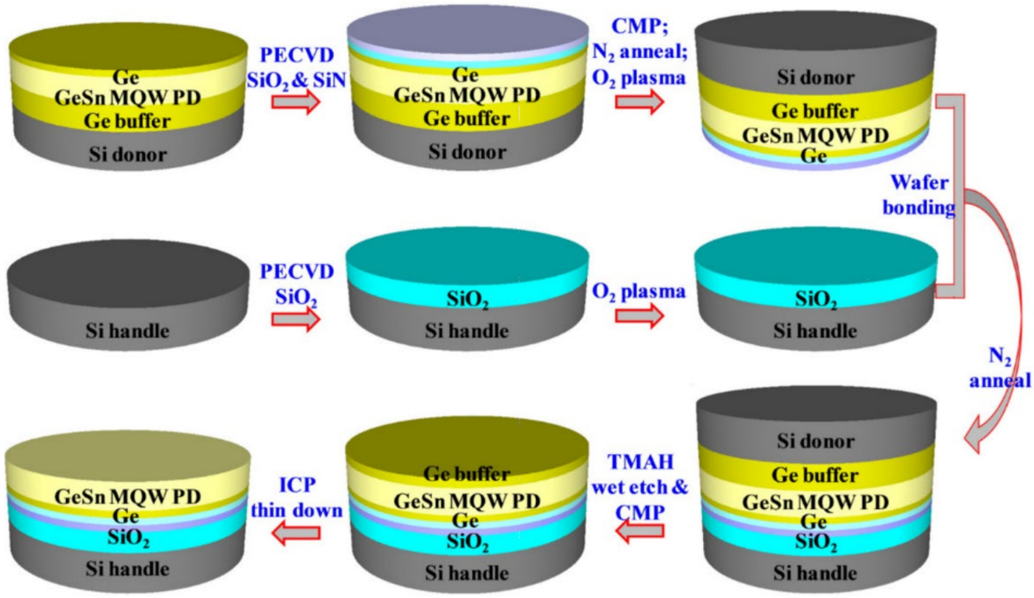

Figure 20. Overall fabrication flows for the demonstration of GeSn-Ge-on-insulator platforms via wafer bonding and layer transfer technique with 200 mm wafer-scale [53].

GeSn growth on gadolinium oxide (Gd_2O_3) insulator is also a promising breakthrough for GeSnOI on a wafer scale [54]. A thin Gd_2O_3 layer on Si (111) substrate is required for Volmer-Weber growth mode, which allows a top GeSn layer to be formed via GeSn islands. As growth time increases, two-dimensional (2D) growth allows increasing thickness. In the meantime, GeSn growth continuously begins in the Volmer-Weber growth mode at the bottom.

2.3 Ge/GeSn Photodetectors

2.3.1 Ge Photodetectors

John N. Shive reported a Ge bulk phototransistor with a quantum yield of 100 for the *n-p-n* structure in 1953 [55]. Subsequently, avalanche Ge bulk photodiodes were demonstrated to extend detection wavelength in 1966 [56]. After that, Ge had not received much attention compared to III-V photodetectors. In the 1980s, once Si photonics came into the lime light, Ge-based devices were back as a strong candidate for integrating with Si-based components. Since then, many electrical and optical Ge components were reported primarily with epitaxial phase Ge on Si substrate.

Epitaxial Ge photodetectors were demonstrated in 1984 [18]. Graded Ge_xSi_{1-x} layers on Si substrate with a highly doped layer on a top Ge layer were proposed to mitigate dislocations generation. Although a quantum efficiency for the photodetector was as high as 41% at 1,450 nm wavelength, dark current density was high (~50 mA/cm^2). In the late 1990s, Ge photodetectors on optimized relaxed graded SiGe layers with low TDD were reported [57]. By growing thick graded SiGe layers, dark current density was reduced by ~250×. However, the photodetector suffered from low responsivity.

In 2000, Ge photodetectors were demonstrated directly on Si substrate without a graded SiGe layer [58]. A three-step growth technique was introduced to reduce TDD. The responsivity was enhanced by ~20× at 1,300 nm as TDD was reduced from 7×10^{-8} to 3×10^{-6} cm^{-2}, meaning that responsivity is related to TDD. The growth of a thick Ge layer was introduced to improve responsivity furthermore [59]. A 3.8 μm thickness of an epitaxial Ge layer provided the high responsivity of 0.75 A/W at 1,550 nm. However, dark current density was still high (15 mA/cm^2 at -1 V) due to many dislocations/defects formed in epi-Ge. Once optical bandwidth was attracted for optical networks, many efforts had been put on optical bandwidth improvement. One of the simplest ways to improve bandwidth is to reduce a photodetector mesa. S. Klinger *et al.* reported that a Ge photodetector on a small scale displayed the 3dB bandwidth of 49 GHz at -2 V [60]. A small mesa diameter (10 μm) and an intrinsic thickness (330 nm) contributed to high 3dB bandwidth for the photodetector. After that, no significant improvement for photodetectors has been explored for a Ge photodetector on Si substrate. Recently, a single-photon avalanche photodetector was reported on a GOS platform for Geiger mode operation [61].

On-insulator platforms bring about improved optical absorption, as described in Chapter 2.2.1. For instance, waveguide photodetectors are mainly demonstrated on insulator platforms with high responsivity, fast frequency response, and high sensitivity. A waveguide photodetector has separated light and carrier paths, meaning that a trade-off between 3dB bandwidth and responsivity can be vanished in designing a photodetector. Normal incidence vertical *p-i-n* photodetectors also gain from insulator platforms. An insulator shows a low refractive index, while Ge contains a high refractive index of ~4. Thanks to the large refractive index gap between them, a high optical field distribution can be confined in Ge, leading to enhanced absorption.

Ge photodetectors on SOI platforms have been intensively introduced [62]. Despite a thin intrinsic Ge layer, high responsivity was achieved. Conventionally, vertical resonance modes with insulator platforms improve optical absorption. Recently, micro- and nano-hole array has been patterned into photodetectors. The hole array scatters light laterally, so that lateral resonance modes also improves the absorption spectra. The micro-hole array structured Ge photodetector displays the high responsivity of 0.91 A/W at

1,550 nm wavelength [63]. Besides, the nano-hole array structure was also suggested to prove that the vertical and lateral resonance modes improved the responsivity for the photodetectors [64]. The dual-absorption Ge photodetector was proposed for high-frequency response [65]. The various types of Ge photodetectors are shown in Figure 21(a)-(d).

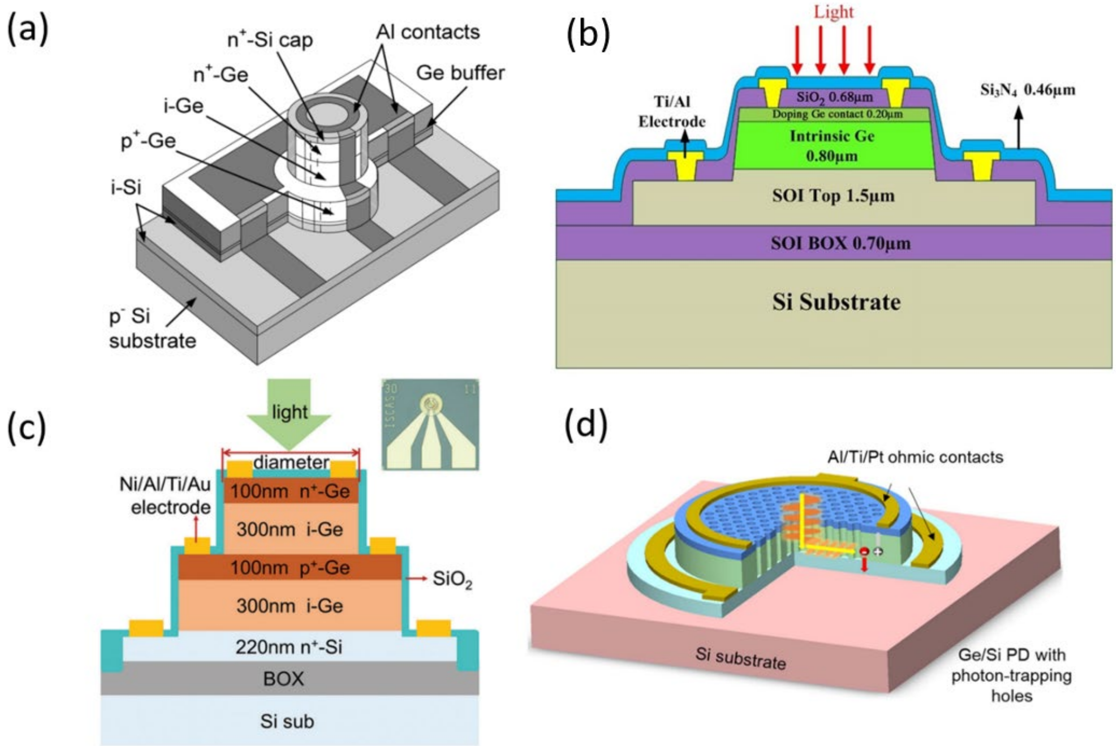

Figure 21. 3D schematic images of Ge photodetectors (a) on Si substrate platform [60], (b) on SOI platform [62], (c) on SOI platform with dual-absorption structure [65], and (d) on SOI platform with photon-trapping hole structures [63].

The Ge photodetectors on the SOI platform suffer from high leakage current due to many dislocations. It has been widely known that the SRH-related tunneling/generation mechanisms govern the dark leakage current for the photodetectors on the SOI platform. The defects formed in the intrinsic layer act as trap states. Due to the thermal excitation or tunneling through the trap states, the leakage current highly increased. This is because main defects are formed at the near Ge/Si interface. Ge photodetectors on GOI platforms have been promising to manage the interface layer [66]. For the GOI platform, the interface layer could be efficiently removed during the layer transfer process. This potentially implies that the dark leakage current and responsivity can be improved.

2.3.2 GeSn Photodetectors

Since MIR range photodetection is attractive to diverse applications, cut-off wavelength extension for Ge photodetectors is desirable. Strain engineering is one of the promising methods to shrink the Ge bandgap [67]. In addition, GeSn alloys are promising for the MIR range photodetection. It should be noted that the GeSn alloy growth with the Sn content between 0 and 12.5 % was demonstrated by MBE, as mentioned in Chapter 2.1.2. Theoretically, defect-free GeSn photodetectors were expected to be comparable with commercial III-V photodetectors in terms of responsivity and detectivity, as shown in Figure 22(a) and (b). The increase in Sn content extends the cut-off wavelength. However, appropriate Sn content should be considered because dark current increases with Sn content.

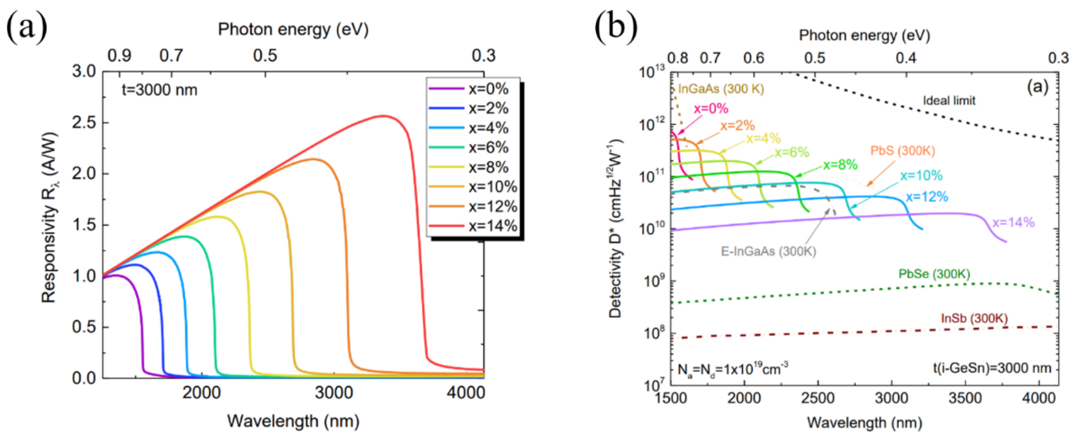

Figure 22. (a) Calculated responsivity and (b) detectivity spectra of GeSn photodetectors with different Sn compositions with a total thickness of 3,600 nm (*i*-GeSn = 3,000 nm) at 300 K in comparison with the commercial photodetectors [68].

In 2011, Shaojian Su *et al.* reported GeSn *p*-*i*-*n* photodetectors with 3% Sn content on Si substrate grown via MBE [69]. The cut-off wavelength was extended to 1,800 nm. Since then, GeSn photodetectors have been widely investigated. GeSn photodetectors with high Sn content increased the cut-off wavelength experimentally [70]. The main interest of 2,000 nm photodetection has been achieved with the Sn content of ~6% [71]. In investigating GeSn photodetectors, critical obstacles for GeSn photodetectors were raised up. One of them is the dark leakage current [72]. The higher the Sn content in GeSn, the higher defects. Many defects in GeSn lead to a high dark current for GeSn photodetectors. It has been reported that surface current was significantly high for GeSn photodetectors with small device sizes. Various approaches have been proposed to suppress surface current. First, Si surface passivation was introduced to reduce surface leakage current [74]. Figure 23(a) represents the cross-sectional view of a GeSn photodetector passivated by a Si passivation layer. The extracted surface leakage current from Figure 23(b) was reduced by ~100× in comparison with the one without Si passivation. Second, dark current was suppressed by adding an Al_2O_3 interlayer between metal and Ge for GeSn metal-semiconductor-metal (MSM) photodetectors [75]. Third, low leakage current was reported with GeSn/Ge multi-quantum well (MQW) structures [76].

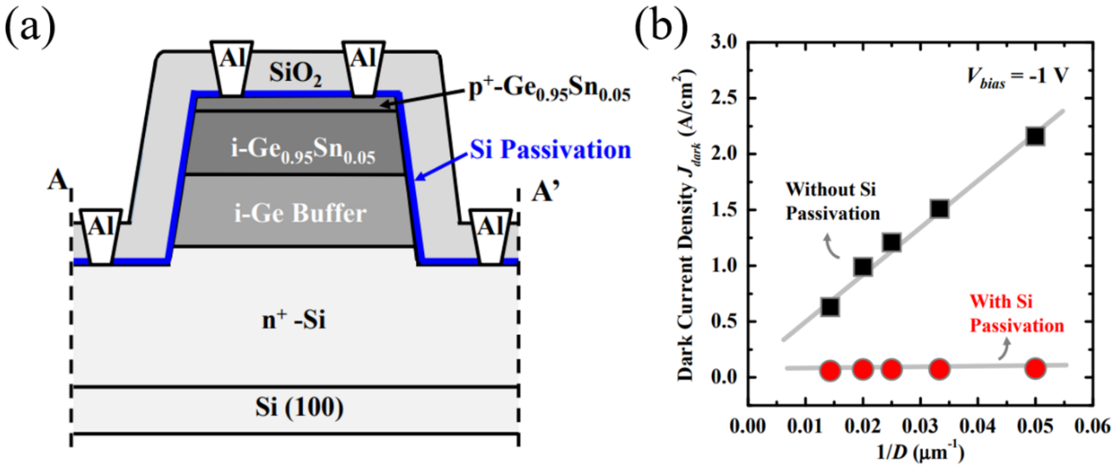

Figure 23. (a) Cross-sectional schematic of a GeSn photodetector (b) dark current density versus 1/diameter (*D*) characteristics of a GeSn p-i-n photodetector [74].

Weak optical responsivity for GeSn photodetectors has been improved by employing on-insulator platforms, photon-trapping hole structures, etc. GeSn photodetectors on insulator platforms, e.g., SOI or GOI platforms, were reported [53]. A vertical resonance cavity induced by an insulator platform enhances optical absorption. Figure 24(a) displays reflectivity and responsivity spectra for a GeSn resonant cavity-enhanced photodetector (RCEPD). It should be noted that responsivity was improved at ~1,700 nm, signifying that an insulator platform is promising for long-wavelength photodetection. Figure 24 (b) displays responsivity improvement for GeSn photodetectors on insulator platforms. Compared with the photodetectors on Si substrate, the responsivity was enhanced by 1.65× and 1.98× at 1,550 and 2,000 nm, respectively.

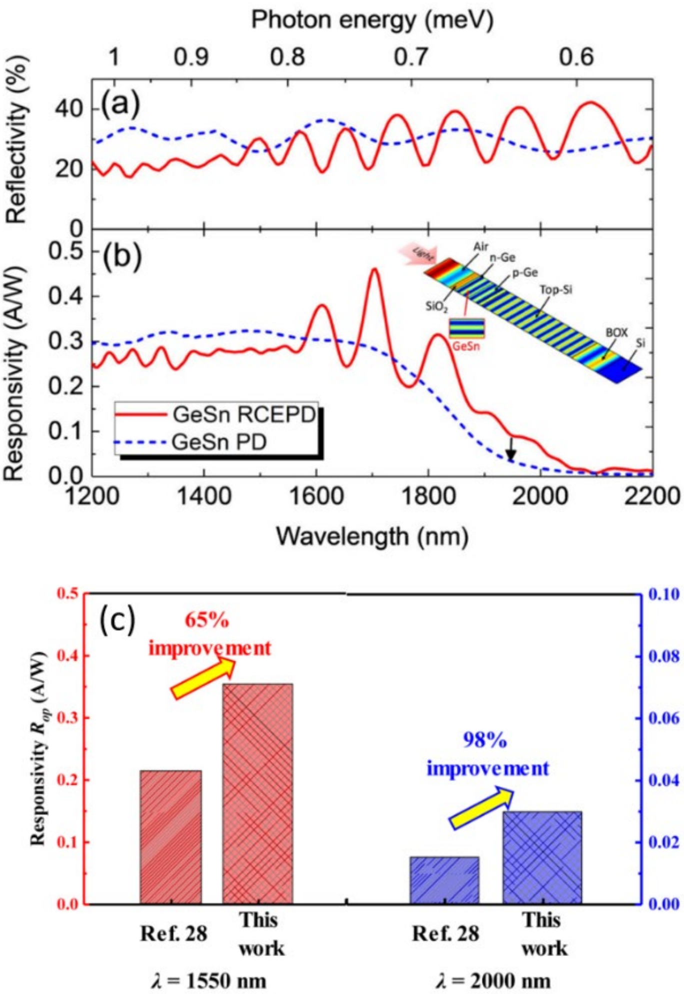

Figure 24. (a) Reflectivity and (b) responsivity spectra of GeSn photodetector on SOI platform and the reference GeSn photodetectors [77]. (c) Responsivity for GeSn/Ge MQW photodetector on Si substrate and on GOI substrate at 1,550 and 2,000 nm wavelength [53].

A micro-photon trapping hole array was proposed to improve optical absorption [78]. Figure 25(a) displays the 3D schematic image of a hole array GeSn photodetector. As shown in Figure 25(b), photocurrent is improved by ~4×. A hole array is adopted to scatter incidence light so that the optical field is confined in vertical and lateral directions. It should be noted that the improved responsivity window can be tunable by changing the hole diameter and period.

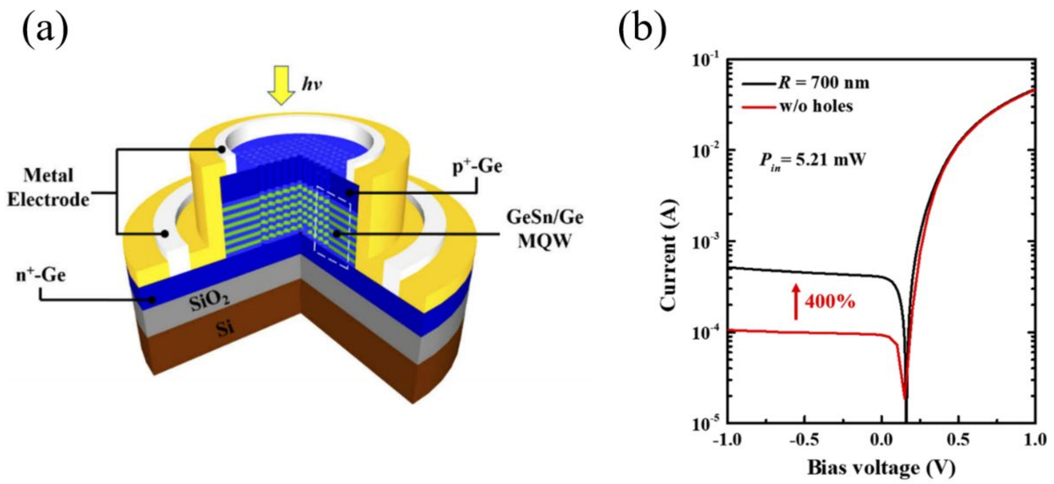

Figure 25. (a) 3D schematic of the hole array GeSn/Ge MQW photodetector on the GOI platform. (b) I-V characteristics of the GeSn/Ge MQW photodetectors with and without photon-trapping hole structure at 2,000 nm wavelength [78].

2.4 Summary

Epitaxial Ge growth has been promising since the early 1980s due to its excellent optical and electrical properties. Ge crystallinity after growth is mainly associated with TDD, which results from a 4.2% large lattice mismatch and a difference in thermal expansion coefficient between Ge and Si. Up to date, the three-step growth has been adopted for epi-Ge growth to mitigate defects/dislocations. Epitaxial GeSn growth was developed in the early 2000s. The main obstacles for GeSn growth are i) low-temperature growth conditions and ii) large lattice mismatch between GeSn/Si.

Diverse optical components in Ge/GeSn material systems on-insulator platforms were investigated. Thanks to its high optical absorption and electrical isolation, integrative devices on insulator platforms, e.g., a waveguide, a modulator, a photodetector, a laser, and MOS, display excellent performances. Many defects/dislocations are formed near GeSn/Si and Ge/Si interfaces, degrading optical and electrical properties. Thus, trap-related carrier dynamics near interfaces should be mitigated by transferring GeSn and Ge directly to an insulator. Among diverse approaches, DWB and layer transfer techniques are promising to satisfy mass production and low-temperature processes.

Photodetectors benefit from the insulator platforms. A thick active layer was grown to increase an optical penetration path. However, such a thick layer causes a trade-off between bandwidth and optical responsivity. On-insulator platforms can vanish the trade-off. The insulator platform causes vertical resonant cavity modes so that the optical field is confined in Ge/GeSn active regions. Hence, despite a thin Ge/GeSn layer, responsivity is considerable and 3dB bandwidth can be improved. Recently, lateral resonant cavity modes were observed for photodetectors with micro- and nano-hole array structures. The photon-trapping hole structures trap the light, leading to improved optical absorption. Besides, dual-absorption structures and an avalanche photodiode (APD) also improved the responsivity.

The following Chapters will describe high-performance Ge/GeSn photodetectors. Significant dislocations in Ge are reduced to mitigate trap-related carrier dynamics in Chapter 3. In addition, the optical responsivity for a photodetector is improved with a gourd-shaped hole array structure in Chapter 4. As a result, the specific detectivity for Ge photodetectors is comparable to commercial bulk Ge and III-V photodetectors. GeSn photoconductors will be addressed and investigated trap-related carrier dynamics in Chapter 5. It will be revealed that a GeSn/Ge interface is the main contributor to degrade photoexcited carrier dynamics. In Chapter 6, GeSnOI platforms will be introduced to remove a GeSn/Ge interface, which potentially leads to low dark current and improved optical absorption.

Chapter 3. Ge-on-insulator *p-i-n* Photodetectors with Sub-mA/cm^2 Dark Current Density

In Chapter 3, vertical *p-i-n* GOI photodiodes with ultra-low dark current density will be addressed. Chapter 3.1 describes one of the main issues for Ge photodetectors. The demonstration of the GOI platform and the fabrication of Ge photodiodes are introduced in Chapter 3.2 and 3.3, respectively. The characterization of the GOI photodiodes is performed in Chapter 3.4. Chapter 3.5 summarizes the results in Chapter 3.

3.1 A Drawback of Ge Photodetectors – High Dark Current Density

Ge is an emerging Group IV element in Si-based electronic and photonics, thanks to its excellent optical and electrical properties. Carrier mobility in Ge is higher than the one in Si, which is desirable in optoelectronics and spintronic devices. As described in Chapter 2, Ge optical properties are attractive to NIR range photodetection.

Epi-Ge photodetectors have shown a huge dark leakage current. Ge *p-i-n* photodiodes have been demonstrated to have dark current densities of ~10 mA/cm^2. In contrast, the dark current density of 56 μA/cm^2 was reported for bulk Ge photodiodes [79]. This drawback of epi-Ge photodetectors degrades performances in terms of detectivity and noise equivalent power (NEP). It has been reported that high dark current for Ge photodetectors originates from plenty of defects, e.g., misfit dislocations and threading dislocations, generated during epitaxial Ge growth on a Si substrate [80]. Specifically, the high leakage currents for Ge photodetectors are attributed to i) defects in Ge, ii) defects at a Ge/Si interface, and iii) surface defects. Numerous defects serve as trap centers, named Shockley-Read-Hall (SRH) centers, degrading optical and electrical properties. SRH leakage, where minority carriers are generated through trap centers, was one of the primary leakage current mechanisms for Ge photodetectors [81]. In addition, a trap-assisted tunneling (TAT) leakage process, where the carriers tunneled through the trap centers, enhances dark current [84].

The trap-related leakage processes, i.e., SRH and TAT leakage processes, are associated with TDD in epi-Ge [81]. A reduction in TDD from 1.6×10^{10} to 4.2×10^{8} cm^{-2} resulted in ~10× dark current reduction for Ge $p^{+}n$ junctions [80]. A decrease in TDD from 3×10^{8} to 5×10^{7} cm^{-2} caused ~45× dark current reduction for Ge *p-i-n* photodiodes [83]. A reduction in TDD from ~4×10^{8} and ~2×10^{10} to ~1-2 $\times 10^{7}$ cm^{-2} led to ~5× and ~25× dark current reduction, respectively [86].

As threading and misfit dislocations are reduced, surface leakage current becomes a dominant leakage current component. The contribution of surface current to dark current is severe, especially where TDD reaches below 10^{8} cm^{-2} [87]. Therefore, advanced surface passivation is required to suppress dark current for Ge photodetectors with low TDD [92]. Among them, the formation of a germanium-oxide (GeO_x) layer is promising, benefiting from a high-*k* dielectric property and low surface defect density. The high quality of the GeO_x surface layer has been demonstrated via thermal annealing, O_2

plasma, and O_3 oxidation. Among them, O_3 oxidation benefits from a low-temperature process and excellent sidewall passivation.

Ge/Si or Ge/Si-on-insulator platforms have been introduced to demonstrate Ge photodetectors [94]. However, plenty of defects near the Ge/Si interface are generated during Ge growth. Thus, it is favorable to remove interface layers. DWB and layer transfer techniques are treatments that isolate an epi-Ge layer from Si substrate. The methods enable the removal of Ge/Si interface layers, which potentially reduce dark current for photodetectors. An annealing process in O_2 ambient on the GOI platform has recently been introduced to suppress TDD down to ~10^6 cm^{-2}. Thus, such a GOI platform with low TDD is promising for the demonstration of high-performance optical devices [96].

In Chapter 3, two approaches are introduced to reduce dark leakage current for Ge photodiodes. First, a TDD reduction via O_2 anneal is conducted to mitigate bulk leakage current. Second, GeO_x surface passivation via O_3 oxidation is implemented to suppress surface leakage current. Two different TDDs, i.e., the order of 10^6 cm^{-2} (low TDD) and the order of 10^8 cm^{-2} (high TDD), are compared and analyzed to figure out their dependence on Ge photodetectors. The GeO_x surface passivation method is compared with the SiO_2 surface passivation to tell the benefits of GeO_x passivation. Chapter 3 aims to investigate characterizations of Ge photodiodes with their dependence on TDD and surface conditions.

3.2 Demonstration of Ge-on-insulator Platforms

The sequence of fabrication flows for the GOI platform will be described. In this section, DWB and layer transfer techniques are addressed to demonstrate the GOI platform. Chapter 3.2.1 contains the detail in epi-Ge layer transfer to insulator platform. Subsequently, characterization of the platform is conducted in Chapter 3.2.2.

3.2.1 Demonstration of O_2-annealed Ge-on-insulator

An epitaxial Ge layer is grown on an 8-inch Si donor wafer via a three-step Ge growth method. Each step consists of (i) low-temperature growth at ~400 °C; (ii) the increases in temperature from 673 to 873 K; (iii) high-temperature growth at 873 K. A Si handle wafer was brought as the transfer wafer separately. SiO_2 and Si_3N_4 layers are deposited via plasma-enhanced chemical vapor deposition (PECVD) on both donor and handle wafers. Subsequently, O_2 plasma exposure is conducted to both wafers, and they are rinsed with deionized (DI) water to make surfaces clean and to form a hydroxyl (OH) group on surfaces for bonding [96]. After that, the donor wafer is flipped over on the handle wafer, and the pair wafers are bonded at 300 °C in an atmospheric N_2 ambient. The tetramethyl-ammonium hydroxide (TMAH) is implemented to remove the bulk Si donor layer on top after the bonding process. During the TMAH solution etching process, a protection layer is covered on the Si handle wafer to etch the Si donor layer selectively. The protection layer can be removed in O_2 plasma after confirming the Si donor layer is removed. It should be noted that the Ge/Si interface is removed away after the DWB and layer transfer processes.

After that, O_2 anneal at 650°C is conducted to reduce TDD. Si-Ge intermixed layers are oxidized during the annealing process. HF solution (49 % HF:H_2O = 1:20, by volume) is implemented to eliminate oxidized Si/Ge layers [96]. After that, CMP is performed to flatten annealed GOI surface. The schematic fabrication flow for GOI platforms is summarized in Figure 26(a)-(d).

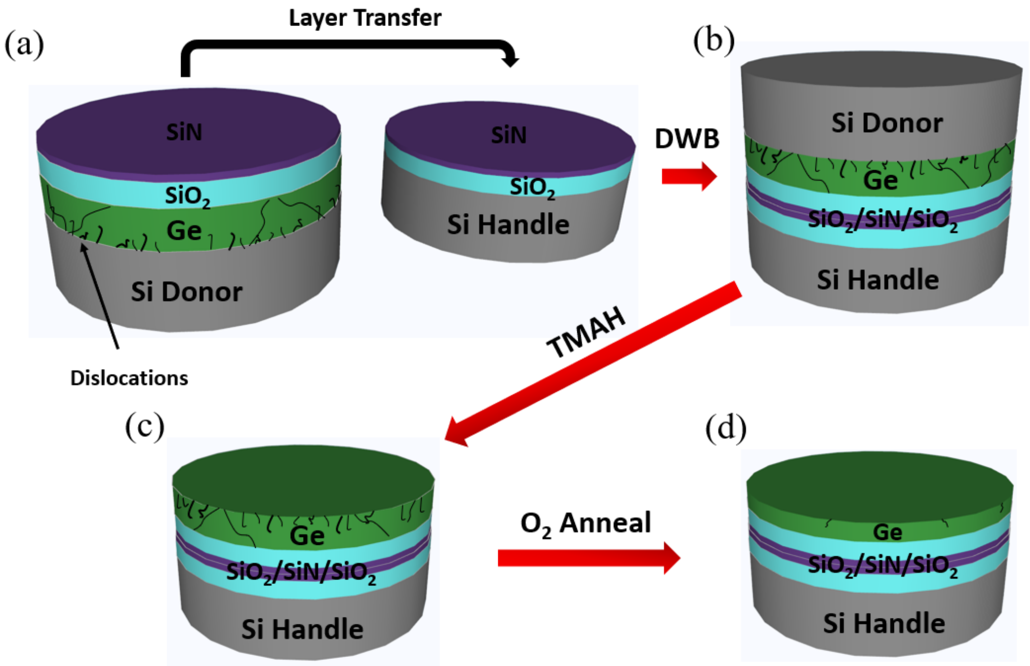

Figure 26. Fabrication flows of DWB and layer transfer techniques. (a) Preparation of donor and handle wafers for layer transfer. (b) Bonded wafer pair in the DWB process, (c) Formation of the GOI platform by etching the Si donor layer by TMAH solution. (d) O_2-annealed GOI substrate. The black lines in epi-Ge layers represent misfit and threading dislocations.

3.2.2 Characterization of O_2-annealed Ge-on-insulator

A photograph of annealed GOI wafer in an 8-inch scale is illustrated in Figure 27(a), signifying a GOI wafer can be realized with a mirror-like surface. AFM is performed to analyze surface characterization in Figure 27(b). Surface scanning is conducted in the size of 5 μm × 5 μm. The root mean square (RMS) of surface roughness for GOI was obtained to be 0.2 nm, comparable to RMS of the surface roughness for an epi-Ge before bonding.

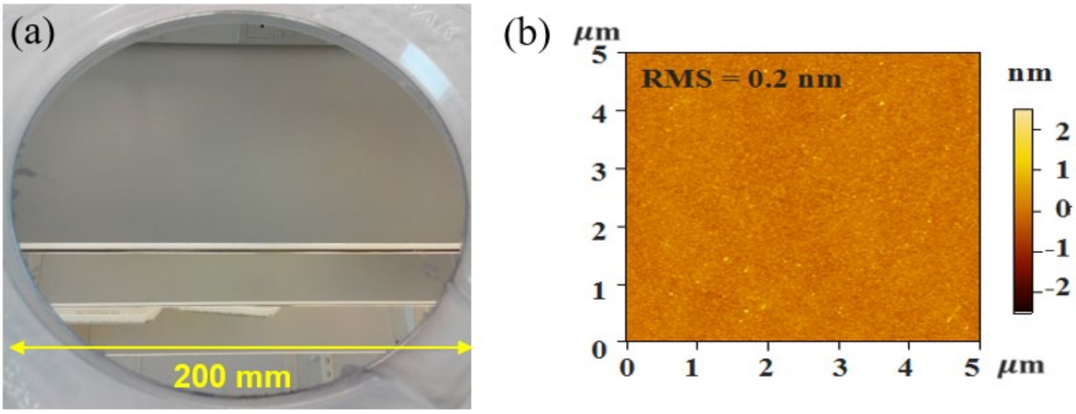

Figure 27. (a) Photograph of the O_2 annealed-GOI substrate in an 8-inch scale [99]. (b) AFM surface scan image for O_2 annealed-GOI substrate in the area of 5 μm × 5 μm.

High-resolution X-ray Diffractometry (HRXRD) characterization of a 2theta-omega (2θ-ω) scan is performed in the (004) orientation for GOI with and without O_2 anneal in Figure 28. The scanning step was defined to be 0.01°. The HRXRD curve of Ge bulk is included as a reference. A bulk Ge peak appears at 65.99°. GOIs show two peaks corresponding to Ge and Si. A peak for GOI with O_2 anneal is close to the Ge bulk peak. In addition, a Ge curve for GOI with O_2 anneal is more symmetric than the one for GOI without O_2 anneal. This is because of strain relaxation during O_2 anneal. The estimated strain for GOIs with and without O_2 anneal is 0.16 and 0.25%, respectively.

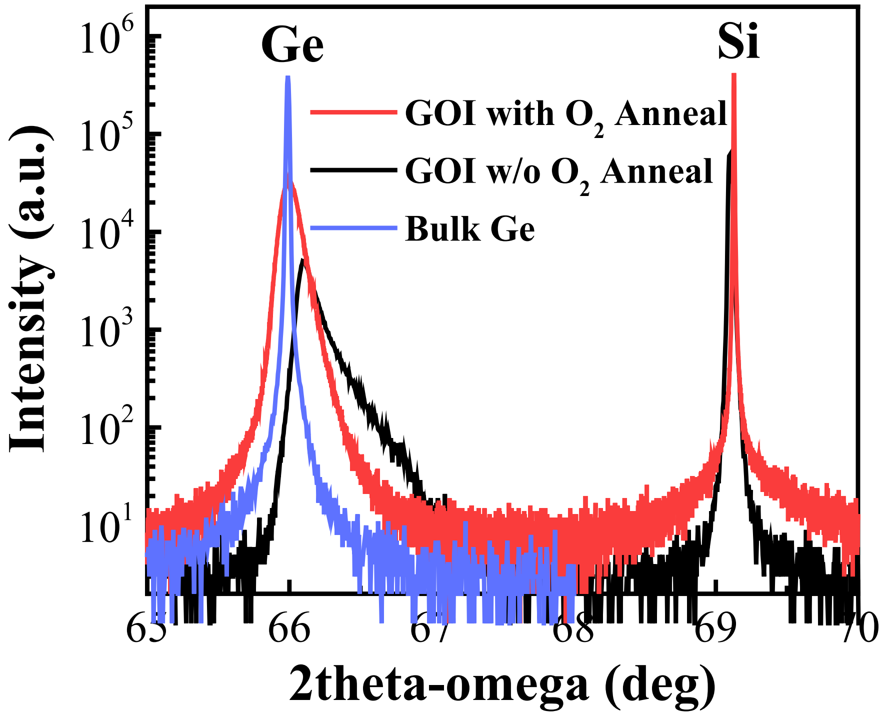

Figure 28. HRXRD curves of *2θ-ω* for GOIs with and without O_2 anneal and Ge bulk as reference [99].

The cross-sectional views of TEM images of GOI structures before and after O_2 anneal are shown in Figure 29(a) and (b), respectively. Dislocations along a Ge/Si interface become smoother after the annealing, resulting from a dislocation reduction. According to TEM analysis, TDD for samples after and before the O_2 anneal is estimated to be 6.4×10^7 and 7.7×10^8 cm^{-2}, respectively.

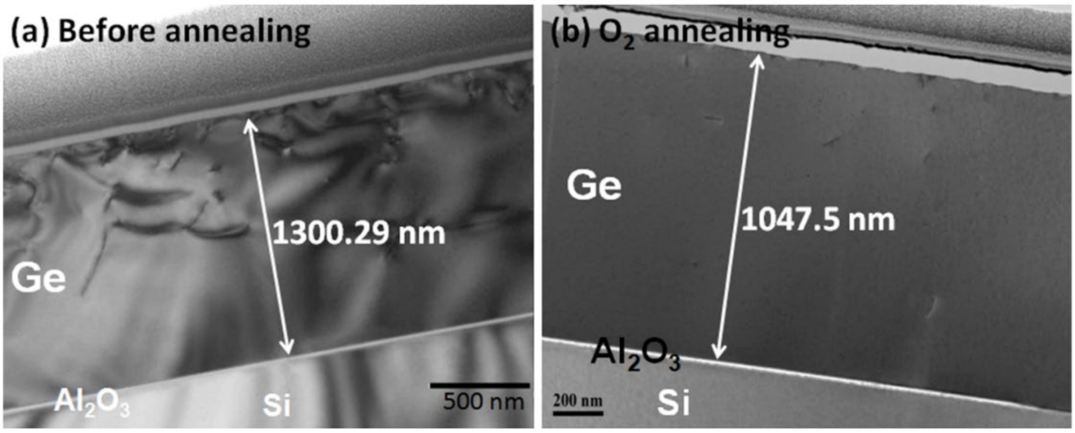

Figure 29. Cross-sectional images for GOIs (a) before and (b) after O_2 anneal via the TEM analysis [96].

In order to verify TDD value precisely, low magnification analysis is required. SEM analysis can be used to characterize TDs based on a top view image. An Iodine solution was used for 1s to make TDs visible. Since the solution etches dislocations faster, etch pits become observable. For GOI after O_2 anneal, the etch pits are barely visible in Figure 30(a). In contrast, many etch pits in Figure 30(b) are present across an entire sample. Etch pit density (EPD) in epi-Ge before and after the annealing is estimated to be ~5.2 $\times$ 10^8 cm^{-2} and ~2.5 $\times$ 10^6 cm^{-7}, respectively. It should be noted that EPD for O_2 annealed GOI is reduced by ~100×.

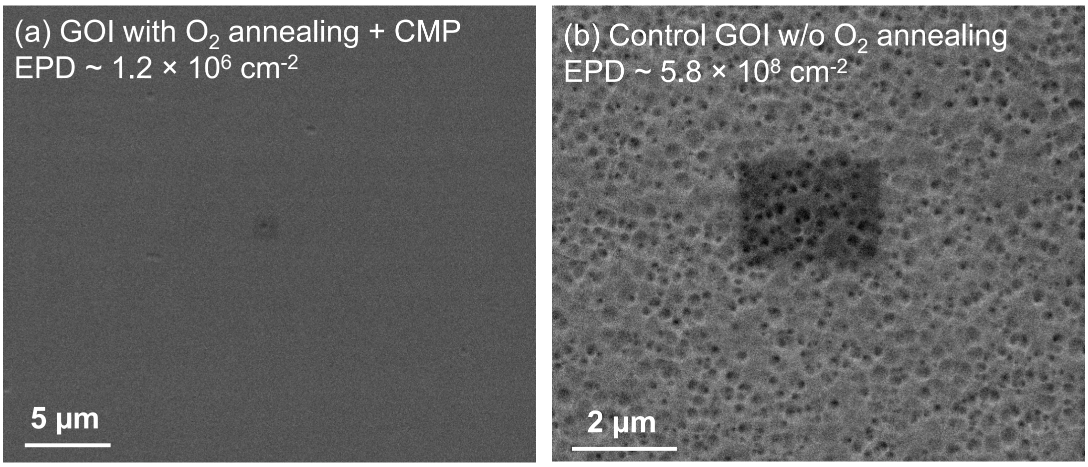

Figure 30. The planar views for GOI substrates (a) before and (b) after O_2 anneal and CMP processes via the SEM analysis [96].

3.3 Demonstration of Ge Photodiodes

The vertical *p-i-n* Ge photodiodes are fabricated using O_2-annealed GOI substrates. Chapter 3.1.1 shows the demonstration and characterization of vertical *p-i-n* GOI structures. Then, vertical *p-i-n* GOI substrates are utilized to demonstrate vertical *p-i-n* photodiodes on a GOI platform in Chapter 3.3.2. Chapter 3.3.3 describes the formation of a GeO_x layer for advanced surface passivation.

3.3.1 Vertical p-i-n GOI Structure

Boron (B) is selected for *p*-type ion implantation on the epi-Ge on Si donor wafer before the DWB process. A *p*-doped layer is formed near insulator substrates after the bonding process. Then, *n*-type ion implantation was performed with Arsenic (As) at a 7×10^4 cm^{-2} dose and the 40 keV ion beam energy. An *n*-doped layer is formed on a top GOI structure [100]. As a result, a vertical *p-i-n* Ge structure can be formed.

Secondary ion mass spectroscopy (SIMS) analysis and sheet resistance profile (SRP) analysis are conducted to characterize the doping properties of vertical *p-i-n* GOI structures. Figure 31(a) shows the As and B doping profiles via the SIMS analysis. p^+- and n^+-doped layers are observed in shallow doping depth below a few tens of nm using both As and B dopants. Heavily doped regions benefit from efficient ohmic contact and the suppression in diffusion-related dark leakage current. Figure 31(b) represents the electrically activated *n*- and *p*-type doping concentration via the SRP analysis. The doping concentrations for As and B are reduced in comparison with the ones in Figure 31(a). SIMS analysis is the tool to count the total number of dopants formed in either crystalline or point defect or etc. In contrast, SRP analysis provides the doping concentration contributed to the electrical properties.

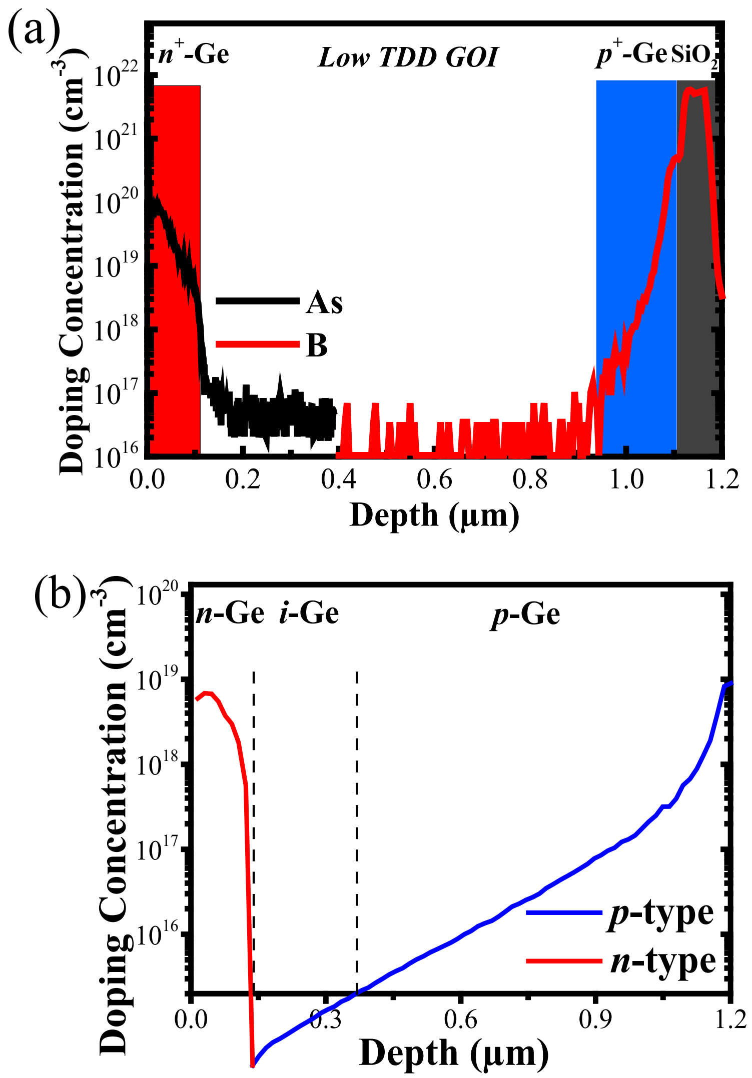

Figure 31. (a) As and B doping profiles of the vertical *p-i-n* GOI structure via the SIMS analysis. (b) *n*- and *p*-type doping profiles of the vertical *p-i-n* GOI structure via the SRP analysis.

3.3.2 Fabrication of GOI Photodiodes

The vertical *p-i-n* GOI structures are used to fabricate vertical *p-i-n* photodiodes. The *n*-mesa region was covered by AZ 5214 photoresist via the photolithography process. Chlorine (Cl_2)-based reactive ion etching (RIE) was implemented to expose p^+-type Ge, remaining the diameters of 60, 80, 150, 250 μm of n^+-type Ge area. The 2nd RIE process was conducted to isolate the p^+-type regions between each photodiode. A buffered oxide etch (BOE) process was then implemented for the removal of a native oxide on a Ge surface. After that, a 200nm SiO_2 was deposited by PECVD for the surface passivation. Subsequently, the surface passivation was conducted. GeO_x surface passivation was performed before the SiO_2 deposition. The detail in the GeO_x passivation process and the characterization can be found in Chapter 3.3.3. Trifluoromethane (CHF_3)-based RIE process and BOE process were carried out to expose ring-shaped tranches on the *n* and *p*-Ge areas. Titanium (Ti)/titanium nitride (TiN)/aluminum (Al) stack metal deposition was performed via the sputtering machine, followed by a lift-off process [100]. Rapid thermal annealing was conducted at 400 °C to improve the ohmic contacts [101]. The schematic 3D cross-sectional view is shown in Figure 32(a), with the key fabrication steps in Figure 32(b). It should be noted that the Al_2O_3/GeO_x layers are formed between SiO_2 and *i*-Ge.

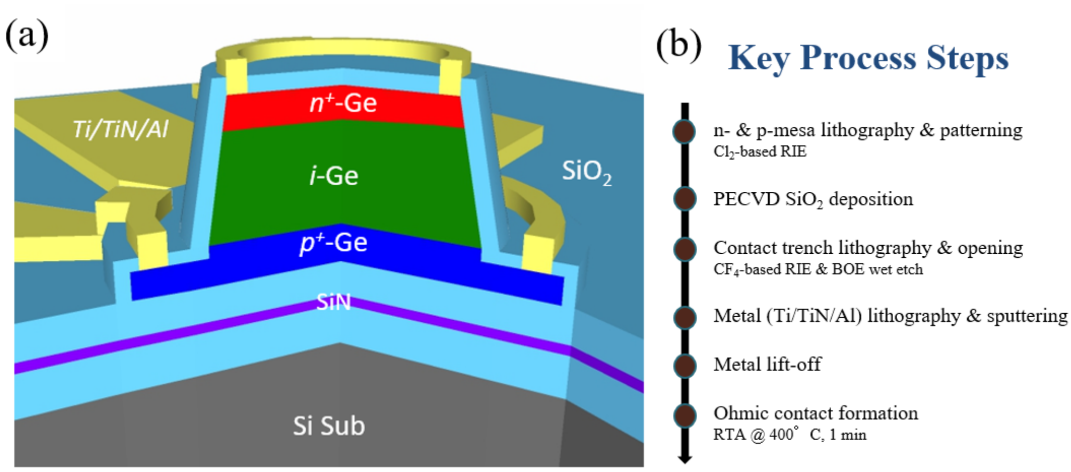

Figure 32. (a) The 3D schematic image for the vertical *p-i-n* photodiode on the O_2-annealed GOI structure. (b) Key fabrication steps for the demonstration of vertical *p-i-n* photodiodes.

The top view of microscopy images is shown in Figure 33(a)-(d) for the completed GOI vertical *p-i-n* photodetectors with diameters of 60, 80, 150, and 250 μm, respectively. The numbers located on the right upper side represent the diameter of the n^+-type area, excluding the metal area. The plan view of the SEM image for the GOI photodiode is shown in Figure 33(e). The right and left electrodes are linked with the *p*-type region, while the central electrode is connected with the *n*-type region. Focused ion beam (FIB) is performed for the cross-sectional view for the photodiode in Figure 33(f).

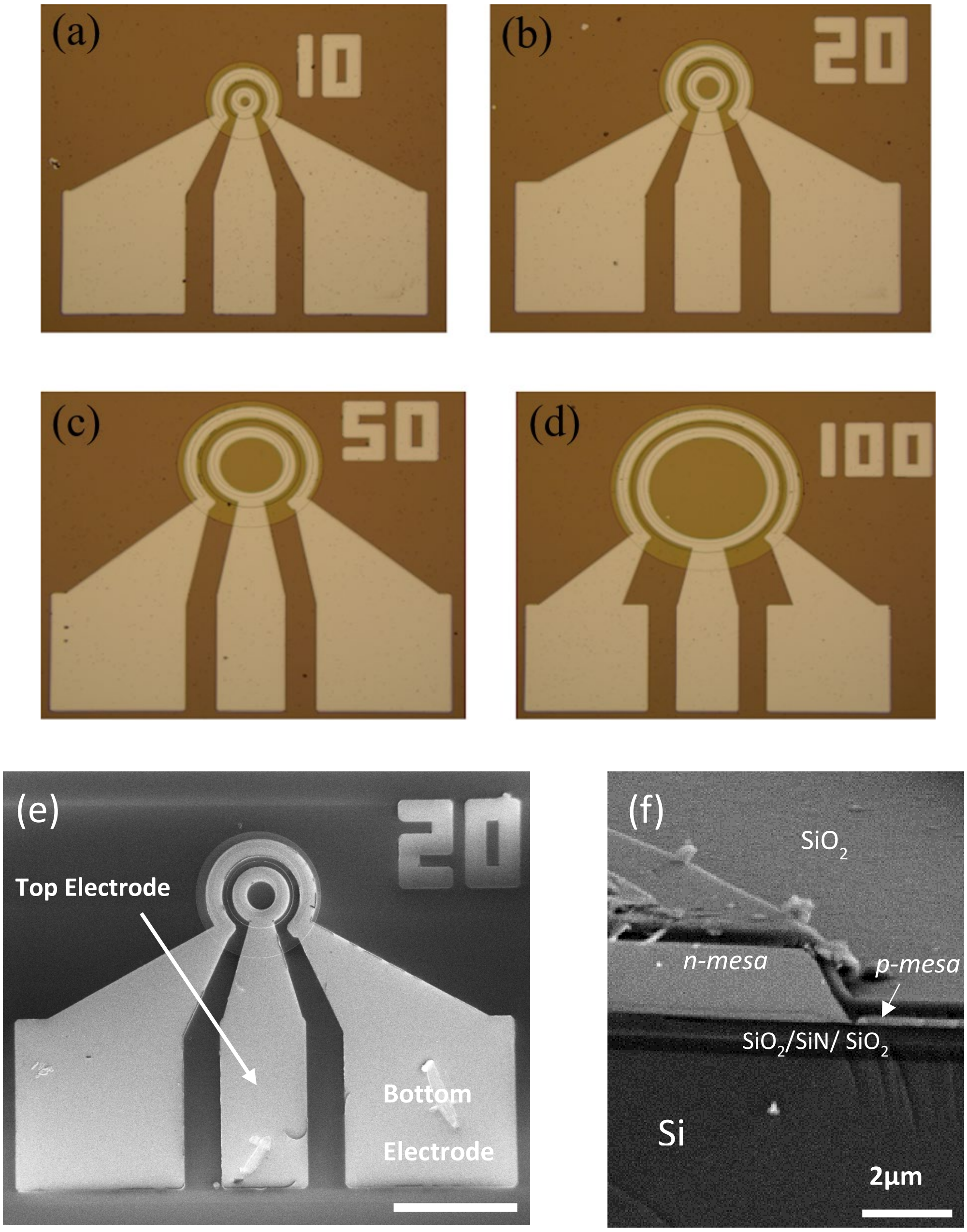

Figure 33. Planar microscopy images of vertical *p-i-n* photodiodes with diameters of (a) 60, (b) 80, (c) 150, and (d) 250 µm. The scale bar is 150 µm. (e) The planar view of the SEM image for the photodiode. (f) The cross-sectional view of the FIB image for the GOI photodiode [100].

3.3.3 O_3 Oxidation for GeOx Surface Passivation

The GeO_x surface passivation process contains the Al_2O_3 layer deposition and O_3 oxidation. Since the GeO_x layer is readily soluble in air, an additional protection layer, i.e., Al_2O_3, is required. Once the BOE process removes the native oxide on the sidewall, the samples are subjected to the 1 nm Al_2O_3 deposition on entire samples via atomic layer deposition (ALD) technique at 250°C. After that, O_3 oxidation is conducted using a UVO cleaner for 20 mins at 300 K. During the oxidation, Al_2O_3/GeO_x is formed on the surface/sidewall of the entire mesa area.

The influence of the GeO_x surface passivation process was studied by X-ray photoelectron spectroscopy (XPS). The Ge 3*d* and Al 2*p* XPS spectra are present in Figure 34(a) for GOIs with and without the O_3 oxidation. The binding energy of ~74 eV is related to Al_2O_3 thin layer, while the bonding energy of ~30 and ~32 eV represents Ge and GeO_x, respectively. The peak at ~32 eV is observed after the O_3 oxidation, meaning that Ge oxides are formed. Binding energy of Ge^{1+}, Ge^{2+}, Ge^{3+}, and Ge^{4+} increases by 0.80, 1.80, 2.75, and 3.40 eV from the Ge^0 binding energy, respectively [103]. Each Ge oxidation state spectra are extracted by the Gaussian-Lorentzian fitting. The extracted chemical components were indicated in Figure 34(b). The Ge^{3+} core level is significant in comparison with other Ge oxidation states. The GeO_x thickness is highly related to the areal intensity of Ge^{3+} [104]. The estimated GeO_x thickness is obtained to be 1.1 nm.

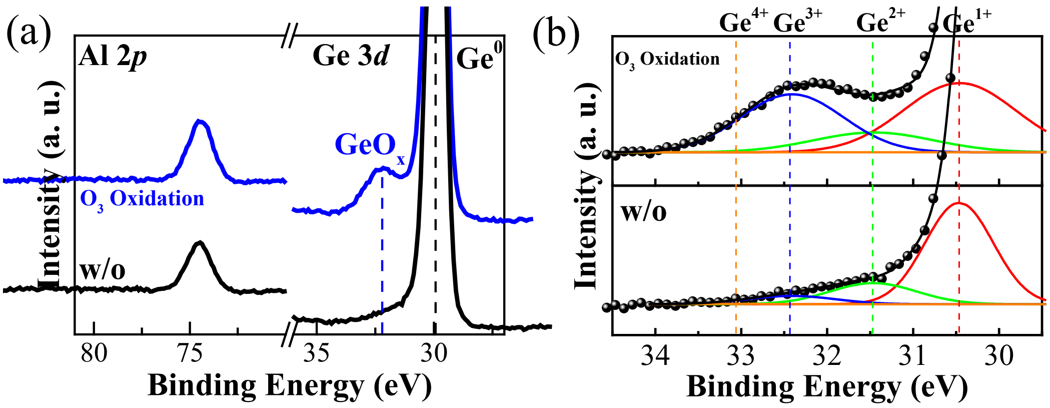

Figure 34. (a) The XPS spectra of Al_2O_3/GeO_x layers before and after the O_3 oxidation. (b) The XPS spectra of GeO_x with the extracted Ge oxidation state spectra.

3.4 Characterizations of Ge Photodetectors

The demonstrated photodiodes are characterized in this section. “High TDD” and “Low TDD” will represent the GOI platforms with and without the O_2 anneal process, respectively, to verify the TDD-dependent performance of photodetectors. The GOI photodiodes with and without the GeO_x passivation process are characterized, representing “SiO_2 passivation” and “GeO_x passivation” in the section, respectively. Chapter 3.4.1 to 3.4.3 describe the dark leakage current characterization. Chapter 3.4.4 and 3.4.5 address the photo-response characterization of the photodiodes.

3.4.1 Dark Current Density Analysis

Dark current density-voltage (J_{dark}-V) characteristics of Ge photodetectors with high and low TDD are illustrated in Figure 35(a). J_{dark} for the photodetectors with varying mesa diameters from 60 to 250 μm is indicated in Figure 35(a). J_{dark} for high TDD photodetectors was ~59.5 mA/cm^2 at -1 V, which is consistent with varying mesa sizes. J_{dark} for low TDD photodetectors was, in contrast, was measured to be 1.1 to 4.0 mA/cm^2 as the diameters decrease from 250 to 60 μm. J_{dark} for Ge photodetectors is suppressed by ~54× due to the TDD reduction from 5.2×10^8 to 3.2×10^6 cm^{-2}.

The dark current for a photodetector can be separated into two leakage current components, i.e., a bulk current density (J_{bulk}) and a surface current density (J_{surf}) [106]. J_{surf} is the dark current density that flows on the Ge surface. The unstable bonds, e.g., dangling bonds, creates surface defect states at the surface. The generation or tunneling of minority carriers through the surface defect states leads to J_{surf}. J_{bulk} is the dark current density where minority carriers are generated or tunneled through the depletion regions and defect states [81]. Trap states in defects, e.g., misfit and threading dislocations, are contributed to the generation or tunneling of minority carriers through trap centers, resulting in significant J_{bulk} [107].

J_{dark} can be divided into surface and bulk currents by the following equation [76],

$$J_{dark} = J_{bulk} + J_{surf} \times \frac{4}{D}. \tag{15}$$

The linear fitting of J_{dark} as a function of 1/*D* can extract J_{surf} and J_{bulk}, as shown in Figure 35(b). estimated J_{bulk} is 59.9 and 0.2 mA/cm^2 for high and low TDD photodetectors, respectively. It should be noted that J_{bulk} is suppressed by ~300×. The following two factors contribute to low J_{bulk}, i) the TDD reduction and ii) The reduced depletion width during the O_2 anneal and HF etching processes. Thin depletion width provides less channel to increase the dark current via the trap states. Shallow Ge *pn* junctions provided lower J_{dark} than *p-i-n* junctions due to the shallow depletion width [86].

The inset in Figure 35(b) shows a contribution of bulk current (I_{bulk}) and surface current (I_{surf}) for low TDD photodetectors as a function of mesa diameters. The I_{bulk} contribution was obtained to be 4% for the photodetector with a 60 μm diameter while I_{surf} contribution is 96%. The I_{surf} contribution is reduced to 85% for the photodetector with a 250 μm diameter. The contribution for photodetectors with TDD of ~10^8 cm^{-2} is not shown here due to the dominant I_{dark} of ~100% in the mesa area from 60 to 250 μm. Previously, photodetectors with the TDD of ~10^7 cm^{-2} were governed by I_{surf} [83]. As TDD is reduced down to the order of 10^6 cm^{-2}, I_{surf} becomes the primary leakage component. The I_{surf} contribution is expected to increase where the mesa diameter decreases further. This is because the bigger device shows a smaller perimeter to area ratio than that of smaller ones. Therefore, it is necessary to perform advanced surface passivation for low TDD Ge photodetector, especially with a few tens of μm mesa diameters.

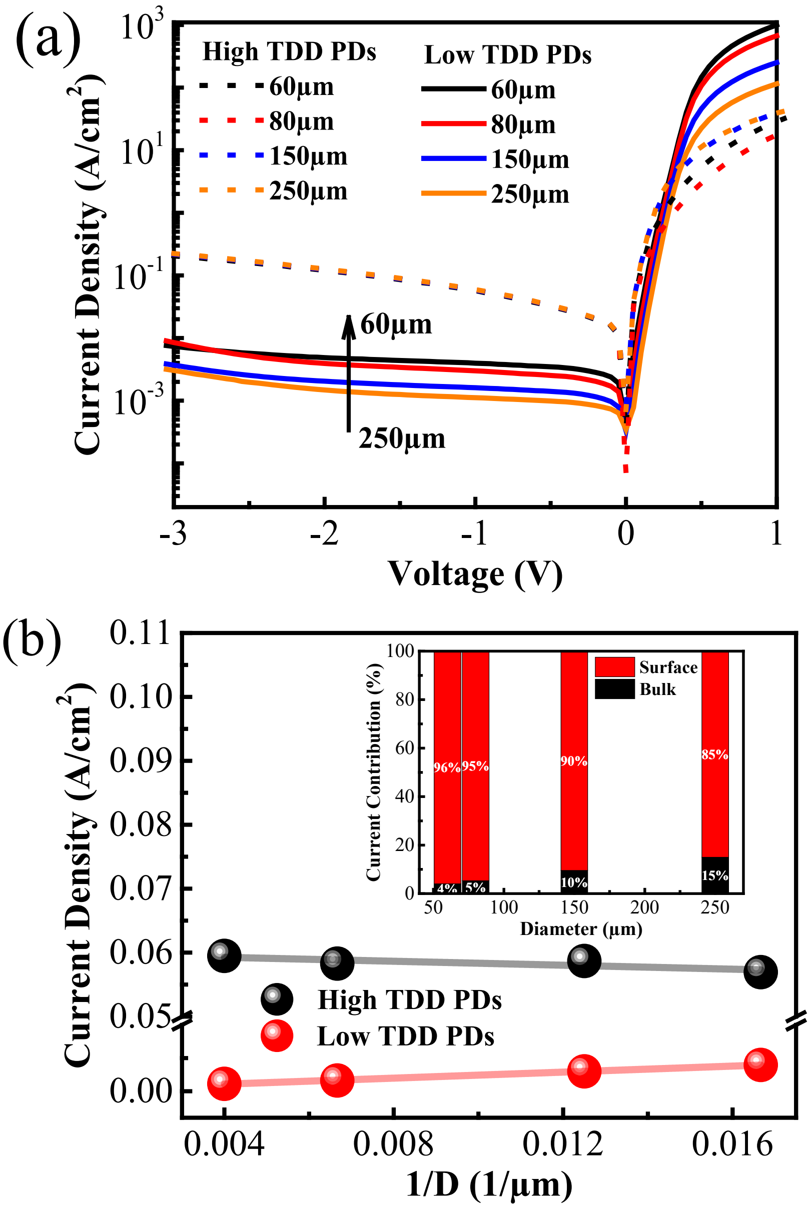

Figure 35. (a) J_{dark}-V characteristics for low and high TDD Ge photodetectors (PDs) with different mesa sizes. (b) J_{dark}-$1/D$ characteristics for low and high TDD Ge PDs at -1 V. Inset in Figure 35(b) shows the current contribution for low TDD Ge photodetectors.

The influence of the GeO_x passivation is investigated to reduce J_{surf} in Figure 36. Figure 36(a) displays J_{dark}–V curves for the photodetectors with GeO_x and with SiO_2 passivations. The photodetector with SiO_2 passivation displays J_{dark} of 4.0 mA/cm^2, suffering from the considerable I_{surf} [66]. J_{dark} for the GeO_x-passivated photodetector with the same mesa size is reduced by

~4×. J_{dark} for the GeO_x-passivated photodetector with the 250 μm diameter was 0.6 mA/cm^2.

Extracted J_{surf} for photodetectors with SiO_2 passivation is 5.7 μA/cm in Figure 35(b). J_{bulk} and J_{sur} for GeO_x-passivated photodetectors are extracted to be 0.5 mA/cm^2 and 0.6 μA/cm, respectively, as shown in Figure 36(b). For the Al_2O_3 passivation, J_{sur} for photodetectors was ~42.0 μA/cm [108]. J_{sur} for photodetectors with SiO_2 passivation was reduced by 8× compared to Al_2O_3-passivated photodetectors. For the GeOx-passivated photodetectors, J_{sur} is further reduced by 10× compared to SiO_2-passivated photodetectors. The I_{dark} contribution for GeO_x-passivated photodetectors is obtained in the inset in Figure 36(b). The I_{surf} contribution is 54% for the photodetector with a 60 μm diameter. The I_{surf} contribution is reduced to 17% for the photodetector with a 250 μm diameter.

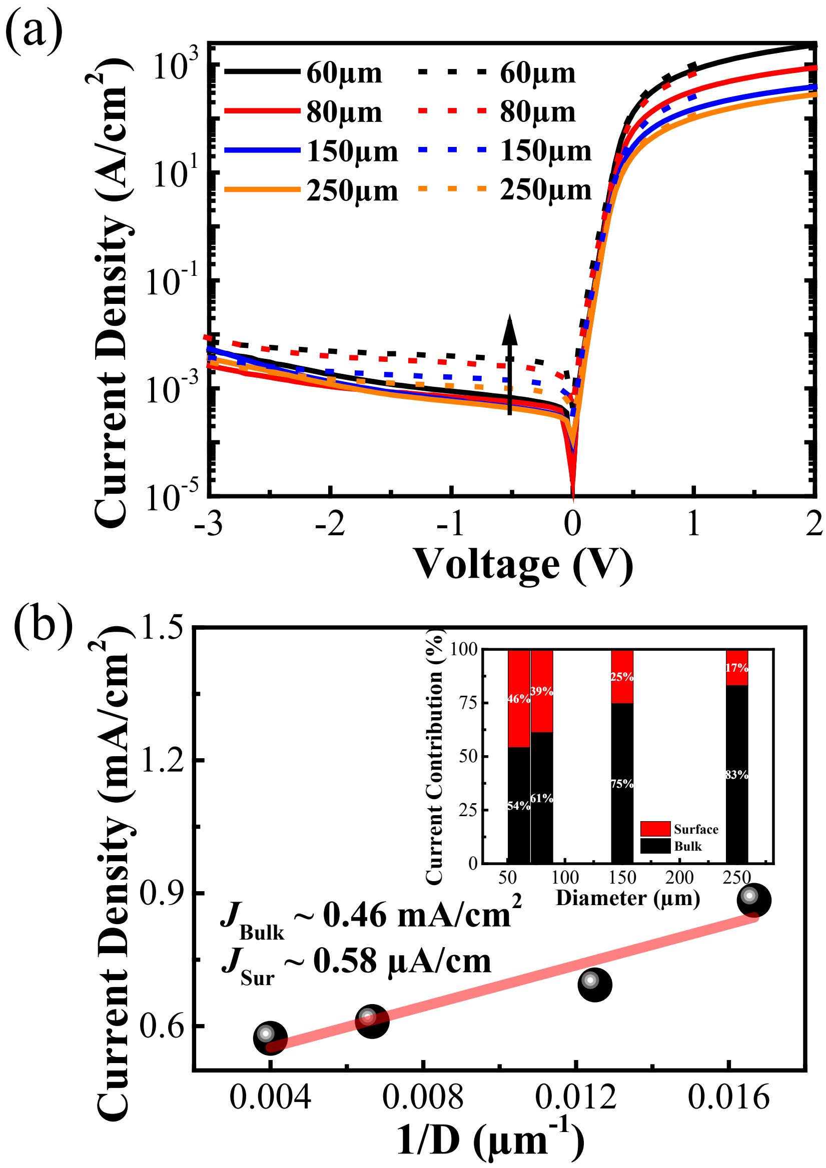

Figure 36. (a) J_{dark}-V characteristic of photodetectors with GeO_x and with SiO_2. The arrows represent the increase in the mesa diameter from 60 to 250 μm. (b) The J_{dark}-$1/D$ characteristic at -1 V. The inset in Figure 36(b) displays the I_{dark} contribution of I_{bulk} and I_{surf}.

3.4.2 Temperature-dependent Dark Current Study

The temperature-dependet dark current study is important to investigate the dark leakage current mechanisms by extracting the activation energy (E_a). The temperature-dependent I_{dark}-V characteristics for the photodetectors with high and low TDD photodetectors with SiO_2 passivation were performed in the temperature range from 293 to 353 K in Figure 37(a). The temperature increases with the dark current for photodetectors. I_{dark} for the low TDD photodetector is suppressed by ~100× in comparison with photodetectors with high TDD in the measured temperature range.

Figure 37(b) shows I_{dark} compared with I_{surf} for the low TDD photodetector with SiO_2 passivation. It should be noted that extracted I_{surf} is almost close to I_{dark}, meaning that I_{surf} is the primary leakage current process. I_{bulk} can be obtained by subtracting I_{dark} by I_{surf}. I_{surf} and I_{bulk} divided by the mesa area give J_{surf} and J_{bulk}, respectively. J_{dark} increases from 4.0 at 293 K to 47.0 mA/cm^2 at 353 K at -1 V. J_{surf} increases from 5.7 at 293 K to 41.3 μA/cm at 353 K. J_{bulk} was 0.2 mA/cm^2 at 293 K and increased 3.6 mA/cm^2 at 353 K. The J_{bulk} variation is severe more than the J_{surf} variation.

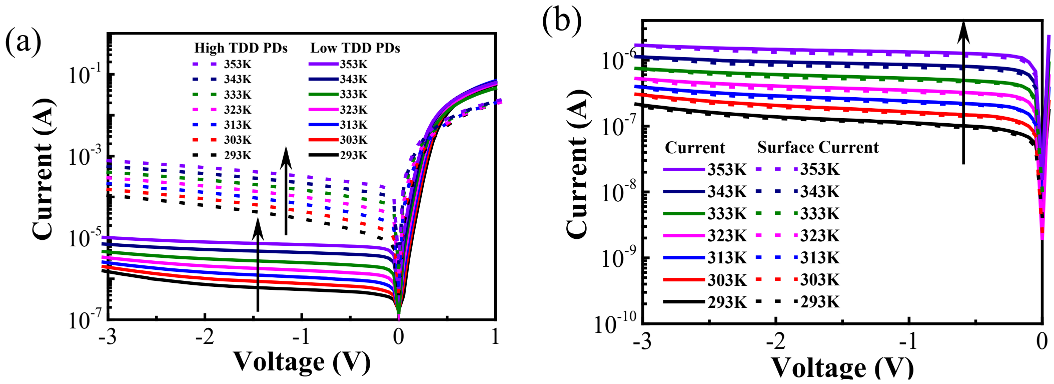

Figure 37. (a) Temperature-dependent I_{dark}-V characteristics for low and high TDD photodetectors (b) Temperature-dependent I_{dark}-V and extracted I_{surf}-V for the low TDD photodetector with a 60 μm diameter. The arrow in Figure 37(a) and (b) represent the temperature increasing from 293 to 353 K.

Since the current variation is different for J_{surf} and J_{bulk}, an interpretation of leakage current mechanisms was performed by the activation energy (E_a) analysis. E_a can be estimated from the Arrhenius plot. Figure 38(a) shows the Arrhenius plot for high and low TDD photodetectors with respect to $1/kT$ when temperature changes from 293 to 353 K, where k is the Boltzmann constant. The line shapes of the low and high TDD photodetectors differ due to the different leakage current mechanisms. E_a can be expressed by the following equation,

$$ln\left(\frac{I_{dark}}{T^{1.5}}\right) = -\frac{E_a}{kT} + ln(B), \tag{16}$$

where T and B are temperature and a constant. Figure 38(b) shows E_a for the high TDD photodetector as a function of the reverse bias voltage. E_a is estimated to be 0.39 eV at -0.1 V in the temperature range from 293 to 353 K. At -3 V, E_a is reduced to 0.21 and 0.29 eV at 298 and 353 K, respectively. Dark leakage current mechanisms for a *p-i-n* photodetector for a photodetector can be categorized into 4 processes as follow: (i) the diffusion leakage process, (ii) the SRH leakage process, (iii) the TAT leakage process, and (iv) band-to-band tunneling (BTBT) leakage process [109]. The diffusion leakage current process provides E_a of 0.66 eV for a Ge photodetector. The SRH leakage current process displays E_a of 0.33 eV for a Ge photodetector. TAT and BTBT leakage processes display E_a of <0.33 eV for a Ge photodetector. The BTBT mechanism can be negligible in this analysis because the electric field is not sufficient to occur the BTBT leakage. The detail will be addressed below. E_a of 0.39 eV in Figure 35(b) is attributed to the dominant SRH leakage process. As voltage increases, E_a is reduced, indicating that the TAT process is improved. E_a varies from 0.21 to 0.29 eV from 293 to 353 K at -3 V, resulting from the temperature-dependent diffusion, SRH leakage, and TAT leakage mechanisms. For the high TDD Ge photodetector, the dark current is mainly contributed by the SRH and TAT leakage processes.

Figure 38(c) displays E_a for the low TDD Ge photodetector. The change in E_a results from different leakage current mechanisms in the different temperatures. E_a for the low TDD Ge photodetector differs at -0.1 V, depending on the temperature. E_a of 0.55 eV at 353 K indicates that the diffusion leakage current contributes mainly to I_{dark}. Low E_a of 0.21 eV at 293 K results from the dominant SRH and TAT leakage mechanisms. At high reverse bias voltage, E_a is reduced to 0.06 eV at 298 K. This is because the enhanced TAT leakage process contributes to high I_{dark} in a high electric field. E_a variation for the low TDD photodetector is more flexible than the high TDD Ge photodetector. The reduction in TDD alleviates the trap-related leakage processes, e.g., the SRH and TAT leakage processes. As a result, diffusion leakage contribution increases, leading to high E_a of 0.59 eV at 0.1 V. At high reverse bias voltage, the TAT leakage process is dominant. This leads to low E_a of 0.06 at -3 V.

Based on the extracted I_{surf} and I_{bulk} in Figure 37(b), E_a of I_{surf} and I_{bulk} for the low TDD Ge photodetectors are obtained in Figure 38(d). E_a of I_{surf} varies between 0.2 to 0.26 eV in the low temperature range (293 to 323 K). The reduction in E_a at high voltage results from enhanced SRH and TAT leakage processes. E_a of I_{bulk} is as high as 0.61 eV at -1 V in the high-temperature range (323 to 353 K). This results from the dominant diffusion leakage mechanism. The reduction in E_a at high voltage results from the enhanced TAT leakage process [110].

The SRH current density (J_{SRH}) and TAT current density (J_{TAT}) can be described by the following equations,

$$J_{SRH} + J_{TAT} = J_{SRH}(1 + \Gamma_{enhan}) \tag{17}$$

$$= \frac{qn_iW_d}{\tau_{eff}} = \frac{qn_iW_d}{\tau}(1 + \Gamma_{enhan}) \tag{18}$$

where Γ_{enhan} is a TAT enhancement factor. τ represents the SRH carrier lifetime [82]. Γ_{enhan} was suggested by Hurkx *et al.* to explain the TAT leakage process [110]. Γ_{enhan} is determined by a few parameters, i.e., electric field distribution, tunneling effective mass, and trap state energy. The low temperature improves Γ_{enhan}. Also, Γ_{enhan} is enhanced by a strong electric field. Thus, the low temperature and the high voltage improves the TAT leakage process [85]. This results in low E_a of <0.33 eV.

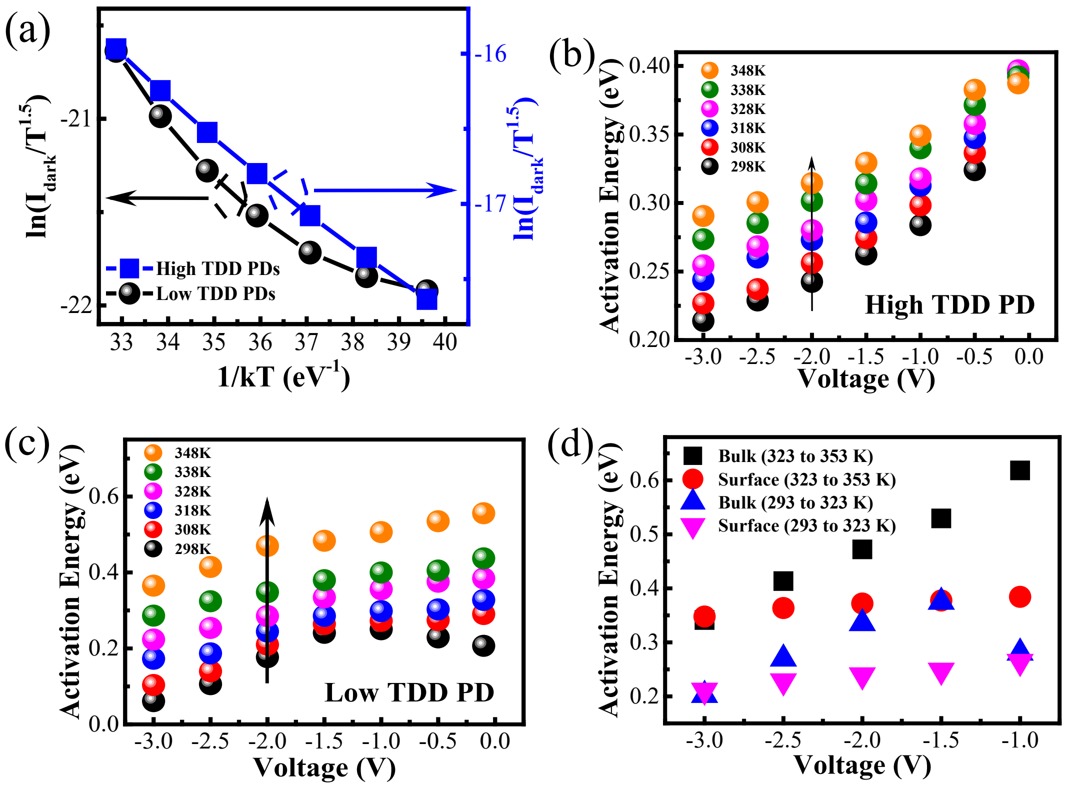

Figure 38. (a) The Arrhenius plot for the low and high TDD photodetectors at -3 V. E_a for (b) the high TDD photodetector and (c) the low TDD Ge photodetector as a function of voltage in the temperature range from 298 to 348 K. The arrows represent the temperature increasing from 298 to 348 K. (d) E_a of I_{surf} and I_{bulk} for the low TDD photodetector.

The BTBT leakage current is affected by the electric field in the depletion region. According to the features of the proposed BTBT leakage current equation [109], the BTBT leakage appears at the electric field intensity of >10^8 V/m. The electric field intensity for Ge photodetectors was calculated via the Lumerical DEVICE simulation, as shown in Figure 39. The maximum electric field increases from 3 × 10^6 to 6 × 10^6 V/m as voltage changes from -1 to -3 V. The calculated electric field is insufficient to cause the BTBT leakage process. Therefore, the BTBT leakage current contribution can be ignored in studying the analysis of leakage current mechanisms for the low TDD photodetector [84].

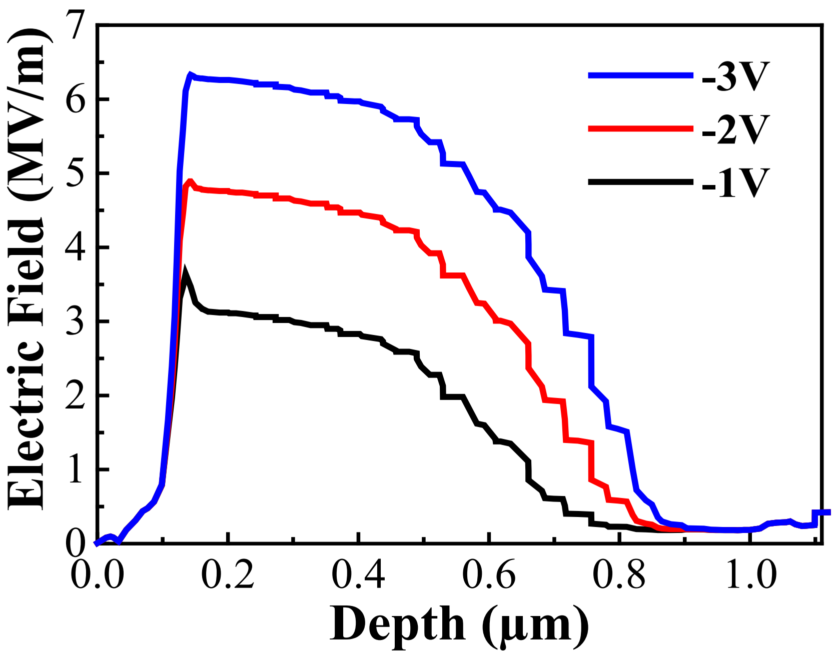

Figure 39. Calculated electric field distribution for the low TDD photodetector as a function of depth.

The temperature-dependent I_{dark}-V characteristics for low TDD photodetectors with GeO_x and with SiO_2 passivation were compared in the temperature range from 293 to 353 K in Figure 40(a). The temperature increases with the dark current for photodetectors. I_{dark} for the photodetector with GeOx is suppressed by 5 times in comparison with the photodetector with SiO_2 passivation in the temperature range.

The extracted J_{surf} for the photodetectors with GeO_x and SiO_2 surface passivation is shown in Figure 40(b). J_{sur} for the photodetector with GeO_x passivation is estimated to be 0.5 μA/cm at 293 K. In contrast, J_{sur} for the photodetector with SiO_2 passivation was obtained to be 5.9 μA/cm. It should be noted that J_{sur} is reduced by 10× for the photodetector with the GeO_x passivation. The suppression of I_{surf} via the GeO_x passivation is due to the improvement of the interface quality between Ge/GeO_x. I_{surf} for the photodetectors with SiO_2 passivation is attributed to the SRH and TAT leakage current. With the GeO_x passivation via the O_3 oxidation, lower defect states are present at the surface. As a result, the trap-related leakage processes, i.e., SRH and TAT leakage processes, are suppressed, leading to the reduction in I_{surf}.

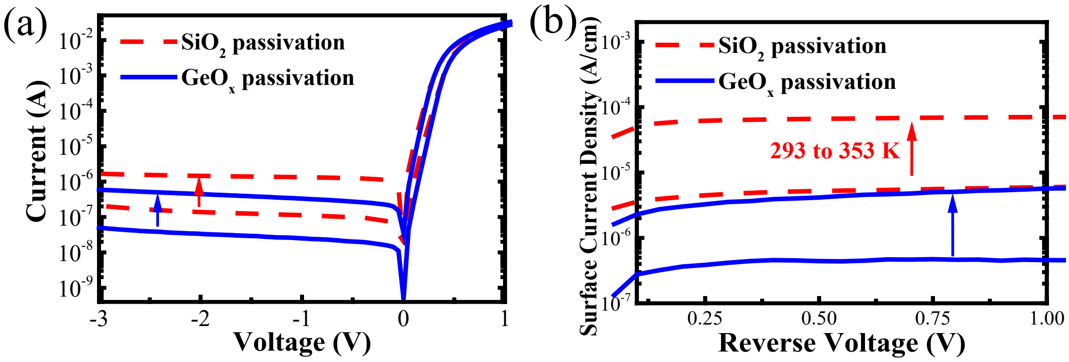

Figure 40. (a) Temperature-dependent I_{dark}-V curves for low TDD photodetectors with GeO_x and with SiO_2 passivation in the temperature range from 293 to 353 K. (b) Extracted J_{surf}-V curves for photodetectors with GeO_x and with SiO_2 passivation in the temperature range from 293 to 353 K. The arrows in Figure 40(a) and (b) represent the increase in temperature from 293 to 353 K.

Arrhenius plot for photodetectors with GeO_x and with SiO_2 passivation is illustrated in Figure 41(a). The $ln(I_{dark}/T^{1.5})$ variation is large at low voltage, while the variation is small at high voltage. Based on Eq. (3), E_a can be extracted from Figure 41(a). Figure 41(b) displays E_a for the photodetector with GeO_x passivation as a function of voltage. At 348 K, E_a at -0.1 V shows 0.55 eV, meaning that the diffusion leakage process is dominant. E_a is obtained to be 0.2 eV at 293 K, meaning that the TAT leakage process is dominant. Where voltage increases to -3 V, the E_a is reduced to 0.0 eV, showing that the TAT leakage process is enhanced at the high reverse bias voltage. The increase in E_a with temperature results from the enhanced diffusion leakage contribution.

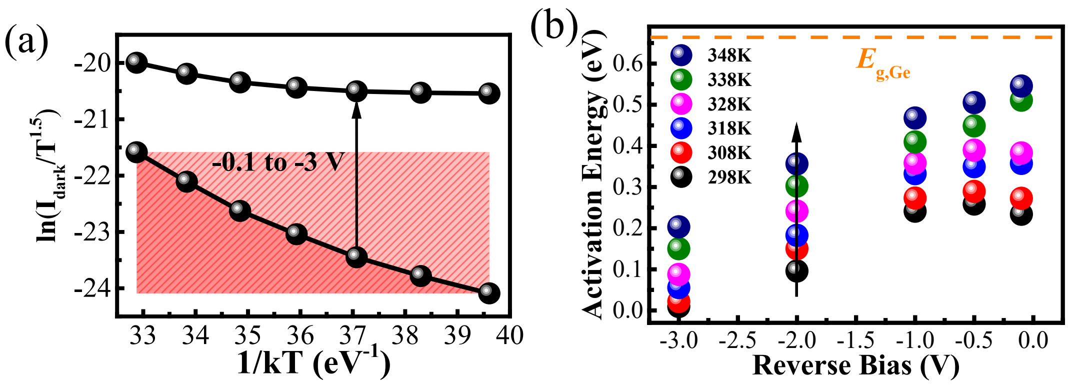

Figure 41. (a) Arrhenius plot for the photodetector with GeO_x passivation. The arrow represents the voltage increase from -0.1 to -3.0 V. (b) E_a for the photodetector with GeO_x passivation in the temperature range from 298 to 348 K. The arrow represents the temperature increase from 298 to 348 K.

3.4.3 Effective Lifetime Analysis

Defects/dislocations in epi-Ge contribute to the effective carrier lifetime. Also, the defects/dislocations generate the trap states, increasing the SRH and TAT leakage current. The effective carrier lifetime (τ_{eff}) study provides the relationship with the leakage current for Ge photodetectors. τ_{eff} related to the trap-related leakage processes can be expressed by the following equation,

$$\frac{dI_{dark}}{dW_d} \approx \frac{dI_{diff}}{dW_d} + \frac{dI_{SRH}+dI_{TAT}}{dW_d} \approx \frac{en_i}{\tau_{eff}} \tag{19}$$

where I_{diff} is the diffusion current. Epi-Ge thickness for low and high TDD Ge *p-i-n* structures differs. Therefore, the τ_{eff} analysis provides normalized impact on τ_{eff}. W_d was estimated via the capacitance-voltage (*C-V*) experiment, as shown in Figure 42(a). The junction and the parasitic capacitance are estimated by linear-fitting of capacitances against the mesa areas [111]. The estimated W_d for low TDD photodetectors is thin compared with high TDD photodetectors, resulting from the O_2 anneal and HF etching processes.

n_i was referred from Ref. 106 to extract τ_{eff}. Figure 42(b) shows the extracted τ_{eff} for photodetectors. Extracted τ_{eff} for high and low TDD photodetectors was 2.9×10^{-9} and 5.7×10^{-7} s at 0.5 V, respectively. It should be noted that τ_{eff} for the low TDD photodetector is reduced by ~100× in comparison with the high TDD photodetector. The reduction in τ_{eff} is corresponding to the reduction in TDD [112]. τ_{eff} is extracted to be 2.2×10^{-10} and 4.8×10^{-8} s for high and low TDD photodetectors at -3.0 V, respectively due to the enhanced TAT leakage process.

Figure 42(c) represents temperature-dependent τ_{eff} for I_{bulk} at -1V. τ_{eff} for low TDD Ge photodetector was extracted to be the order of 10^{-7} s at -1 V in the temperature range, which is enhanced by <100× in comparison with the high TDD photodetector. τ_{eff} for the high TDD photodetector increases as the temperature increases. The diffusion leakage process increases in high temperature, leading to improved τ_{eff}. Voltage-dependent τ_{eff} for the low TDD photodetectors is shown in Figure 42(d). τ_{eff} decreases at 293 K as the voltage increases. This results from the improved TAT leakage process. τ_{eff} is reduced at 353 K as the voltage increases. The τ_{eff} variation in the voltage change is suppressed at high temperature due to the suppressed TAT leakage process [85].

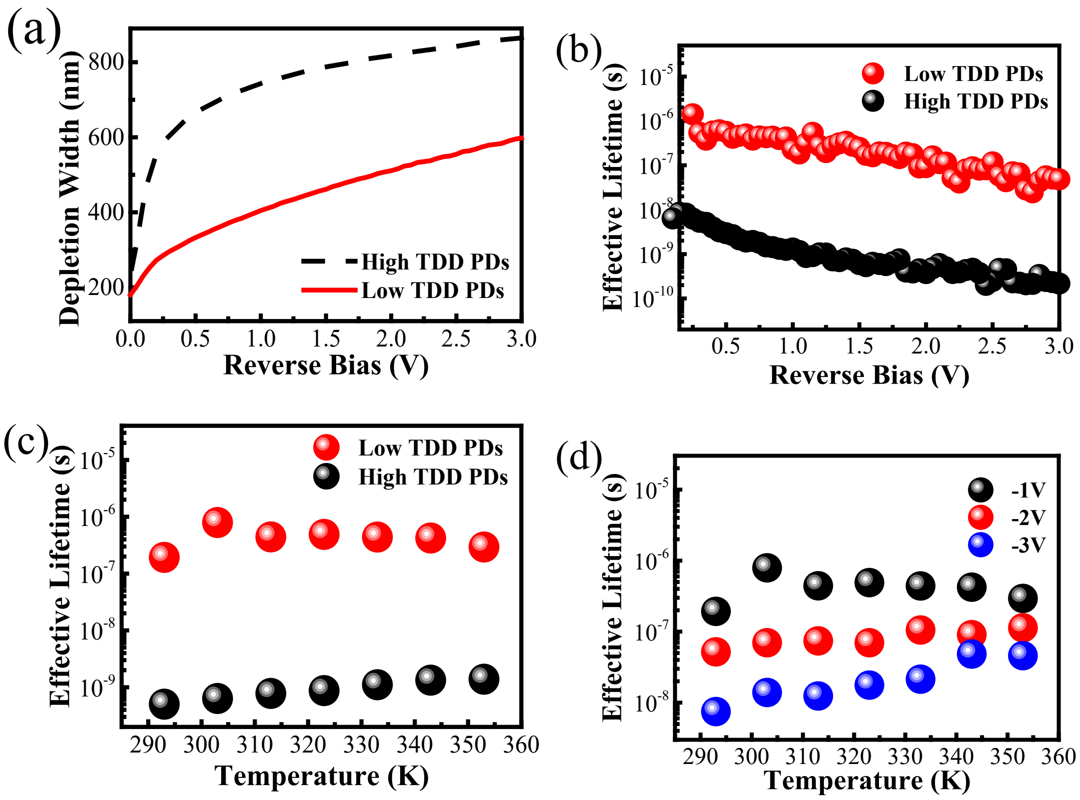

Figure 42. (a) Extracted W_d for low and high TDD photodetectors. (b) τ_{eff} for I_{bulk} of the low and high TDD photodetectors at 343 K. (c) τ_{eff} for I_{bulk} of the low and high TDD Ge photodetectors as a function of temperature. (d) τ_{eff} for the low TDD photodetector as a function of temperature.

Figure 43 displays the benchmarking of τ_{eff} for the Ge photodetectors in comparison with the reported SRH lifetime (τ) for *pn* Ge junctions. Modeling τ is obtained from Ref. 112. TDD is reversely proportional to the SRH lifetime. Reported τ follows the trend of modeling τ. Extracted τ_{eff} for low and high TDD photodetectors is in good agreement with the modeling τ. τ_{eff} for low TDD is enhanced by 185× compared with τ_{eff} for high TDD. It should be noted that the improvement in τ_{eff} is attributed to the reduction in TDD [112].

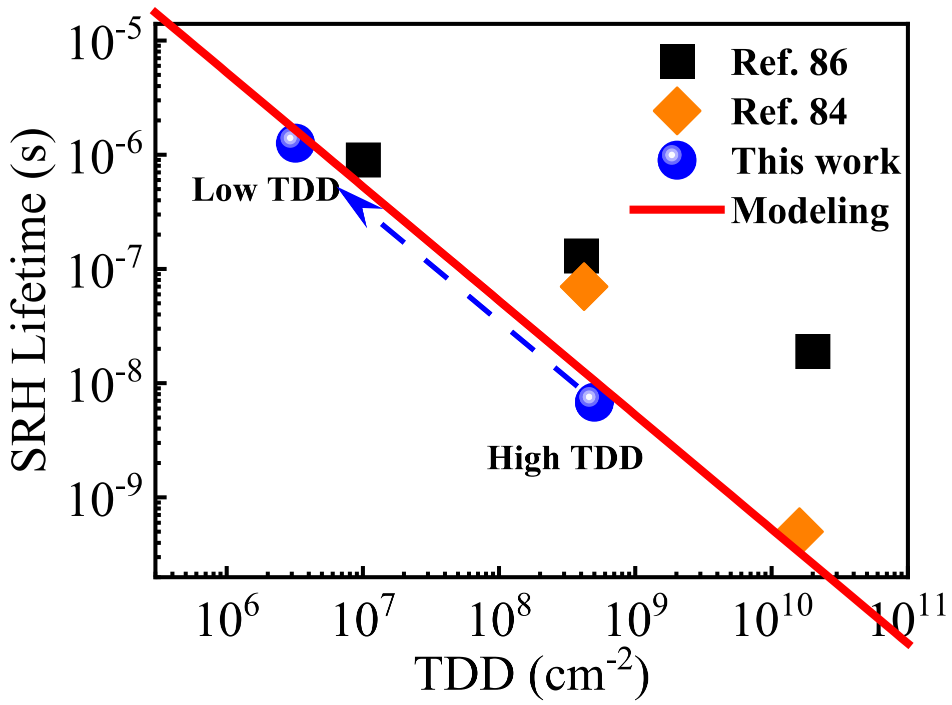

Figure 43. Benchmarking of τ_{eff} for the low and high TDD photodetectors with τ for pn Ge junctions [84].

3.4.4 Photocurrent Characteristic

The optical response is conducted with 2401 Keithley SourceMeter and a tunable laser operating in the wavelength range from 1500 to 1630 nm. Single-mode optical fiber is used for the incidence illumination on the devices. The photoexcited carriers are collected by a probe station connecting to electrodes of the fabricated photodetectors. The output optical power was calibrated by using an optical power meter. Figure 44(a) shows photocurrent-voltage (I_{photo}-V) curves for high and low TDD photodetectors at 1,550 nm. I_{photo} is generated when the light is on, meaning that EHPs are created, and they are swept to the electrodes. The responsivity can be obtained by using Eq. (14). Calculated responsivity for high and low TDD photodetectors was 0.41 and 0.24 A/W, respectively. Reduced responsivity for low TDD photodetector results from the decrease in the penetration depth due to thin intrinsic-germanium (*i*-Ge). The responsivity is normalized by providing the responsivity per the unit of the Ge thickness in Figure 44(b). The responsivity per the thickness unit is reduced at high voltage. This is because of the Franz-Keldysh effect [114]. The low TDD photodetector shows high responsivity per the unit of thickness at low voltage, while the value is degraded at high voltage. This is because a strong electric field distribution improves the Franz-Keldysh effect.

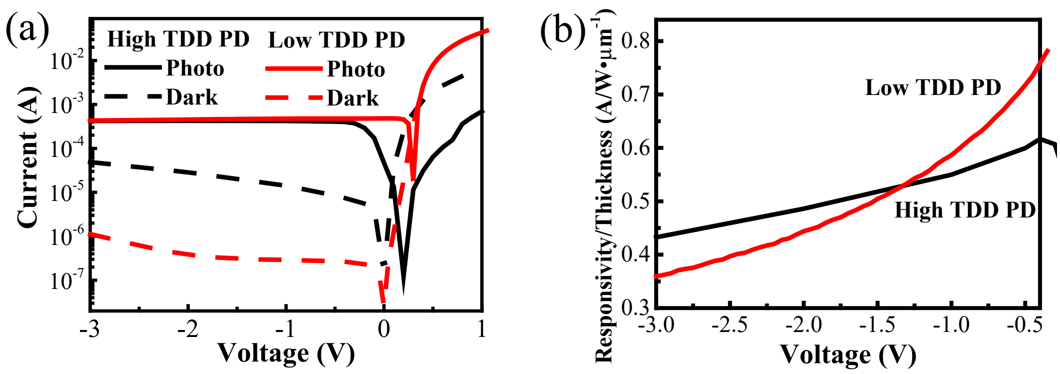

Figure 44. (a) I_{photo}-V characteristics for high and low TDD photodetectors. (b) The thickness-normalized responsivity for high and low TDD photodetectors at 1,550 nm.

The photo-response for low TDD photodetectors with GeO_x passivation is investigated. I_{dark} and I_{photo}-V curves are obtained at 1,550 nm Figure 45(a). The responsivity for the GeO_x-passivated photodetector was 0.28 A/W. It should be noted that the optical responsivity can be improved with thick epi-Ge or photon-trapping hole arrays. The responsivity varies from 0.27 and 0.29 A/W as voltage increases from 0 and -3 V. The increase in responsivity results from the suppressed Franz-Keldysh effect [114]. This means that the low power consumption is suitable for photodetectors to operate at low voltage. The inset of Figure 45(a) represents photocurrent as a function of output power with its linear fitting. The non-linear optical effect is observed in the output power range. Figure 45(b) shows the responsivity spectra with respect to wavelength. The responsivity decreases from 0.42 to 0.05 A/W with increasing wavelength. Given the thickness of *i*-Ge (~350 nm), the obtained responsivity values are considerable. The absorption coefficient (α) for low TDD epi-Ge can be estimated by the following equation,

$$\alpha = -\frac{1}{t_{Ge}} ln\,(1 - hv\frac{R}{1-r}) \tag{20}$$

where t_{Ge}, is the *i*-Ge thickness [115]. r is reflectivity. r can be calculated based on Fresnel equations. The extracted α scanning is obtained in the inset in Figure 45(b). α for low TDD epi-Ge is higher than bulk Ge [117]. This improvement originates from two factors; i) the tensile strain in the Ge layer, and ii) the improved optical confinement due to the insulator platform.

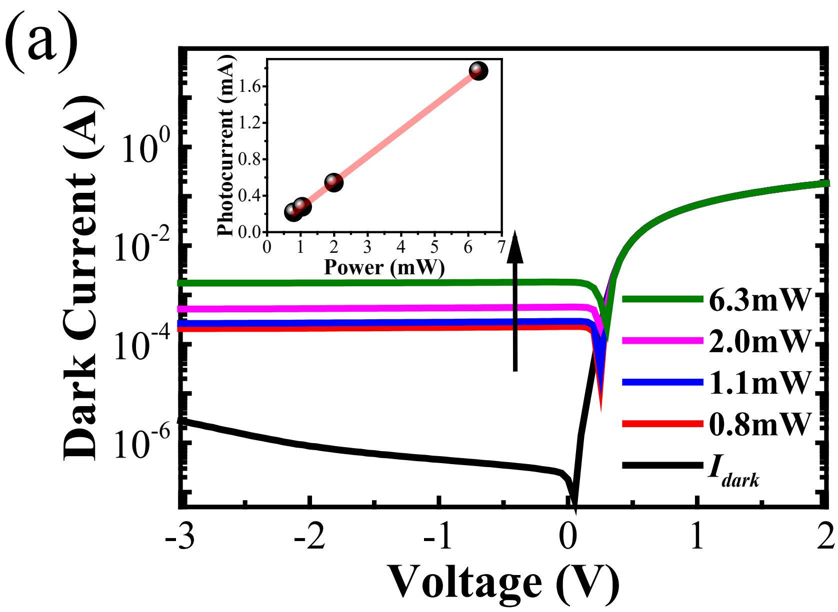

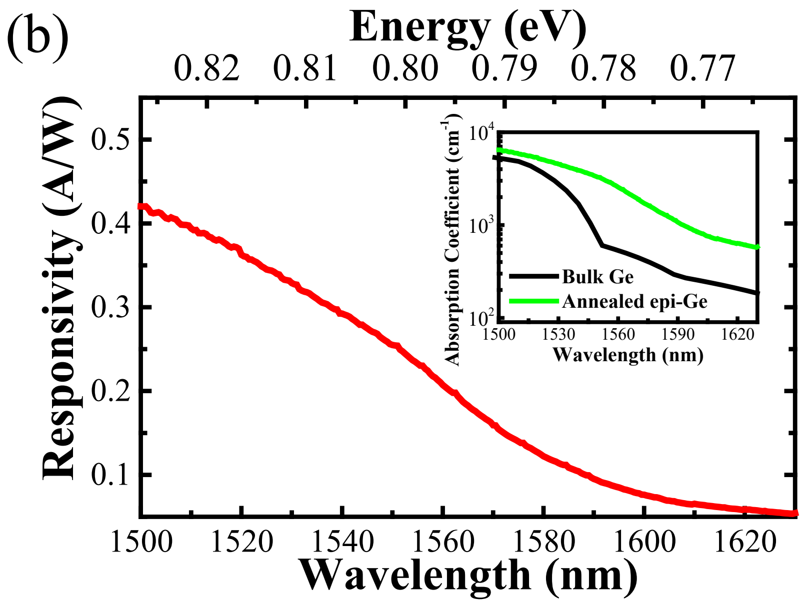

Figure 45. (a) I_{photo} for low TDD photodetector with GeO_x passivation. The arrow represents the incident power increases from 0.8 to 6.3 mW. Inset in Figure 45(a) displays photocurrent for the photodetector as a function of the output optical power. (b) The responsivity spectrum in the wavelength range from 1500 to 1630 nm. Inset in Figure 45(b) shows the extracted α spectra as a function of wavelength. The α spectra for Ge bulk are referred to Ref. 117.

The responsivity for the low TDD photodetector with GeO_x passivation at 1,550nm is benchmarked with the reported normal incidence vertical Ge photodetectors in Figure 46. The dark current densities were obtained at -1 V. The reported photodetectors on Ge/Si and Ge/SOI platforms show high J_{dark} of > 1 mA/cm^2, which degrades the performances of photodetectors in terms of specific detectivity and NEP. In contrast, the low TDD GOI photodetector with the GeO_x passivation shows the ultra-low J_{dark} of < 1mA/cm^2. It should be noted that the responsivity can be further enhanced i) by employing the micro-hole array structures [63] and ii) by growing thick epi-Ge.

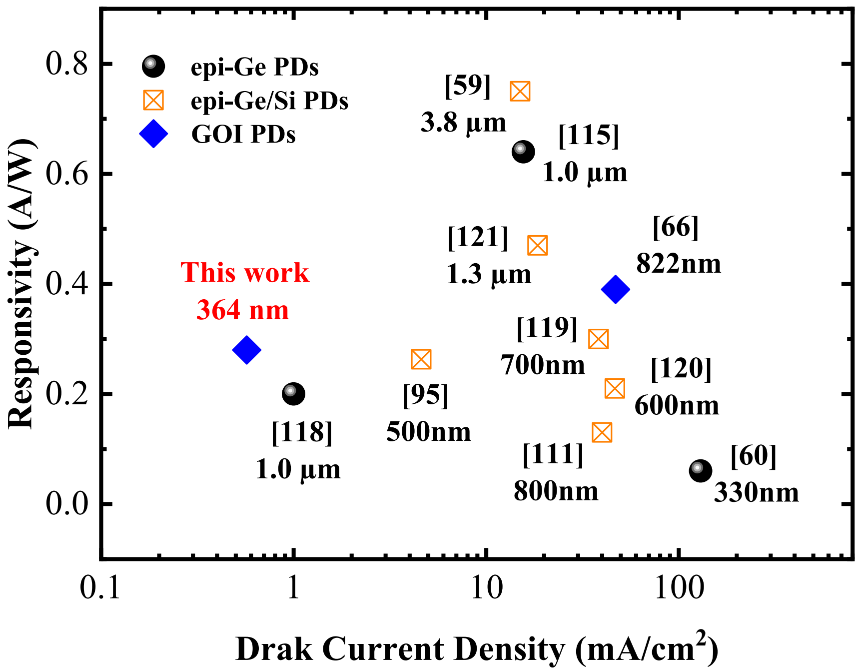

Figure 46. Benchmarking of responsivity for the reported epi-Ge vertical photodetectors at 1,550 nm. The epi-Ge/Si PDs represent the photodetectors with heterojunction of Ge/Si structure. The *i*-Ge thicknesses are indicated below the Ref. 59,60,66,95,111,115,118-121.

3.4.5 Frequency Response

The frequency response for low TDD photodetectors was performed using a lightwave component analyzer (Keysight N4373D), which can measure 3dB bandwidth up to 15 GHz. The selected wavelength for 3dB bandwidth was 1,550 nm. Figure 47(a) displays the normalized frequency response for photodetectors with GeO_x and with SiO_2 passivation. The 3dB cut-off frequency for photodetectors with the SiO_2 and GeO_x passivation was obtained to be 0.88 and 1.72 GHz at -1 V, respectively. The 3 dB bandwidth is improved by 2× for the photodetector with GeO_x passivation. The 3dB bandwidth for the GeO_x-passivated photodetectors with different mesa sizes is shown in Figure 47(b). The higher the 3dB bandwidth, the smaller the mesa diameter, signifying that 3dB bandwidth is restricted mainly by the (resistance-capacitance) R_eC-limited delay. Through *C-V* experiments, it is found that the capacitance for the SiO_2-passivated photodetector was measured to be 1.6 pF while the capacitance for the GeO_x-passivated photodetector was obtained to be 1.1 pF. The capacitance is reduced by 0.5 pF. The capacitance of a photodetector consists of the bulk, sidewall, and parasitic capacitances. The defect density determines the sidewall capacitance on the sidewall. It has been reported that the interface defect density contributes to the total capacitance in metal-oxide-semiconductor (MOS) devices [122]. With the GeO_x passivation, the interface quality is improved, leading to the suppressed capacitance.

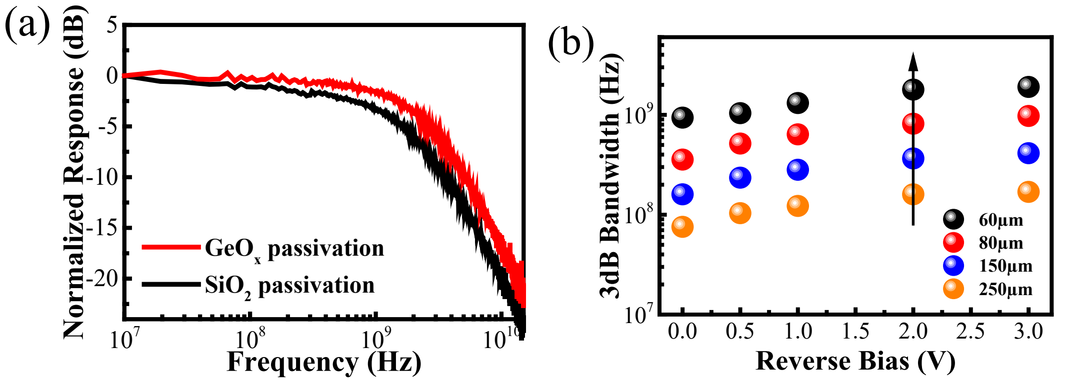

Figure 47. (a) Frequency response for low TDD photodetectors with GeO_x and with SiO_2 passivation. (b) 3dB bandwidth for the photodetector with varying mesa sizes as a function of voltage. The arrow indicates a decrease in the mesa diameter.

The 3dB bandwidth (f_{3dB}) for the GeO_x-passivated photodetector can be extracted theoretically using the following equations [66],

$$f_{3dB} = \sqrt{\frac{1}{f_T^{-2}+f_{RC}^{-2}}}, \tag{21}$$

$$f_{RC} = \frac{1}{2\pi R_e C}, \tag{22}$$

$$f_T = \frac{0.45 v_{sat}}{W_b}, \tag{23}$$

where f_{RC} and f_T are the *RC* delay-limited bandwidth and carrier transit-limited bandwidth, respectively. v_{sat} represents the saturated Ge drift velocity. R_e is composed of two resistances, i.e., the series resistance ($R_{e,series}$ = 19 Ω at 2 V) and the load resistance ($R_{e,load}$ = 50 Ω). C can be separated into parasitic capacitance (C_p) and junction capacitance (C_j). C_j increases with the mesa area (A), while C_p is constant. The inset in Figure 48(a) displays C as a function of the mesa area. C_p and C_j are estimated by obtaining the intercept and the slope from the linear fitting. Extracted C_j and C_p are 1.06 and 0.13 pF, respectively. v_{sat} is 6 × 10^6 cm/s. d_i can be estimated in Figure 48(a) according to the equation of $W_d = \varepsilon A/C_j$, where ε is the Ge permittivity. Estimated W_d is obtained to be 200 nm at 0 V. W_d increases to 700 nm at -5 V. f_T is restricted by W_{d} and v_{sat}. Estimated f_T varies from 130 to 39 GHz as d_{i} increases from 200 to 700 nm. It should be noted that f_T is further improved to > 100 GHz at 0 V owing to a thin depletion width of 200 nm. f_{3dB} for the photodetectors with various diameters from 60 to 250 μm is mainly attributed to f_{RC}. Because the mesa size determines f_{RC} mainly, it can be expected that f_{3dB} can be further enhanced by reducing the device diameter. By assuming that C_j is proportional to the mesa size, estimated f_{3dB} is obtained as a function of mesa diameters along with the measured 3dB bandwidth in Figure 48(b) at -1 V. The impact of C_p is excluded for the calculation. The experimental f_{3dB} is in good agreement with the estimated f_{3dB}. The measured 3dB bandwidth is a bit underestimated, resulting from the existence of the parasitic capacitance. It should be noted that f_{3dB} can be further enhanced up to ~70 GHz as the diameter is reduced to 5 μm, thanks to the large f_{T} of 72 GHz at -1 V.

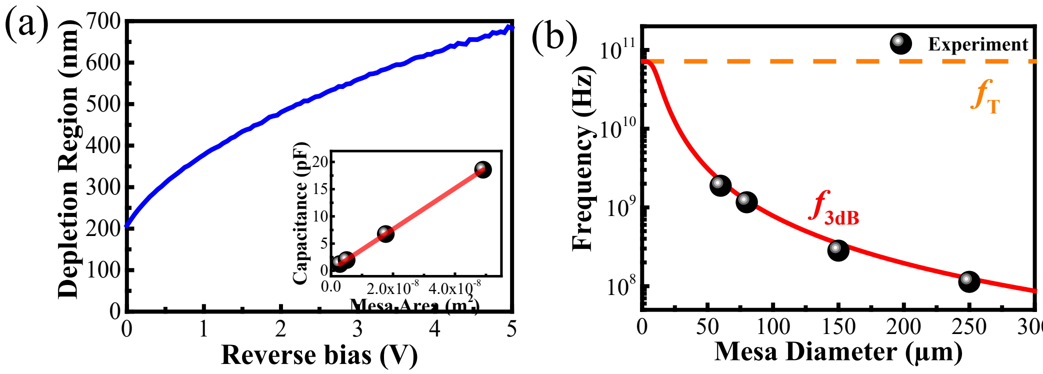

Figure 48. (a) Extracted W_d as a function of reverse bias. Inset in Figure 48(a) represents capacitance as a function of mesa area. (b) Measured f_{3dB} with expected 3dB bandwidth.

3.5 Summary

A systematic study on the normal incidence vertical *p-i-n* GOI photodetector with GeO_x passivation was conducted in Chapter 3. Low TDD Ge (~10^6 cm^{-2}) was achieved via O_2 anneal and HF etching processes. This is reduced by two orders of magnitudes in comparison with the GOI platform without the O_2 anneal (TDD of ~10^8 cm^{-2}). Thanks to the alleviation of TDDs, J_{dark} for low TDD Ge photodetectors was reduced by 53 times. Through E_a study, it is revealed that the diffusion current governs I_{dark} in the high-temperature range. In contrast, the leakage current for the high TDD photodetectors is governed by the SRH leakage process. I_{surf} for low TDD photodetectors with SiO2 passivation is governed by the TAT and SRH leakage mechanisms. The τ_{eff} study was associated with the trap-related leakage current, i.e., TAT and SRH leakage current, for photodetectors. τ_{eff} for low TDD photodetectors was estimated to be 1.3×10^{-6} s at -0.5 V. This is improved by two orders of magnitude compared with τ_{eff} for high TDD Ge ones.

As TDD decreases, I_{dark} is determined by I_{surf}. The I_{surf} contribution reaches 96% of I_{dark} for the low TDD Ge photodetector. Significant I_{surf} requires advanced surface passivation to suppress I_{dark}. The GeO_x passivation was proposed to improve the surface quality. Thanks to the GeO_x passivation, J_{dark} for the low TDD photodetector was measured to be 0.6 mA/cm^2 at -1 V. Estimated J_{surf} and J_{bulk} were 0.6 μA/cm and 0.5 mA/cm^2, respectively. The optical responsivity for the low TDD photodetector with GeO_x passivation was obtained to be 0.28 A/W at 1,550 nm. The estimated absorption coefficient for low TDD Ge on insulator is higher than the one for Ge bulk, resulting from the residual tensile strain and improved optical confinement. The 3dB bandwidth for the GeO_x-passivated photodetector was 1.72 GHz at -1 V. The 3dB bandwidth is theoretically extracted with respect to the mesa diameter, and the 3dB bandwidth of 70 GHz can be obtained with a 5 μm mesa diameter. In Chapter 3, the normal incidence vertical *p-i-n* Ge photodetectors with sub-mA/cm^2 of J_{dark} are demonstrated for low-cost and CMOS compatible Si-based PICs.

Chapter 4. Hole Array GOI Photodetectors for Improved Responsivity and Specific Detectivity

In this chapter, gourd-shaped hole array normal-incidence *p-i-n* GOI photodiodes will be investigated. In Chapter 4.1, the drawback of the Ge photodetectors and the various approaches to improve the responsivity will be introduced. Chapter 4.2 consists of the optimization of hole array parameters and the demonstration of hole array photodiodes. In Chapter 4.3, characteristics of the hole array GOI photodiodes are performed. Finally, Chapter 4 is summarized in Chapter 4.4. Chapter 4 aims to obtain remarkable performance of epi-Ge photodiodes, which is superior to commercial Ge bulk/ III-V photodiodes.

4.1 A Drawback of Ge Photodetectors – Low External Quantum Efficiency

Conventionally, Ge photodetectors have been demonstrated on Si substrate, suffering from low responsivity. Thus, incorporating with Sn or a thick *i*-Ge layer has been introduced to improve the responsivity [59]. The responsivity for the Ge photodetector with the *i*-Ge thickness of 1,000 nm [115] is improved from 0.05 to 0.64 A/W in comparison with the Ge photodetector with the *i*-Ge thickness of 330 nm [60]. An increase in *i*-Ge layer depth provides long optical penetration depth so that most of the photons can be absorbed in the active region. The responsivity for the GeSn photodetectors was enhanced from 0.10 to 0.22 A/W as the Sn content increases from 0 to 4.2% [70]. The introduction of Sn into Ge provides high absorption coefficient theoretically. However, both approaches result in huge dark current densities due to enhanced SRH and TAT leakages mechanisms. In addition, for the thick *i*-Ge, the 3dB bandwidth is restricted owing to the long carrier transit time. The introduction of Sn requires low-temperature growth to add Sn atoms into Ge, which causes the high defective misfit/threading dislocations.

Alternatively, an insulator platform has been promising to improve optical responsivity. For normal incidence photodiodes, the insulator substrate causes vertical-cavity modes, enhancing optical confinement. The insulator substrates have been demonstrated in either SOI or GOI. Ge photodetectors on SOI show a high dark current density resulting from the defective Ge/Si interface. Thus, the GOI platform is promising for low dark leakage current density and improved optical responsivity [97]. In Chapter 3, low TDD photodetectors with GeO_x passivation showed the dark current density of sub-mA/cm^2.

Recently, the tetraethy-lorthosilicat layer was inserted between Ge and BOX layers to improve optical responsivity [123]. The responsivity can be obtained to be as high as 0.5 A/W. The photon-trapping hole structures and the dual-absorption structure were also introduced to improve optical responsivity [63]. The hole-array Ge photodiodes on SOI displayed the responsivity of 0.91 A/W, which is equivalent to EQE of 80%. Also, 3dB bandwidth is enhanced because the photon-trapping hole array structure reduces the effective mesa area. Dual-absorption structure provides the improved responsivity and high 3dB bandwidth due to the folded n^+-i-p^+-i-n^+ structures [65]. Although the recently demonstrated Ge photodiodes provide high responsivity of 0.91 A/W [63] and 3dB bandwidth of 49GHz [60], those photodetectors showed the high dark current densities of >10 mA/cm^2, degrading specific detectivity (D^*).

In Chapter 4, the gourd-shaped hole array vertical *p-i-n* GOI photodetectors with GeO_x passivation were introduced. The parameters for the hole array design are optimized via simulation. The gourd-shaped hole design shows enhanced optical absorption in comparison with the cylinder-shaped hole design via the FDTD method. As a result, the responsivity for gourd-shaped hole array photodetectors is improved by 2.5×. Importantly, D^* for the hole array photodetector is extracted, and it is compared with commercial bulk Ge/extended-InGaAs photodetectors. The hole array vertical *p-i-n* GOI photodetector with GeO_x passivation paves the way toward high-efficiency photodetection for Si-based PICs.

4.2 Demonstration of Hole Array GOI Photodetectors

In this section, hole array structure is optimized using the FDTD method in Chapter 4.2.1. After that, the hole array photodiodes are demonstrated on the GOI platform in Chapter 4.2.2.

4.2.1 Design of Hole Array Structure

The electric field distribution of the GOI platform is calculated to study the influence of the insulator and the hole array structures using the FDTD method, considering a periodic boundary condition. The polarization dependence was not considered owing to the round shape of the holes. For the simulation, the window size is determined to be 1.55 μm × 1.55 μm × 9.00 μm, and the time step is selected to be 0.028 fs. The mesh with a 1.30 μm × 1.30 μm × 2.00 μm size is defined in the hole structures. The structures for the simulation consist of i) Ge on Si, ii) Ge on insulator, iii) Ge on insulator with cylinder-shaped hole array, and iv) Ge on insulator with gourd-shaped hole array. For the simulation, the Si substrate was inserted at the bottom and the Ge layer with 1.1 μm thickness was built on the Si substrate. SiO_2 with 200 nm of thickness was placed on the top of the Ge layer. The GOI platform contains the same structure with the GOS platform, but adds the insulating layers of SiO_2/SiN/SiO_2 between the Ge layer and the Si substrate. The cylinder-shaped hole array is designed on the GOI platform. The diameter of the hole is 1.16 μm with the height of 800 nm. The gourd-shaped hole array consists of the same design that the cylinder-shaped hole array is built. The round shape at the sidewall was made to be 1.24 μm at the middle of the round-shaped hole array. The unit cell in the size of 1.55 × 1.55 × 9.00 μm^3 is applied to extract the reflectance and the transmittance. The polarization dependence is not considered in the simulation due to the polarization-independent round shape of the holes.

Figure 49(a) displays the calculated reflectance of each platform. The reflectance is reduced for the insulator platform compared with the Ge on Si platform. Where the hole arrays are included in the simulation, the reflectance dramatically drops, leading to enhanced optical absorption. Especially, the gourd-shaped hole array provides lower reflectance compared to the cylinder-shaped hole array. It has been reported that the hourglass-shaped vertical nanowires benefit from low reflectance [125]. The reflectance of the gourd-shaped hole array decreases by 2.6× in comparison with the cylinder-shaped hole array due to the gradient changes in diameter in the vertical direction.

Figure 49(b) shows the calculated absorption spectra for each platform. The absorption (A_{absor}) is extracted by A_{adsor}=1-R_{reflec}-T_{trans} where R_{reflec} and T_{trans} are reflectance and transmittance, respectively. The GOI platform provides improved absorption compared with the Ge on Si platform. With the hole array structures, the absorption spectra increase dramatically. The absorption for the gourd-shaped hole array design is higher than the cylinder-shaped hole array.

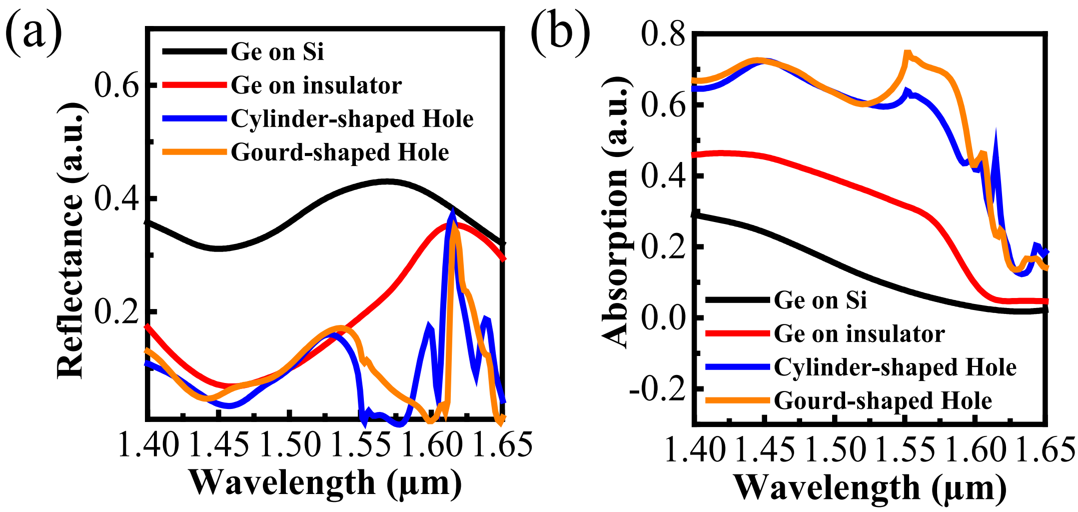

Figure 49. (a) Calculated reflectance spectra for various platforms. (b) Calculated absorption spectra for various platforms.

Figure 50(a) and (d) illustrate the cross-sectional views of the electric field distribution for Ge on Si and GOI platforms, respectively. It is observed that the electric field confinement for the GOI platform is enhanced. The cross-sectional views for various hole arrays on the GOI platform are displayed in Figure 50(b) and (e). It is obvious that the high electric field is confined in the active region. Because the hole array traps the photons, the vertical resonance mode is additionally observed.

The planar views of electric field distribution at the middle depth of each hole are simulated to distinguish the different hole shapes in Figure 50(e) and (f). The cylinder- and gourd-shaped hole arrays are adopted for the simulation, as shown in Figure 50(c) and (f). The electric field intensity for the gourd-shaped hole array is higher than the cylinder-shaped hole array. This is due to the low reflectance of the gradient diameter in the vertical direction.

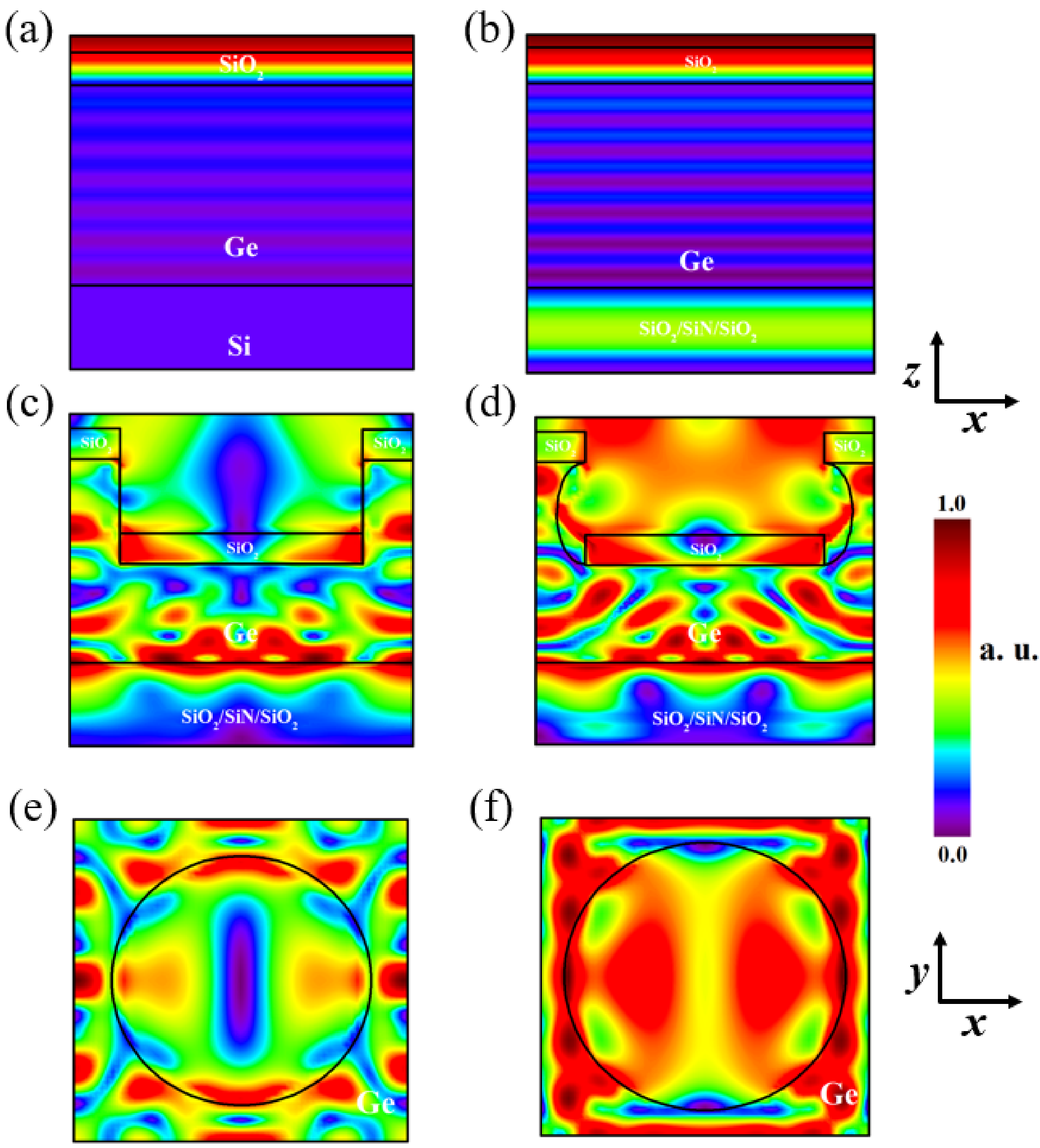

Figure 50. Cross-sectional view of electric field distribution for (a) Ge on Si and (b) GOI. (c) Cross-sectional and (e) top views of electric field distribution in GOI with the cylinder-shaped hole array structure. (d) Cross-sectional and (f) top views of electric field distribution in GOI with the gourd-shaped hole array structure. The simulated area is a unit cell. The wavelength of 1,550 nm is selected for the simulation.

The hole array period and hole diameter should be properly selected to optimize the optical absorption in the active region. The gourd shape is adopted for the hole array optimization. The hole array period ranges from 1.35 to 1.75 μm with an interval of 0.2 μm. The hole diameter ranges from 1.00 to 1.32 with an interval of 0.16 μm. Figure 51(a) represents the absorption spectra for the gourd-shaped hole array with a consistent period of 1.55 µm. The absorption is enhanced as either the diameter increases or decreases from 1.16 µm. Figure 51(b) represents the absorption spectra for the gourd-shaped hole array where the hole array period is 1.16 µm. The high absorption is 0.75 for the period of 1.55 µm at 1,550 nm. The absorption at 1,550 nm with different hole array periods and diameters is shown in Figure 51(c). The hole array diameter of 1.16 µm and period conditions of 1.55 µm provide the highest absorption of 0.75.

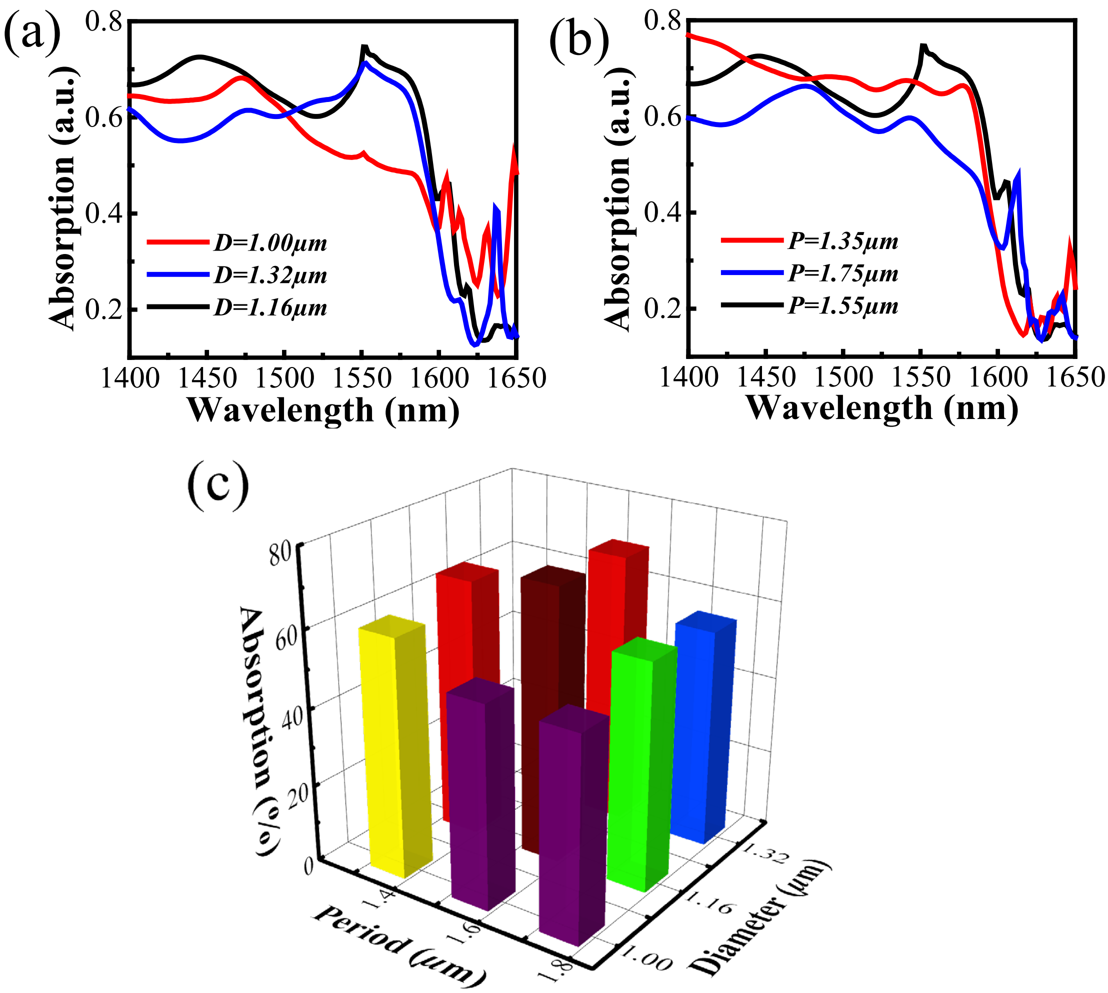

Figure 51. (a) The absorption spectra for the gourd-shaped hole design with a period of 1.55 µm. (b) The absorption spectra for the gourd-shaped hole design with a diameter of 1.16 µm. (c) Simulated absorption for various hole array parameters at 1,550 nm.

4.2.2 Demonstration of Gourd-shaped Hole Array GOI Photodetectors

The demonstration of the low TDD GOI platform follows the same steps described in Chapter 3.3. Two fabrication steps are different from the previous fabrication; i) a dopant for *n*-type formation, and ii) the formation of the gourd-shaped hole array structures. The *n*-type ion implantation is performed with Phosphorus (P). The dose for the P ion implantation is selected to be 1×10^{15} cm^{-2} and the ion energy is 25 keV with 7° tilted angle. The SIMS profiles of P and B doping concentrations for vertical *p*-*i*-*n* structures are shown in Figure 52(a). The SRP analysis for vertical *p*-*i*-*n* GOI structures is performed in Figure 52(b). The p^+- and n^+-regions are observed in the bottom and top epi-Ge, respectively. The p^+- and n^+-type doping concentrations are obtained to be 5×10^{19} and 5×10^{18} cm^{-3} in shallow regions. The activated doping concentration of B is consistent with the previous one in Chapter 3.2, while the *n*-type doping concentration differs from the vertical GOI *p*-*i*-*n* structure. Low n-type concentration could cause high dark current due to enhanced diffusion current.

One time of electron-beam lithography (EBL) was first implemented to pattern hole array patterns on the low TDD GOI surface. The hole array diameter and period are varied. The period ranges from 1.50 to 1.60 μm with an interval of 0.05 μm, and the diameter ranges from 0.98 to 1.42 μm with the interval of 0.04 μm during the fabrication. The voltage and dose should be properly selected during the EBL process to get rid of damage on a sample or either underexposure or overexposure. Sulphur hexafluoride (SF_6)-based inductively coupled plasma ion etching (ICP-RIE) is conducted for the gourd-shaped hole array formation. After defining the *p*- and *n*-type mesa, the GeO_x oxidation process, i.e., the 1nm Al_2O_3 deposition and the O_3 oxidation, was performed to cover the sidewall of hole array structures with GeO_x/Al_2O_3.

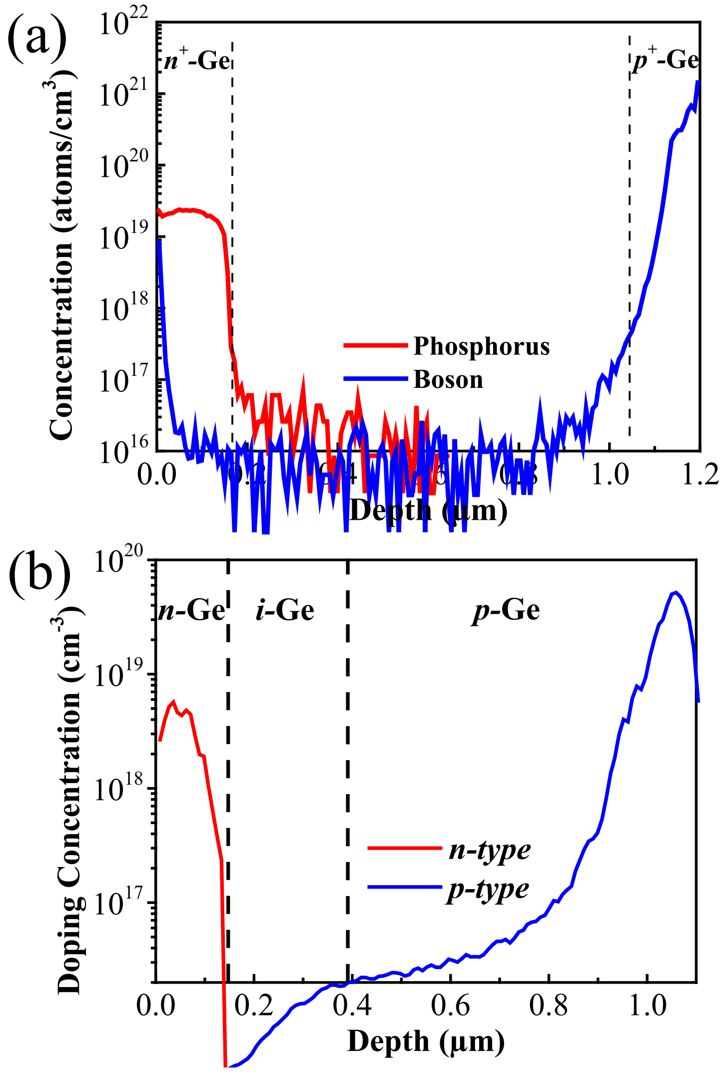

Figure 52. (a) The SIMS profiles of B and P dopants for the vertical *p-i-n* structure. (c) The SRP profiles of B and P dopants for the vertical *p-i-n* structure.

The top SEM view for the hole array photodetector is shown in Figure 53(a). The hole array structure was designed at the mesa center. The zoom-in SEM image of the hole array area in the red-squared area in Figure 53(a) is shown in the inset of Figure 53(a). The 3D schematic image of the hole array photodetector is displayed in Figure 53(b).

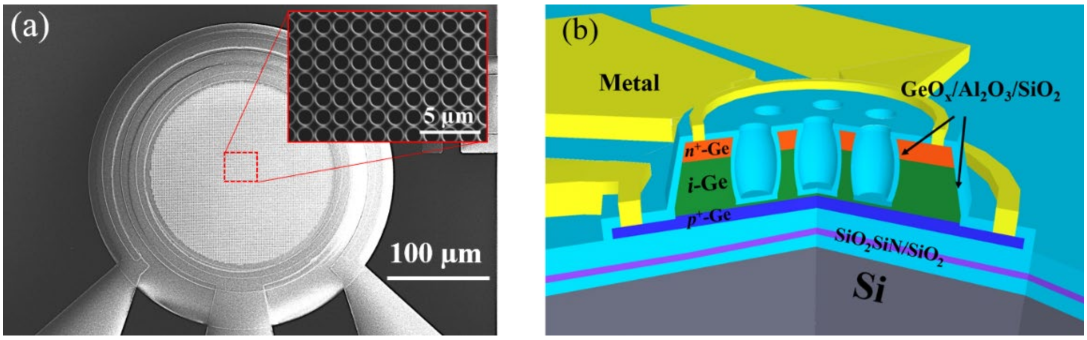

Figure 53. (a) Top SEM view of the hole array photodetector with a 250 µm diameter. Inset in Figure 53(a) shows the zoom-in SEM image of the hole array area. (b) The 3D schematic image of the gourd-shaped hole array photodetector.

Figure 54(a) displays the cross-sectional TEM image of the hole array structures. The hole array structures were patterned with the period and diameter of 1.55 and 1.06 µm, respectively, via the EBL process. The isotropic etching process via ICP-RIE completes the gourd-shaped hole array structures. The upper 600 nm of the epi-Ge layer is only etched away to form the hole array structure to scatter the normal incidence lights. Figure 54(b) displays the cross-sectional high-resolution transmission electron microscopy (HRTEM) image of a hole array that is in the red-squared region in Figure 54(a). The Al_2O_3/GeO_x layers are observed via the HRTEM image, indicating that the O_3 oxidation process provides the sidewall GeO_x formation [91].

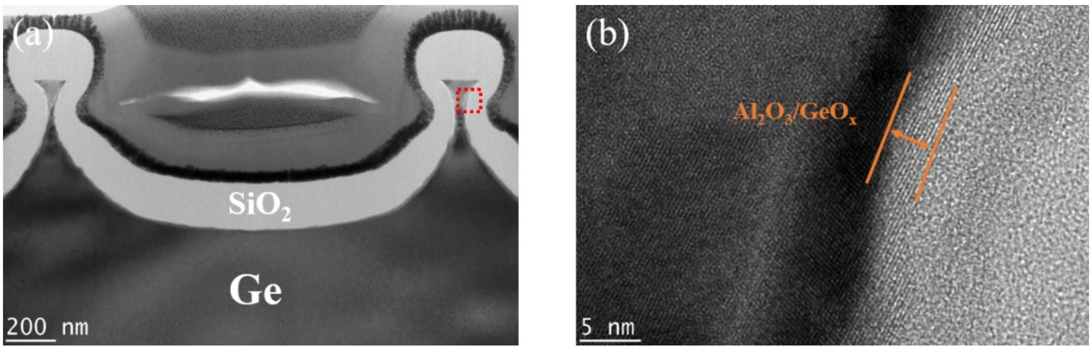

Figure 54. (a) The cross-sectional view of the TEM image of the gourd-shaped hole array structure. (b) The HRTEM image of GeO_x/Al_2O_3 layers for the red-squared region in Figure 54(a).

4.3 Characterizations of Hole-array Ge Photodetectors

The hole array Ge photodiodes are characterized in this section. The dark current analysis will be first discussed in Chapter 4.3.1. Temperature-dependent dark current characteristics are subsequently addressed in Chapter 4.3.2. Next, the optical response and *D** will be mentioned in Chapter. 4.3.3. Last, the 3dB bandwidth will be studied in Chapter 4.3.4.

4.3.1 Dark Current Density Analysis

Mhe micro photon-trapping hole structures increase the dark current for the photodetectors [63]. For the hole array photodetectors, the empty area in the hole region decreases I_{bulk} due to the reduced mesa area. However, I_{surf} increases with the empty area due to the enhanced surface area. The I_{dark} change for a hole array photodetector is associated with *Fill factor* (*FF*). *FF* can be obtained by the equation of *FF=hole area/mesa area* [63]. The demonstrated hole array photodetectors display the *FF* of 6 to 28% with the diameter increasing from 60 to 250 µm. Figure 55 shows the I_{dark}-V curves for the hole array photodetectors in comparison with the hole array-free photodetectors. It should be noted that I_{dark} increases for the hole array photodetectors due to the surface area enhancement. I_{dark} for the hole array photodetectors with the *FF* of 6 to 28% increases by 16 to 61%.

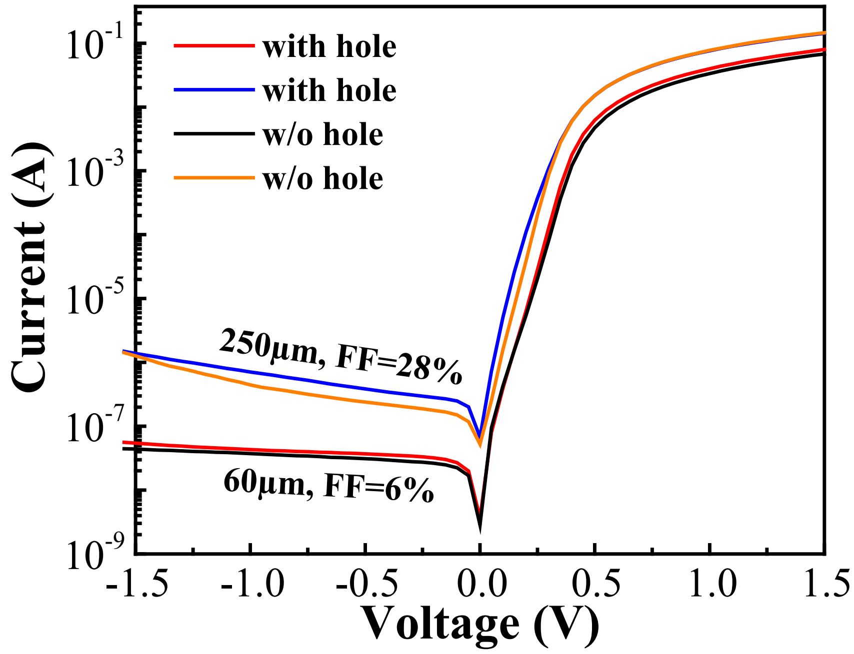

Figure 55. I_{dark}-V characteristics for photodetectors without and with the hole array structures. FF of 6 and 28% corresponds to 60 and 250 μm diameter photodetectors, respectively.

4.3.2 Temperature-dependent Dark Current Study

Temperature-dependent J_{dark}-V characteristics for the hole array and hole array-free photodetectors are obtained in Figure 56(a). J_{dark} for the hole array photodetector was measured to be 1.41 mA/cm^2 at 293 K. J_{dark} for the photodetector with FF of 8% is enhanced by 20%.

The Arrhenius plot for the photodetector was obtained in Figure 56(b). The slopes become flat at high voltage, meaning that I_{dark} is barely affected by the temperature variation. According to Eq. (3), E_a can be extracted. The estimated E_a for the photodetector is displayed in Figure 56(c) along with E_a without the hole array. The E_a variation is larger than the photodetector without the hole array. E_a is high at low voltage, meaning that the dark leakage current is affected by the temperature variation. At high voltage, however, the leakage current is barely changed by the temperature variation. At high voltage, the electric field distribution in epi-Ge is strong, enhancing the TAT leakage process. This TAT process is further improved for the hole array photodetectors at the high reverse voltage.

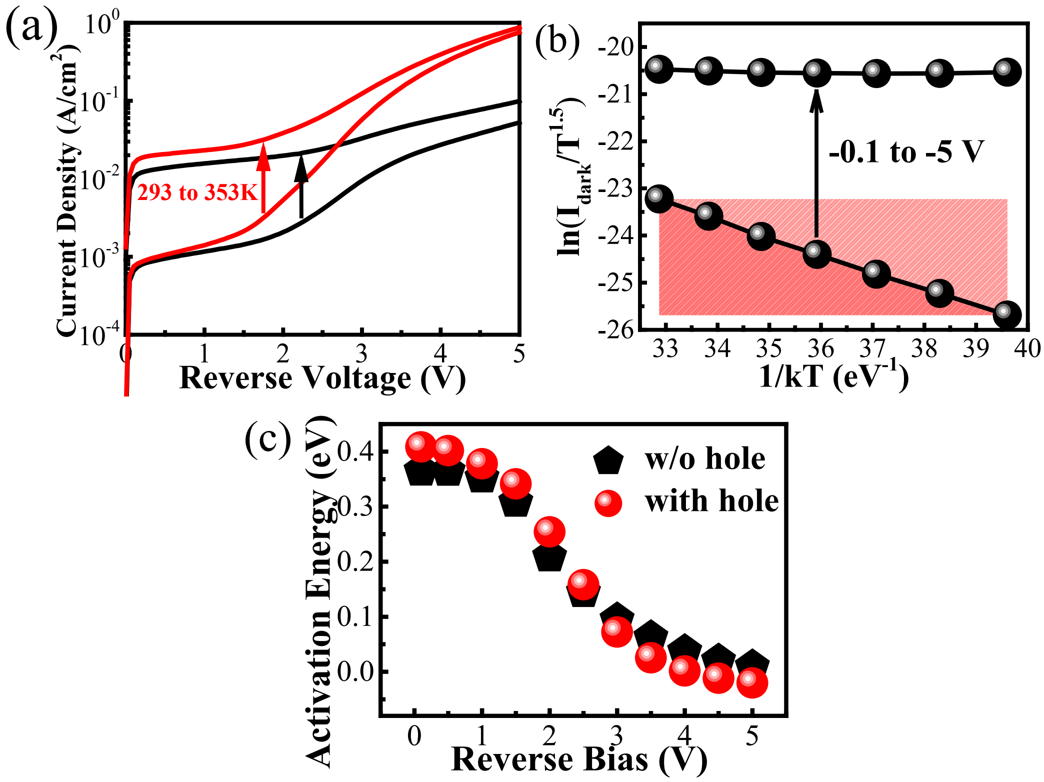

Figure 56. (a) Temperature-dependent I_{dark}-V characteristics for photodetectors without and with the hole array. (b) Arrhenius plot for the hole array photodetector as a function of *1/kT*. The arrow indicates the voltage increase from -0.1 to -5.0 V. (c) E_a for the hole and the hole-free photodetectors as a function of voltage from -0.1 to -5.0 V.

4.3.3 Photocurrent & Specific Detectivity Analysis

The output optical power was calibrated to be 0.4 mW in the wavelength range from 1,500 to 1,630 nm. Figure 57(a) displays I_{photo}-V characteristics for the photodetectors without and with the hole array structures at 1,550 nm. I_{photo} increases for the hole array photodetector due to the light trapping in hole array structures as simulated in Figure 50. The absorption efficiency for a photodetector can be determined by EQE. The following equation can extract EQE,

$$EQE = \frac{hc}{q\lambda}R. \tag{24}$$

Figure 57(b) shows obtained EQE for the hole array photodetectors in different hole diameters and periods at 1,550 nm. EQE for the hole array photodetectors is improved than the photodetector without the hole array. The hole array structure with a 1.55 μm period and a 1.08 μm diameter shows an EQE of 70%, improved by 2.5×.

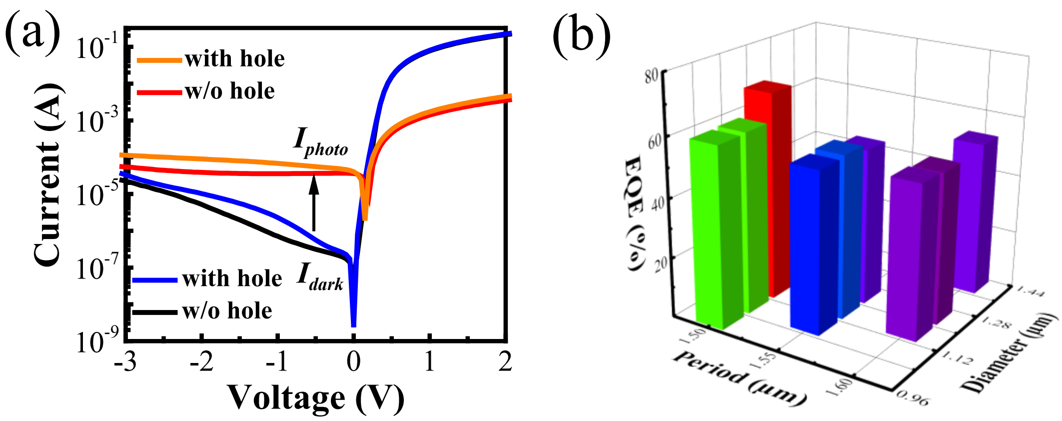

Figure 57. (a) I_{photo}-V characteristics for photodetectors without and with the hole array. The arrow represents the I_{photo} generation under illumination. (b) EQE for hole array Ge photodetectors at 1,550 nm as a function of hole periods and diameters.

Figure 58(a) and (b) displays the responsivity spectra for the hole array photodetector with various diameter and period conditions. Figure 58(a) displays the responsivity spectra for hole array photodetectors with a consistent period of 1.50 μm im comparison with the hole-free photodetector. The responsivity is improved for hole array photodetectors. Among the hole array photodetectors, the cut-off wavelength is extended with the diameter increasing from 1.00 to 1.08 μm. Then, the cut-off wavelength decreases when the diameter size increases from 1.08 to 1.16 μm. Figure 58(b) illustrates the responsivity spectra for hole array photodetectors with a consistent diameter of 1.16 μm. The cut-off wavelength is extended with the period decreasing from 1.60 to 1.55 μm. Where the diameter is 1.16 μm, the measured responsivity was obtained to be 0.74 A/W at 1,550 nm. The cut-off wavelength is reduced with the period decreasing from 1.55 to 1.50 μm. When the period is 1.50 μm, the measured responsivity was obtained to be 0.74 A/W at 1,550 nm. The period variation gives a large variation in the responsivity, meaning that the responsivity is mainly determined by the period condition.

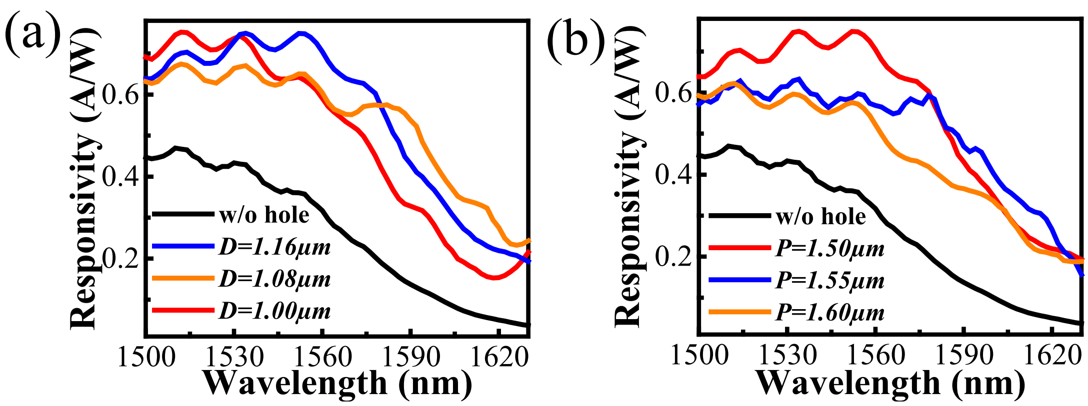

Figure 58. The responsivity spectra for the hole array photodetectors with different (a) diameters from 1.00 to 1.16 μm and (b) periods from 1.50 to 1.60 μm. The responsivity spectra for the hole-free array photodetector are also included.

The reported responsivity for the gourd-shaped hole array photodetector is benchmarked with the responsivities for the reported normal incidence vertical *p-i-n* Ge photodetectors with respect to the dark current density at -1 V in Figure 59. In Figure 59, diverse substrate platforms are proposed for the Ge photodetectors, i.e., Si substrate, SOI, and GOI platforms without and with the hole array. The responsivity for the Ge photodetectors on the Si substrate is improved by increasing the thickness of epi-Ge. However, the high dark current density is huge due to the enhanced SRH and

TAT leakage mechanisms. Also, the thick *i*-Ge layer restricts the 3dB bandwidth. For the photodetectors on SOI or GOI platforms, the responsivity is improved, despite thin *i*-Ge. This is because the insulator substrate provides high optical confinement. Recently, the photon-trapping hole array designs were adopted in the nano-and micro-size hole scales [63]. Since the hole array structure traps the normal incidence lights, the responsivity was improved up to 0.91 A/W. However, the dark current density for such photodetectors is > 20 mA/cm^2. The huge dark current density degrades D^*, which is the key parameter to compare the photodetector performances made by different materials. The demonstrated gourd-shaped hole array photodetectors achieved the ultra-low J_{dark} of ~1mA/cm^2 and improved responsivity of 0.74 A/W [99]. It should be noted that a thin *i*-Ge layer for the hole array photodetector is 288 nm at -1 V.

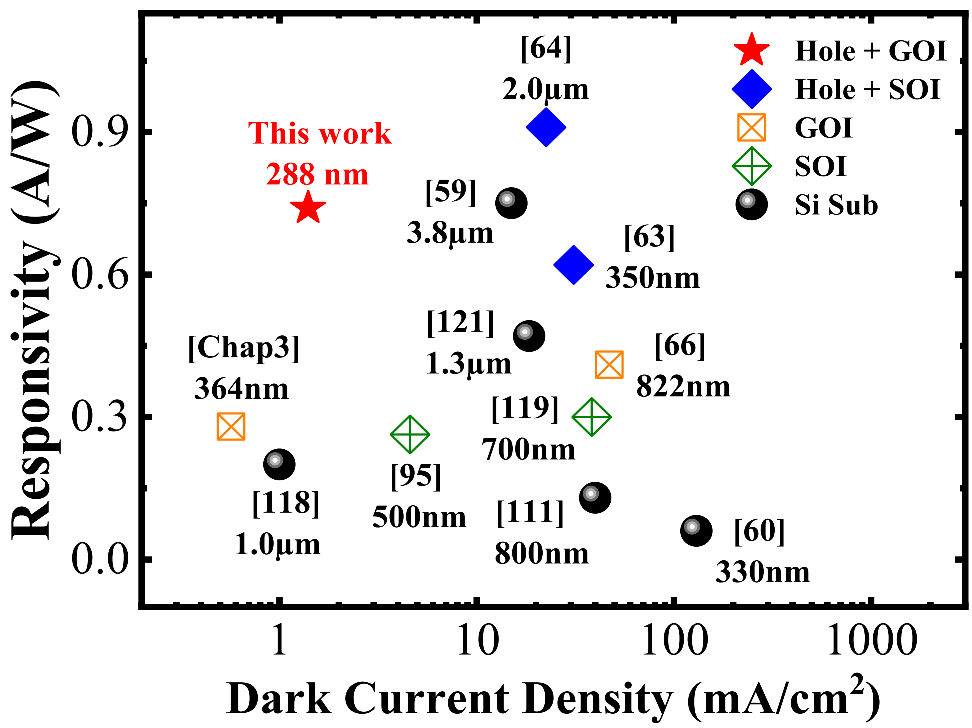

Figure 59. Benchmarking of responsivities for normal incidence epi-Ge vertical photodetectors with respect to dark current density. The photodetectors were demonstrated on diverse platforms, i.e., Si substrate, SOI without and with hole array structures, and GOI without and with hole array [58].

The low leakage current and high responsivity performances for the photodetectors can be expressed by *D**. *D** can be estimated by the following equation [52],

$$D^* = \frac{R\sqrt{A\Delta f}}{I_{rms}} \tag{25}$$

where Δf is the noise bandwidth, and I_{rms} is the root-mean-square noise current. I_{rms} can be obtained by shot noise (I_{shot}) and thermal noise ($I_{thermal}$). I_{rms} for a photodetector can be described by the following equations,

$$I_{rms} = \sqrt{I_{thermal}^2 + I_{shot}^2}, \tag{26}$$

$$I_{thermal} = \sqrt{4kT\Delta f / R_{shunt}}, \tag{27}$$

$$I_{shot} = \sqrt{2eI_{photo}\Delta f}, \tag{28}$$

where R_{shunt} is shunt resistance. Δf is selected to be 1 Hz. R_{shunt} is estimated by extracting the first derivative of V to I_{dark} near 0 V. Estimated R_{shunt} for the photodetectors without and with the hole array is 1.9 and 1.7 MΩ, respectively. Estimated $I_{thermal}$ for photodetectors without and with the hole array structures is 9.3×10^{-14} and 9.8×10^{-14} A/Hz$^{1/2}$, respectively. I_{shot} for photodetectors without and with the hole array is extracted to be 1.38 and 1.39×10^{-13} A/Hz$^{1/2}$, respectively. The calculated *D** for the hole array Ge photodetector is 3.1×10^{10} cm·Hz$^{1/2}$W^{-1} at 1,550 nm. This value is enhanced by ~1.5× in comparison with the hole-free photodetector. The *D** spectra for photodetectors with and without the hole array are illustrated in comparison with the commercial extended-InGaAs/Ge photodetectors in Figure 60 [73]. *D** for the hole array photodetector displays the order of 10^{10} cm·Hz$^{1/2}$W^{-1}

beyond the wavelength of 1,600 nm. Thanks to the cut-off wavelength extension, it is worth noting that D* for the hole array photodetector is improved by 10× at 1,600 nm.

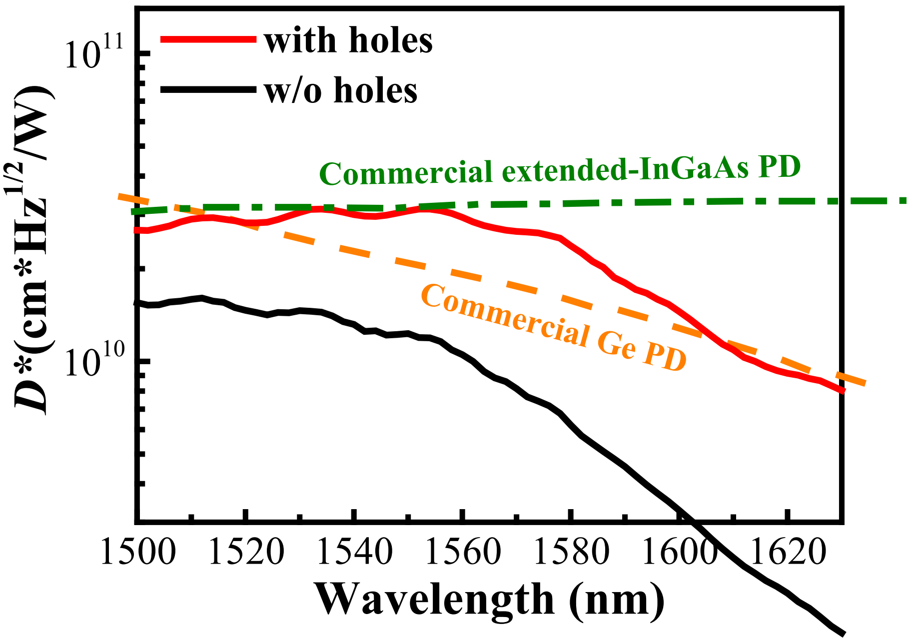

Figure 60. The specific detectivity D* spectrum of the gourd-shaped hole array vertical p-i-n photodetector with respect to the wavelength from 1,500 to 1,630 nm in comparison with the hole-free array Ge photodetector at a reverse bias of -1 V. D* for commercial Ge and extended-InGaAs photodetectors also displays as references [53].

4.3.4 Frequency Response

The frequency response for the hole array photodetector was implemented in Figure 61(a) at 1,550 nm. The 3dB bandwidth for the hole array photodetector was 500 MHz at -5 V. This is enhanced by ~10% in comparison with the hole-free photodetector [78]. The voltage-dependent 3dB bandwidth is shown in Figure 61(b) for the photodetectors with different diameters of mesa sizes. A noticeable difference appears between them at high voltage beyond -1 V. The 3 dB bandwidth is enhanced as the mesa diameter decreases, indicating that the RC-limited delay determines the 3dB bandwidth mainly.

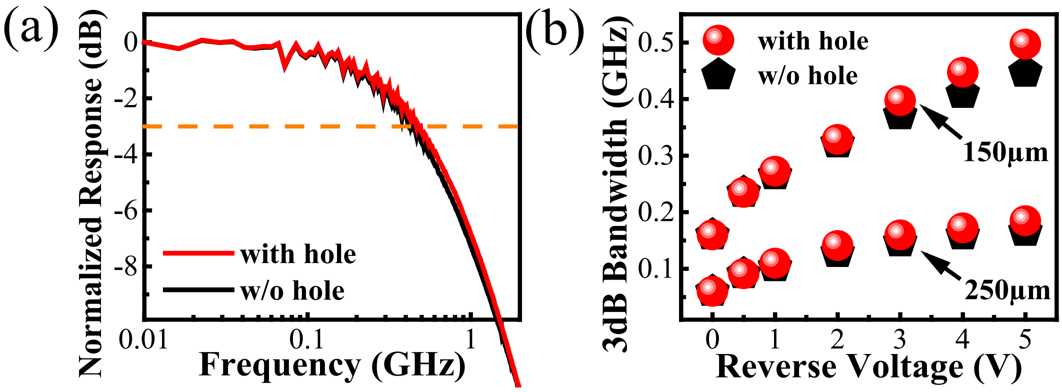

Figure 61. (a) Frequency response for photodetectors without and with the hole array at 1,550 nm. (b) The 3dB bandwidth for photodetectors without and with the hole array as a function of voltage from 0 to -5 V.

Figure 62(a) displays the C-V characteristics for photodetectors without and with the hole arrays. There is no noticeable difference between them where the voltage is low. Where the voltage is high, the capacitances are distinguishable between photodetectors without and with the hole array. The inset in Figure 62(b) displays capacitances with respect to the photodetector mesa areas. W_d increases from 150 to 600 nm with the voltage from 0 to -5 V. C_j can be divided into hole-free area junction capacitance ($C_{j,no\text{-}hole}$) and hole area junction capacitance ($C_{j,hole}$) as shown in the inset in Figure 62(a). Where the voltage is low, $C_{j,no\text{-}hole}$ doesn't significantly contribute to C_j. However, $C_{j,no\text{-}hole}$ contributes to C_j where the voltage is high. Therefore, the total junction capacitance decreases, enhancing the 3dB bandwidth when the reverse bias voltage is high. It is worth noting that the reduction in the mesa sizes for the hole array photodetectors can theoretically enhance the 3dB bandwidth due to the low RC-limited bandwidth, as expected in Chapter 3.

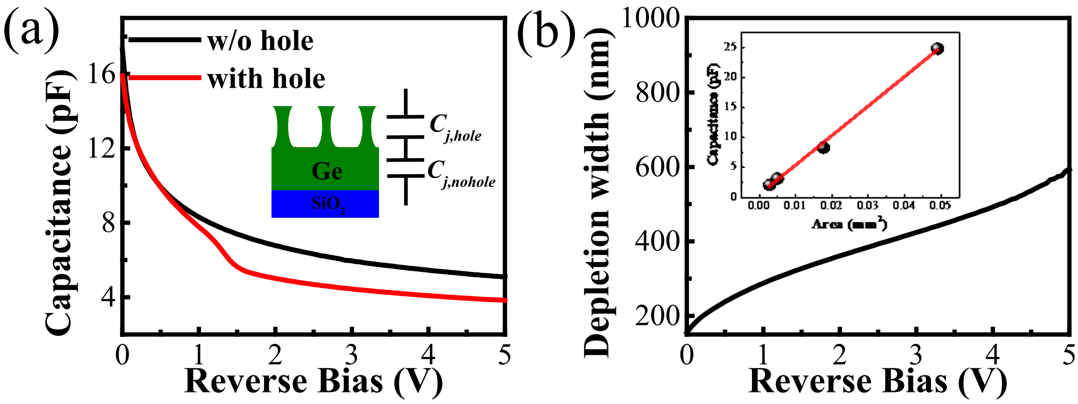

Figure 62. (a) *C-V* characteristics for photodetectors without and with the hole array as a function of voltage from 0 to -5 V. The inset in Figure 62(a) displays the cross-sectional schematic image of the hole array structure and the corresponding capacitance components. (b) Extracted W_d as a function of reverse bias. Inset displays the capacitance with varying mesa areas at -1 V.

4.4 Summary

The gourd-shaped hole array vertical *p-i-n* photodiodes on the low TDD GOI platform with GeO_x passivation were demonstrated in Chapter 4. The optimized hole array structures were obtained through the FDTD simulation study. It is simulated that the gourd-shaped hole array structures provide improved absorption spectra in comparison with the cylinder-shaped hole array structures. The responsivity for the hole array photodetector was 0.74 A/W at 1,550 nm. The two approaches improved the responsivity; i) the low TDD GOI platform and ii) the groud-shaped hole array structures. *D** for the hole array photodetectors was estimated to be 3.1 × 10^{10} cm·$Hz^{1/2}W^{-1}$ at 1,550 nm. This value is superior to the commercial Ge bulk photodiodes. The frequency response experiment revealed that the hole array structures improved the 3dB bandwidth by 10% due to low capacitance. The gourd-shaped vertical p-i-n photodiodes on low TDD GOI with GeO_x passivation are promising for CMOS-compatible and low-cost photodetectors for Si-based PICs, comparable with the commercial extended-InGaAs photodiodes.

Chapter 5: Trap-related Photoexcited Carrier Dynamics in GeSn Films toward Efficient Mid-infrared Range Photodetection

In this chapter, alloying Sn with Ge will be addressed for MIR range photodetection. A systematic study on the cut-off wavelength extension and carrier dynamics related to defects in GeSn will be conducted. In Chapter 5.1, GeSn photodetectors and their dependence on defects will be introduced. Chapter 5.2 describes the characterization of GeSn films and photoconductors with varying Sn contents. Chapter 5 will be summarized in Chapter 5.3. Chapter 5 aims to provide the ways toward high-efficiency MIR range photodetection.

5.1 GeSn Photodetectors for MIR Range Photodetection

A Ge photodetector has mainly been developed for NIR range photodetection. Although strain engineering has been employed for the cut-off wavelength extention [67], the MIR range photodetection beyond 2,000 nm is still challenging. Alternatively, alloying Sn with Ge fascinates for long wavelength photodetection. GeSn bandgap shrinks as Sn content increases. This leads to a tunable band structure in changing Sn content [61]. Therefore, tremendous efforts have been made for photodetectors using GeSn alloys.

The main interest of 2,000 nm photodetection was achieved for GeSn photodetectors with the Sn content of 6% [71]. Moreover, since *Γ* valley in a conduction band shrinks faster than *L* valley in a conduction band, strain-free GeSn films with Sn content of above 8% were suggested for a monolithic light source, which could open up the new scheme for Si-based PICs [127]. However, the plenty of defects in GeSn degrades its performance.

Epitaxial GeSn growth has been developed via CVD, MBE, magnetron sputtering, laser annealing, etc., for high-quality GeSn films and high Sn content. However, many dislocations/defects are generated in GeSn films due to i) low solubility of Sn into Ge (~1%), ii) low-temperature growth, and iii) the lattice mismatch between GeSn/Ge/Si. Numerous defects serve as trap states in GeSn, limiting optical and electrical performances of GeSn-based devices. For instance, poor-quality GeSn causes i) high dark leakage current and ii) low optical responsivity for a GeSn photodetector.

5.1.1 Dark Current Generation Related to Dislocations and Defects in GeSn

The dark current for defect-free GeSn photodetectors is governed by a diffusion current mechanism. Guo-En Chang *et al.* reported that the calculated dark current density for defect-free GeSn photodetectors with a Sn content of < 10% is <1mA/cm^2 [68]. Since SRH centers do not exist at defect-free GeSn, only BTBT and diffusion leakage current mechanisms are considered as the primary leakage current mechanisms. At low reverse bias voltage, the electric field intensity is not sufficient to cause band tunneling, meaning that only the diffusion leakage current mechanism plays a main role for the dark current generation. J_{diff} consists of J_{diff} in the direct (Γ)-conduction band (J^{Γ}_{diff}), J_{diff} in the indirect (L)-conduction band (J^{L}_{diff}), and J_{diff} in the valence bands (J^{h}_{diff}). J_{dark} for defect-free GeSn photodetectors can be calculated by summing up the J_{diff} components and they are shown in Figure 63(a)-(d). Figure 63(a)-(c) represent J_{dark} for defect-free GeSn photodetectors with different Sn contents of 2, 6, and 10%, respectively. It should be noted that leakage current increases with Sn contents due to GeSn bandgap narrowing. Figure 63(d) summarizes J_{dark} for photodetectors with respect to Sn contents. J^{Γ}_{diff} increases faster than other components because of high electron mobility and fast bandgap decrease with increasing Sn content.

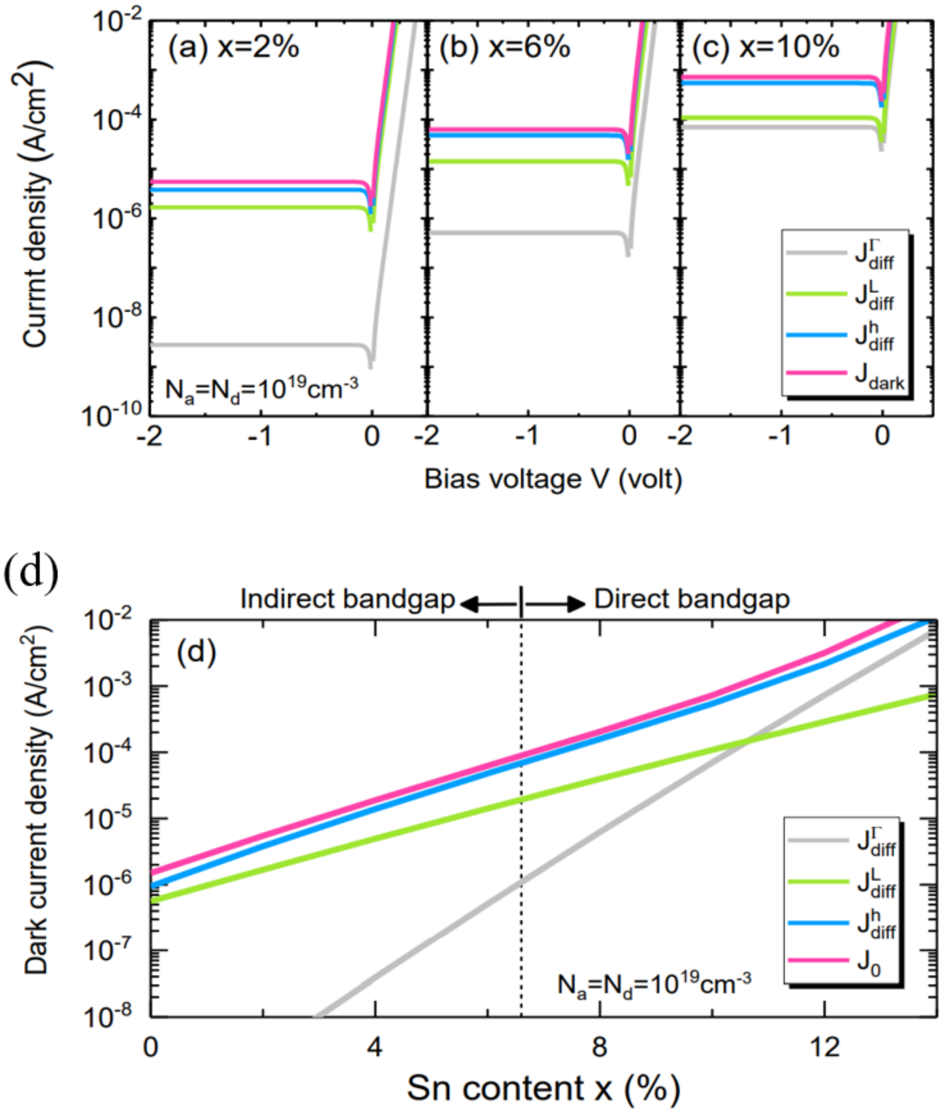

Figure 63. The calculated J_{dark}-V curves for defect-free p-i-n GeSn photodetectors with different Sn contents of (a) 2%, (b) 6%, and (c) 10%. Γ and L-valleys in conduction bands and valence bands are considered for the diffusion current calculation [68]. (d) J_{dark} for defect-free GeSn photodetectors with respect to Sn content [68].

Experimentally, however, it has been reported that demonstrated vertical *p-i-n* GeSn photodetectors displayed a huge dark current. In addition, the dark current for GeSn photodetectors increases with Sn contents [128]. Figure 64(a) and (b) display the cross-sectional view of a GeSn photodetector and J_{dark}-V curves with varying Sn contents, respectively. J_{dark} increases with Sn contents. An increase in J_{dark} is attributed to a shrinkable of a GeSn bandgap and increased dislocations/defects in GeSn. A E_a study can tell which process is dominant for the huge leakage current. Since a narrow GeSn bandgap improves thermal-excited EHPs, this could enhance the E_a up to the material bandgap. However, according to temperature-dependent *I-V* characteristics in Figure 64(c) and (d), The E_a of GeSn photodetectors was below the half of a material bandgap, signifying that the dark current for a GeSn photodetector is governed by trap-related leakage current mechanisms.

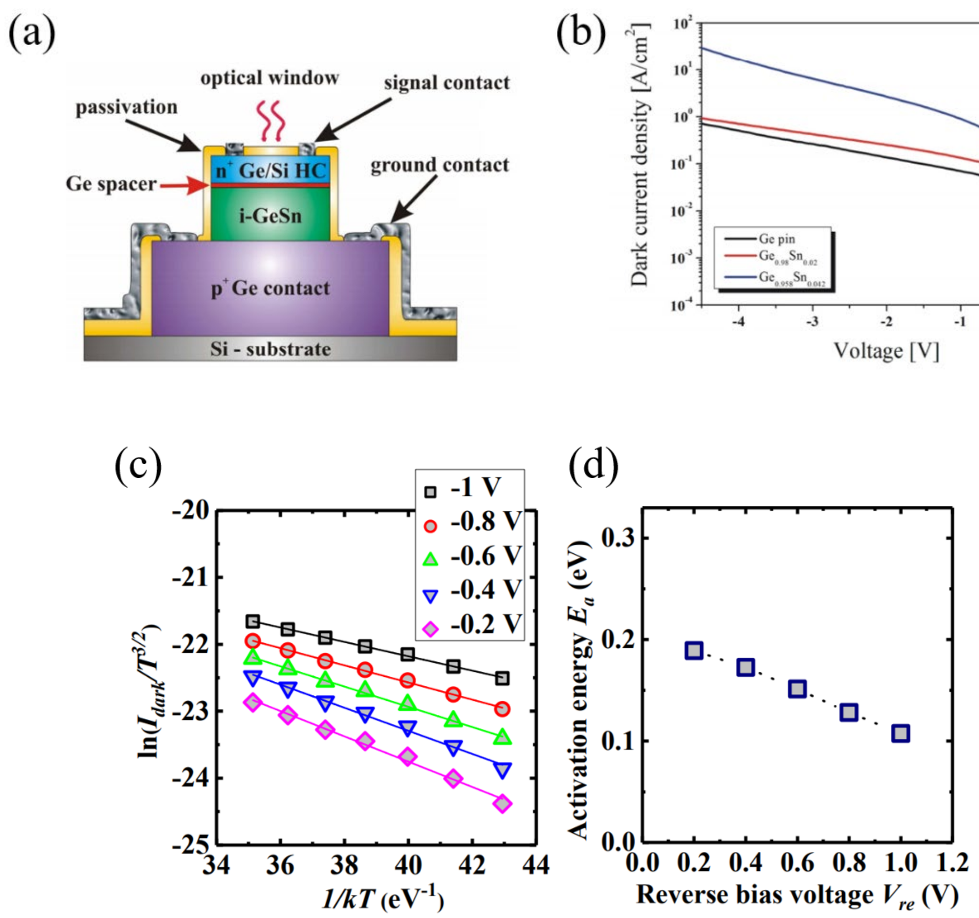

Figure 64. (a) Cross-sectional schematic image of the GeSn photodetector [128]. (b) the I-V characteristics for GeSn photodetectors with varying Sn contents [128]. (c) The Arrhenius plots for the lateral GeSn p-i-n photodetectors as a function of 1/kT [129]. (d) Extracted Ea from the linear fitting in Figure 64(c) [129].

Recent GeSn optical components, therefore, have been discovered by mitigating defect-related carrier dynamics. Several methods have been introduced to manage defects/dislocations, e.g., the removal of a defective layer, step graded GeSn growth, and post-thermal annealing process [130]. Successful defect management represented a reduction in optical threshold current by ~10× for lasing [133]. In addition, Si layer passivation was introduced to improve surface quality, reducing dark current density by ~100× [74]. Therefore, a systematic study on a dark current associated with dislocations/defects should be implemented to achieve low leakage current GeSn photodetectors.

5.1.2 Degradation on Optical Responsivity Related to Defects in GeSn

The optical responsivity for defect-free GeSn photodetectors with an intrinsic region thickness of 3,000 nm was estimated in Figure 65(a). The cut-off wavelength is extended with increasing Sn contents due to a narrowing GeSn bandgap. Also, responsivity increases with Sn content due to enhanced GeSn absorption coefficient. In practical, The cut-off wavelength is extended with increasing Sn contents. However, the responsivity for demonstrated GeSn photodetectors is not improved with different Sn contents. Also, the responsivity for GeSn photodetectors decreases with wavelength. Although absorption coefficient extracted via Ellipsometry increases with Sn contents [17], it does not directly improve responsivity. This could probably be due to many dislocations/defects in GeSn or a GeSn/Ge/Si interface. An increase in defect density results in a fast non-radiative recombination process via trap states so that photoexcited carriers are recombined before reaching electrodes.

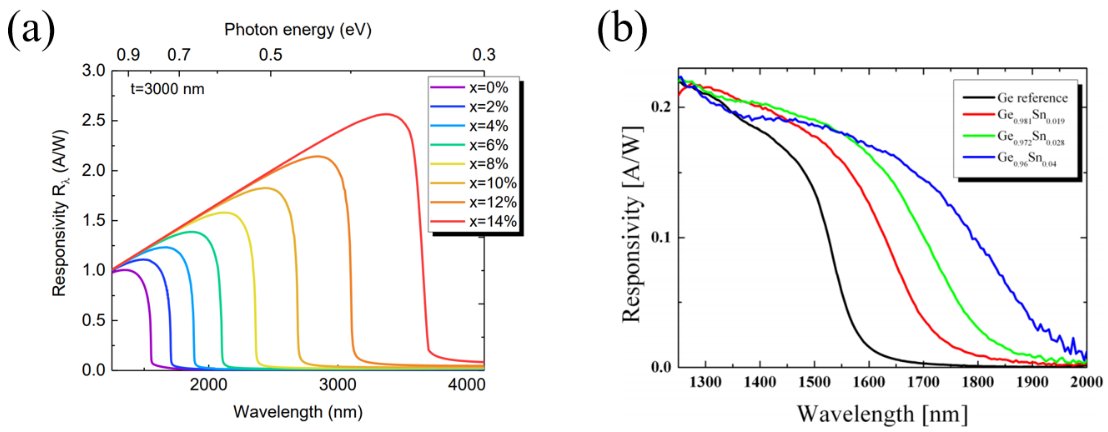

Figure 65. (a) The calculated responsivities for GeSn *p-i-n* photodetectors as a function of wavelength [68]. (b) the I_{photo}-V characteristics for GeSn photodetectors with varying Sn contents [134].

5.2 Carrier Dynamics Related to Defects in GeSn Photoconductors

In this section, carrier dynamics in GeSn films will be investigated. GeSn films are prepared with different Sn contents from 3.0 to 7.1% and different thicknesses from 180 to 900 nm. GeSn films are then fabricated for photoconductors with interdigitated electrodes. Dark current analysis is performed in Chapter 5.2.2. Chapter 5.2.3 addresses a photocurrent transient study for GeSn photoconductors. EQE spectra are extracted and are compared with simulated absorption spectra via FDTD simulation in Chapter 5.2.4. Chapter 5.2.5 will introduce a comparison between PL and photoconductivity (PC) spectra.

5.2.1 GeSn Growth and their Characterization

A Ge strain-relaxation buffer layer was grown on a 6-inch Si wafer and the thickness of a Ge buffer layer is 900 nm. Subsequently, epitaxial GeSn films were grown on a Ge buffer layer using $SnCl_4$ and Ge_2H_6 in H_2 carrier gas via a reduced pressure chemical vapor deposition (RPCVD) reactor. In order to grow GeSn with the Sn content of above Sn solubility, low-temperature growth was adopted with temperature below 400°C. GeSn wafers were grown with different Sn contents and different thicknesses, named Sample A, B, C, and D. Sample A and B were grown using the same recipe, but only increases growth time to obtain a thick GeSn film for Sample B. Also, Sample C and D were grown by the same recipe, but only increases growth time to obtain a thick GeSn film for Sample D.

Figure 66(a) shows the SIMS analysis of Sample A and B to verify Sn content and the depth of as-grown GeSn films. GeSn thicknesses are estimated to be 180 nm and 900 nm for Sample A and B, respectively. Thick GeSn thickness is achieved by increasing growth time. And Sn content is the same for Sample A and B. Figure 66(b) displays HRXRD curves in (004) 2θ-ω direction for Sample A-D. Peaks at around 66.1 and 69.0° represent a Ge buffer layer and a Si substrate, respectively. As-grown GeSn peaks are observed below 65.99°. GeSn curves for Sample A and B are symmetric. Also, a GeSn peak position is consistent although the thickness is different. In contrast, a GeSn curve for Sample D is asymmetric, and a GeSn peak shifts in comparison with Sample B. This results from that a gradient GeSn layer was grown in the bottom. Subsequently, a higher Sn content layer is grown on top spontaneously. This originates from the fact that a bottom GeSn layer with a large lattice constant allows growing a top GeSn layer with high Sn content on top.

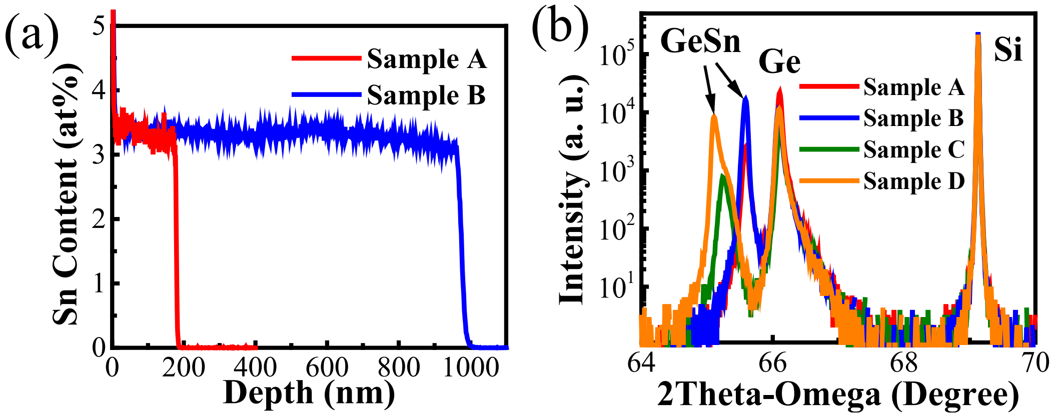

Figure 66. (a) SIMS profiles for Sn content of Sample A and B. (b) HRXRD curves in 2θ-ω orientation for Sample A to D.

RSM images in (224) direction for Sample A-D are shown in Figure 67(a)-(d), respectively. The (Q_x, Q_z) coordination can determine in-plane lattice constant ($a^{\parallel}$) and out-plane lattice constant ($a^{\perp}$) by the following equations,

$$Q_x = \frac{2\sqrt{2}}{a^{\parallel}} \times 1000, \tag{29}$$

$$Q_z = \frac{4}{a^{\perp}} \times 1000. \tag{30}$$

Taking accout into the Vegard's law to determine GeSn lattice constant and tetragonal deformation of GeSn lattice, Sn content and its strain value can be extracted by the following equations [130],

$$a^0_{GeSn} = xa^0_{Sn} + (1-x)a^0_{Ge} + x(1-x)b_{GeSn}, \tag{31}$$

$$a_{GeSn} = \frac{1-\nu_{GeSn}}{1+\nu_{GeSn}} a^{\perp}_{Gesn} + \frac{2\nu_{GeSn}}{1+\nu_{GeSn}} a^{\parallel}_{GeSn}, \tag{32}$$

$$\nu_{GeSn} = x\nu_{Sn} + (1-x)\nu_{Ge}, \tag{33}$$

where a^0_{GeSn}, x, a^0_{Sn}, a^0_{Ge}, and b_{GeSn} are GeSn lattice constant, Sn content, Sn lattice constant (a^0_{Sn} = 0.6489 nm), Ge lattice constant (a^0_{Ge} = 0.5648 nm), and a bow parameter (b_{GeSn} = 0.0041 nm), respectively. And v_{GeSn}, v_{Ge}, and v_{Sn} are the poison's ratio of GeSn, Ge (v_{Ge} = 0.271), and Sn (v_{Sn} = 0.360), respectively. The estimated Sn content and strain values are shown in Table 2. GeSn layers for Sample A-D are under compressive strain while Ge buffer layers are under tensile strain. The compressive strain in GeSn results from the large lattice mismatch between GeSn/Ge.

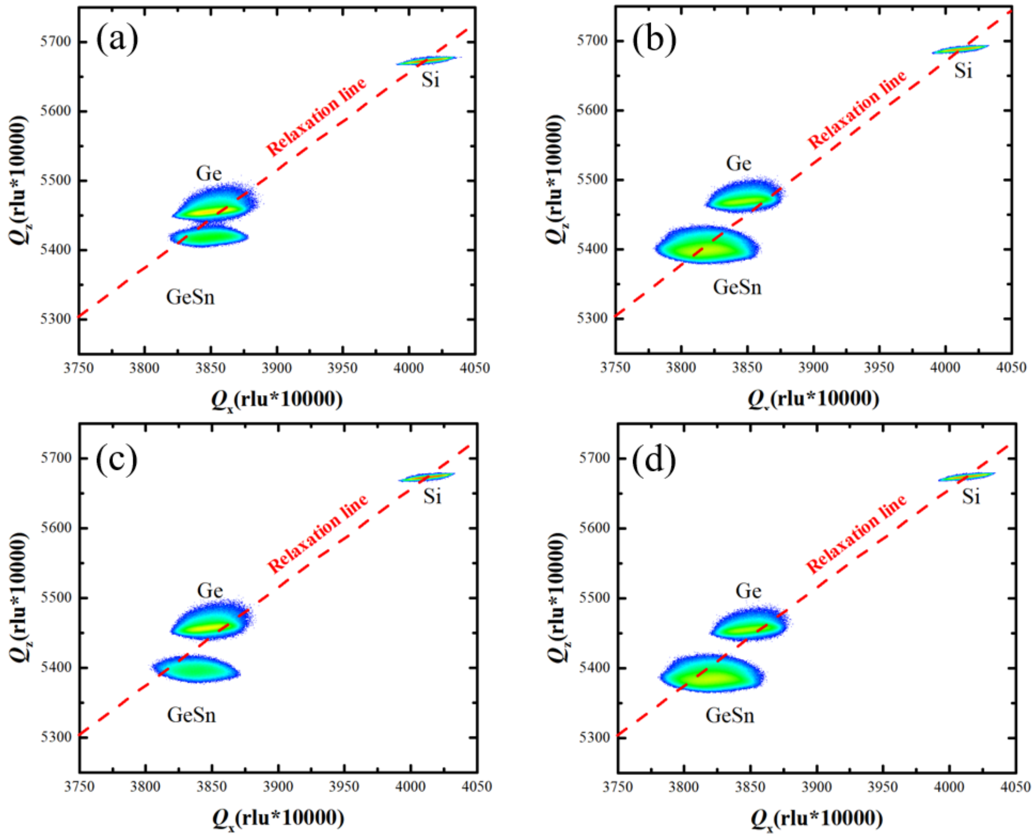

Figure 67. Reciprocal space map (224) images of (a) Sample A, (b) Sample B, (c) Sample C, and (d) Sample D.

Sample Name	Sn Content (%)	Strain (%)	Sample Feature
Sample A	3.0	-0.21	Thin GeSn
Sample B	3.4	-0.09	Thick GeSn
Sample C	5.0	-0.32	Thin GeSn

Sample D	7.1	-0.16	Thick GeSn

Table 2. Sn contents and strain information for Sample A, B, C, and D extracted from RSM analysis.

A cross-sectional TEM image for Sample A is displayed in Figure 68(a). Dislocations are observed at a GeSn/Ge interface. Flat dislocations are also observed in the HRTEM image in Figure 68(b) [127]. The zoom-in HRTEM image in Figure 68(c) shows lattice fringes near the interface [137]. It is worth noting that many dislocations/defects are observed near a GeSn/Ge interface.

Photoconductors were fabricated using Sample A-D. Interdigitated electrodes of Ti 20nm/Al 400nm were deposited by sputtering, followed by the lift-off process. The spacing between electrodes and the width of each electrode are 16 and 8 μm, respectively. The 3D schematic image for a GeSn photoconductor is displayed in Figure 68(d). The top SEM view for a GeSn photoconductor is displayed in Figure 68(e).

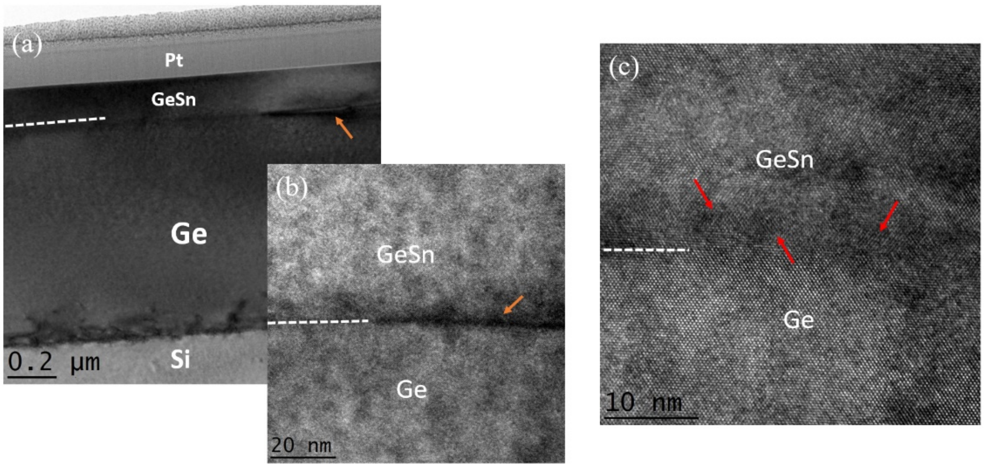

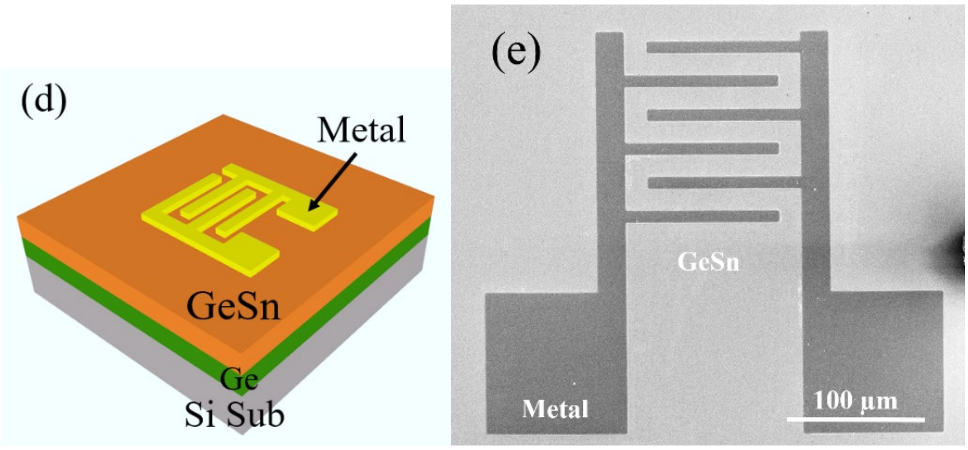

Figure 68. (a) Cross-sectional TEM image of Sample A with the GeSn/Ge interface (indicated by the orange arrow). (b) High-resolution TEM image of Sample A with dislocation (indicated by the orange arrow). (c) High-resolution TEM image of Sample A interface with the lattice fringes (indicated by the red arrows). (d) The 3D schematic image of GeSn photoconductors. (e) Top-view of the SEM image for the photoconductor.

5.2.2 Dark Current Analysis

I_{dark}-V curves for Sample A and B photoconductors are measured in Figure 69(a). Equivalent both electrode conditions cause symmetric I-V characteristics in positive and negative voltage ranges. I_{dark} for Sample A and B shows linear and non-linear shapes, respectively. It is worth noting that I_{dark} for Sample B is lower than the one for Sample A despite thick *i*-GeSn. Figure 69(b) represents I_{dark}-V characteristics for Sample C and D photoconductors. I_{dark} for Sample C and D shows linear and non-linear shapes of the *I*-*V* curves, respectively. It is worth noting that I_{dark} for the Sample D photoconductor is close to the one for the Sample C photoconductor although Sn content is high and the GeSn film is thick. Thin GeSn photoconductors (Sample A and C) display linear I_{dark} while thick GeSn photoconductors display non-linear I_{dark}. When voltage is applied, the electric field is formed between electrodes, and electric field intensity is decayed as depth deeper [138]. The low I_{dark} for thin

GeSn photoconductors (Sample B and D) could probably result from electric field distributed far away from a GeSn/Ge interface.

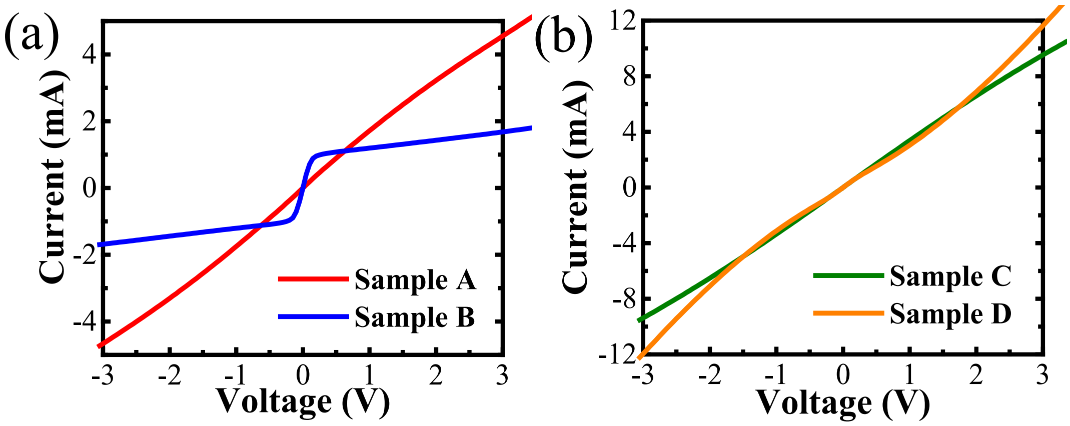

Figure 69. Idark-V curves for (a) Sample A and B and (b) Sample C and D photoconductors.

Temperature-dependent I_{dark}-V characteristics for Sample A and B were obtained in Figure 70(a). I_{dark} for the Sample A photoconductor is not sensitive to temperature change. In contrast, I_{dark} for the Sample B photoconductor increases with temperature. Figure 70(b) displays temperature-dependent I_{dark}-V curves for Sample C and D photoconductors. I_{dark} for Sample C is almost constant in the measured temperature range, while I_{dark} for Sample D changes in temperature variation. A dark current is mainly attributed to thermionic emission, the tunneling of minority carriers via trap states. The generation of minority carriers via the thermionic emission process causes dark current variation in different temperature [139]. In contrast, tunneling or TAT leakage currents are insensitive to temperature variation [140]. Thus, I_{dark} for thick GeSn photoconductors (Sample B and D) is affected by a thermionic emission process while I_{dark} for thin GeSn photoconductors (Sample A and C) are not sensitive to temperature change due to improved tunneling and TAT leakage processes.

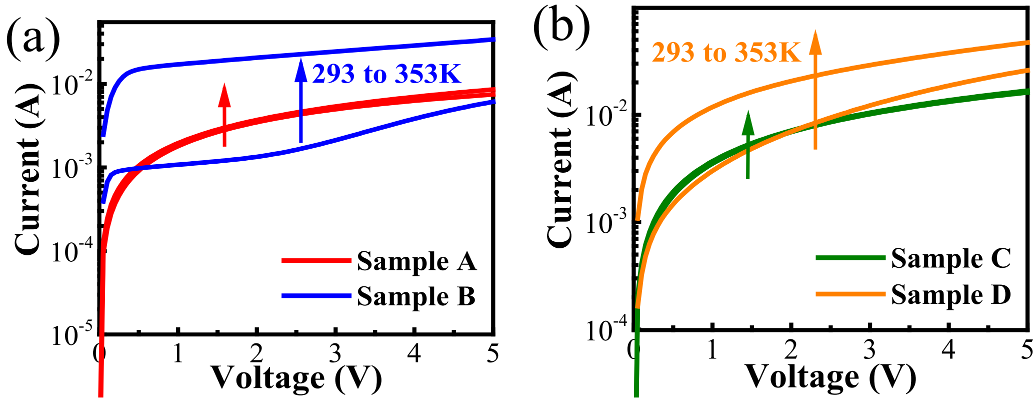

Figure 70. Temperature-dependent Idark-V curves for (a) Sample A and B, and (b) Sample C and D photoconductors. The arrows indicate a temperature increase from 293 to 353 K.

Figure 71(a) displays Arrhenius plots for Sample A and B photoconductors as a function of *1/kT*. The leakage current of a Schottky diode is mainly attributed to the thermionic emission process over the Schottky Barrier Height (SBH). SBH for GeSn/metal can be estimated by the following equations,

$$I_{dark} = I_0\, exp\left(\frac{qV}{n_{ideal}kT}\right)\left[1 - exp\left(-\frac{qV}{kT}\right)\right], \tag{34}$$

$$I_0 = CA^{*}T^2\, exp\left(\frac{q\phi_b}{kT}\right), \tag{35}$$

where I_0 is saturation current, and n_{ideal} is the ideal factor. A^* and ϕ_b are the Richardson constant for GeSn, and SBH, respectively. The Sample B photoconductor shows ϕ_b of 0.37 eV. In contrast, the Sample A photoconductor displays ϕ_b of -0.04 eV. ϕ_b for the Sample B photoconductor is higher than the Sample A photoconductor. Figure 71(b) shows Arrhenius plots for Sample C and D photoconductors. The extracted ϕ_b for Sample D is 0.14 eV while ϕ_b for Sample C is -0.04 eV. High ϕ_b for Sample B and D could result from the dominant thermionic emission process. Where ϕ_b is close to 0 eV, dark current generation is governed by trap-related leakage current mechanisms, such as two-step TAT or variable-range-hopping (VRH) conduction [141].

The two-step TAT is a mechanism where electrons/holes in metal are thermally excited to trap states and pass through a Schottky barrier to reach valence/conduction bands. This mechanism is described by the equation of $exp(-E_a/kT)$, where E_a is the energy difference between trap states and Fermi level. The VRH process is a mechanism where electrons/holes in metal reach defect states associated with a dislocation/defect, and they pass through GeSn by hopping conduction. For thin GeSn photoconductors (Sample A and C), the defective area near the GeSn/Ge interface improves two-step TAT and VRH mechanisms, resulting in ϕ_b of -0.04 eV for the Sample A and C photoconductors. When GeSn is thick (Sample B and D), ϕ_b is higher than -0.04 eV originated from the improvement of thermionic emission. ϕ_b of 0.37 eV for Sample B is low comparing with ϕ_b of 0.14 eV for Sample D. This is because that the number of many defects/dislocations in GeSn increases with Sn content, reducing low ϕ_b [135].

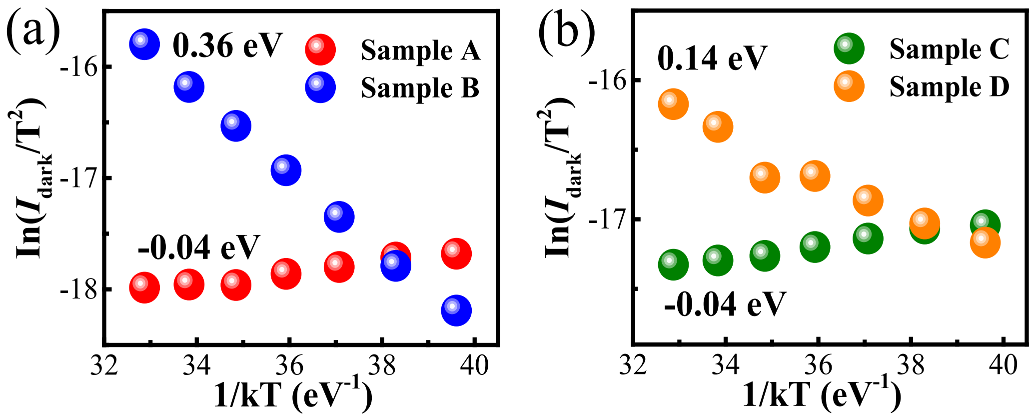

Figure 71. Arrhenius plots for (a) Sample A and B and (b) Sample C and D photoconductors as a function of *1/kT*.

5.2.3 Photocurrent Transient Study

Figure 72(a)-(d) displays photocurrent transients for Sample A-D photoconductors. When the light is on, electron-hole pairs (EHPs) are generated in an absorbing layer and the generated EHPs are collected via electrodes, generating I_{photo}. Figure 72(a) shows the photon transient characteristic for the Sample A photoconductor. Under normal incidence illumination, I_{photo} is generated, resulting in peak I_{photo}. After that, I_{photo} decreases until I_{photo} reaches to steady-state I_{photo}. When the light is off, I_{dark} falls down to steady-state I_{dark} and increases gradually to steady-state I_{dark}.

The valley I_{dark} and peak I_{photo}, named “overshot,” have been addressed in photodiodes made by thin-film polymer solar cells and organic semiconductors [142]. The peak I_{photo} is observed due to typically many dislocations/defects at surface/interface/spacing charge regions [145]. For GeSn photoconductors, trap states near an interface are filled up with photoexcited carriers, resulting in charging/recombination processes. Carrier transit time is much shorter than the charging/recombination processes at interface/surface areas. Thus, the overshot I_{photo} is observed, and subsequently, I_{photo} decreases until reaching steady-state I_{photo} due to the dominant charging/recombination processes [146]. When the light is off, I_{dark} falls down below the steady-state I_{dark}, and the charged/recombined carriers are discharged, increasing valley I_{dark} to steady-state I_{dark}. I_{photo} for Sample A decreases down to 70% of the I_{photo} peak. In other words, photoexcited EHPs are charged/recombined at trap states in the portion of 30%. In contrast, the overshot I_{photo} disappears for Sample B in Figure 72(b), showing the box shape of photocurrent transient. This is because the increase in GeSn thickness suppresses the overshot effect.

Figure 72(c) displays the photocurrent transient for the Sample C photoconductor. The overshot I_{photo} is barely observed. When the light is off I_{dark} gradually decreases, not causing the valley I_{dark}. This means that the charging/recombination processes are barely observed. Where Sn content is high, numerous dislocations/defects are generated during GeSn growth. Thus, the different types of trap states exist at various trap energy levels in GeSn bulk so that the interface-related photoresponse is relatively suppressed [147]. Second, radiative emission and absorption via a band-edge are improved for GeSn with high Sn content since the *Γ* conduction band decreases faster than the *L* conduction band. As a result, thin GeSn photoconductors with high Sn content are not mainly affected by interface defect-related photo-response.

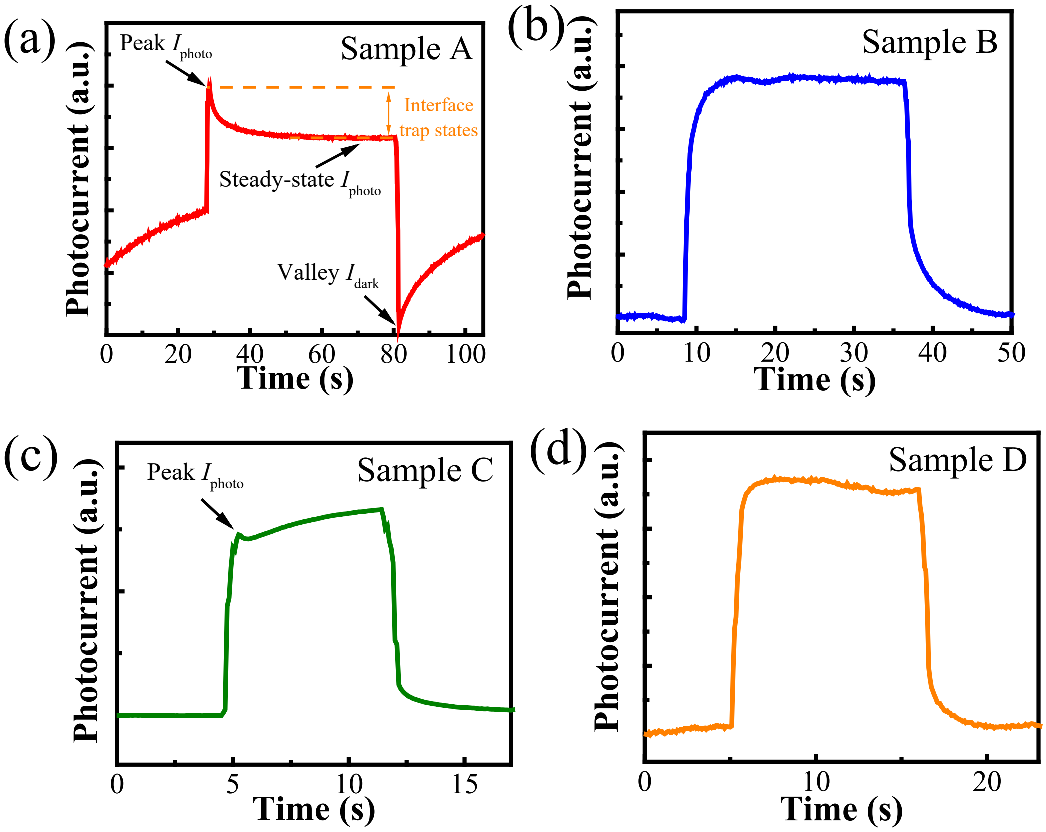

Figure 72. Photocurrent transients for (a) Sample A, (b) Sample B, (c) Sample C, and (d) Sample D photoconductors at 1V.

5.2.4 Optical Absorption and EQE Spectra

To study carrier collection efficiency, optical absorption spectra are compared with EQE spectra. *n* and *k* indies were obtained via Ellipsometry. The absorption spectra were calculated via FDTD simulation. The simulated structure is GeSn/Ge (900nm)/Si Sub. The absorption spectra for Sample A and B were shown in Figure 73(a). The absorption spectra for Sample B are higher than Sample A because the optical penetration depth is deep.

The EQE spectra for Sample A and B photoconductors were compared in Figure 73(b). The cut-off wavelength was measured to be 1,900 nm wavelength. It is worth noting that EQE for Sample B is significantly improved compared with Sample A. At 1,400 nm, EQE for Sample A is below 10%, but EQE for Sample B is 80% at 1,400 nm. The EQE enhancement between Sample A and B is larger than the estimated gap via the simulation in Figure 73(a). This is because photoexcited carriers are captured at trap states near the GeSn/Ge interface, degrading EQE. By increasing GeSn thickness, the overshot I_{photo} is effectively alleviated. As a result, EQE for Sample B is improved by 10× at 1,400 nm.

Figure 73(c) displays the EQE spectra for Sample C and D. EQE spectra is enhanced in comparison with the Sample A photoconductor. This is because the charging/recombination processes are suppressed for the Sample C photoconductor. For a thick GeSn photoconductor (Sample D), EQE spectra are improved due to thick GeSn thickness. Sn content increase from bottom to top during the growth, which causes the cut-off wavelength beyond 2,200 nm wavelength.

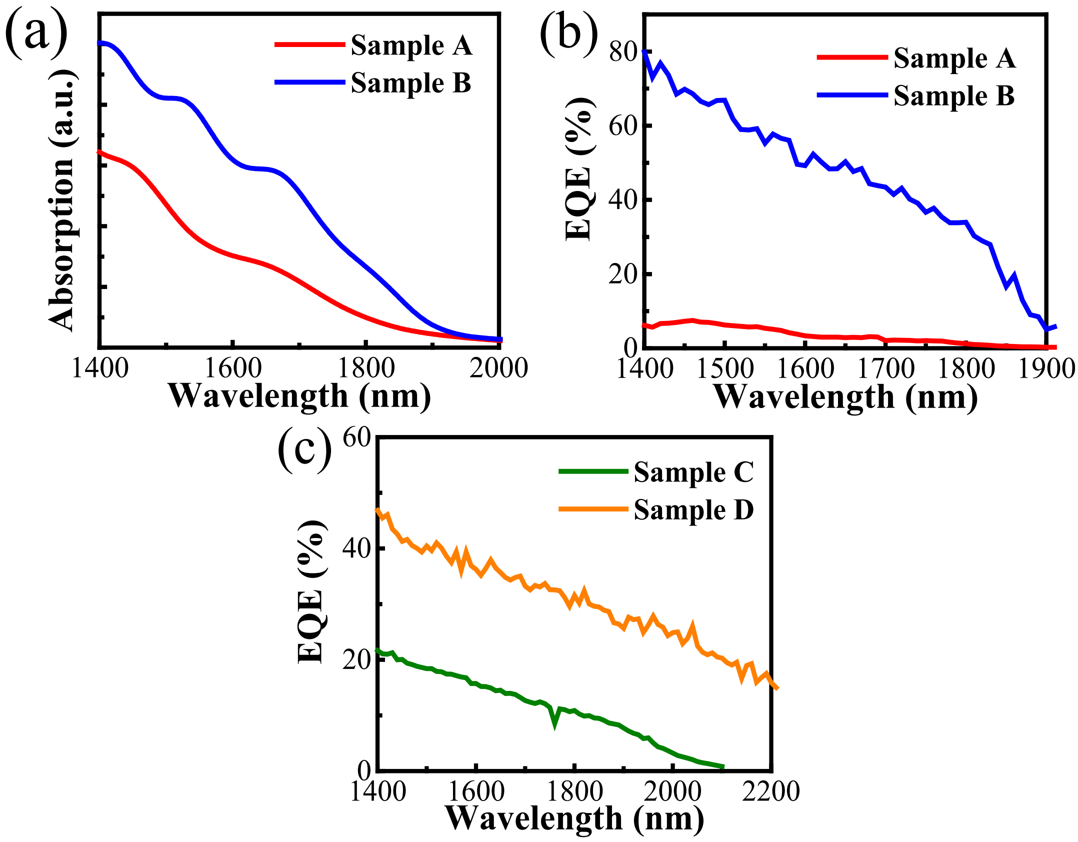

Figure 73. (a) Extracted absorption spectra for Sample A and B. n and k values were extracted from Ellipsometry. EQE spectra with respect to the wavelength of 1,400 to 2,200 nm for (b) Sample A and B and (c) Sample C and Sample D photoconductors.

5.2.5 Photoluminescence and Photoconductivity

A radiative recombination process in GeSn films was investigated via PL measurement using a pump laser at 1,064 nm wavelength. A laser was focused on samples with a spot size of ~10 μm at room temperature using a reflective objective lens. The optical response was received by an extended InGaAs detector. Figure 74(a) displays the PL spectra in comparison with PC spectra for Sample A. The broad PL shape is obtained with a peak point at 0.57 eV. The PC spectra for Sample A displays the cut-off energy at 0.66 eV.

PL spectra for Sample B are compared with PC spectra in Figure 74(b). Direct and indirect bandgap emissions are clearly observed at 0.63 and 0.66 eV, respectively [148]. The PL direct bandgap emission matches the cut-off energy in the PC spectra. This indicates that the cut-off energy in the PC spectra mainly originates from a GeSn direct bandgap. However, interestingly the direct and indirect band emissions are not observed in the PL spectra for Sample A. This PL peak point of 0.57 eV in Figure 74(a) is significantly related to trap states near GeSn/Ge. Previously, deep defect states were observed at 0.55 and 0.62 eV for $Ge_{0.968}Sn_{0.032}$ and $Ge_{0.96}Sn_{0.04}$ at 83 K, respectively [149]. Also, defect-related PL peaks were observed in thin GeSn films with Sn contents from 1.2 to 5.0% [150]. Electrically driven carrier dynamics were affected by trap states near the GeSn/Ge interface [151]. Because the non-radiative recombination process is much faster than the interband recombination process, photoexcited carriers are scattered into the *L* conduction band, SRH centers, or trap states at the interface/surface [152]. Especially for thin GeSn, the non-recombination process is more severe, leading to suppressed the interband emission. In contrast, trap-related emission is clearly observed. By increasing GeSn thickness (Sample B), however, the trap-related emission is suppressed and interband emission is enhanced. Most dislocations/traps are present near the GeSn/Ge interface. The high-quality GeSn layer with fewer dislocations is achieved on a top region [138]. As a result, the generated EHPs in GeSn bulk are recombined via the interband band before carriers are captured at the trap states near the interface, leading to improved direct and indirect interband emissions.

The PL and PC spectra for Sample C were shown in Figure 74(c). The PL peak appears at 0.62 eV, which is consistent with the cut-off energy in the PC spectra [148]. Although GeSn is thin for Sample C, the radiative recombination via direct band-edges is dominant in contrast to Sample A in Figure 74(a). GeSn for Sample A and B contains the misfit dislocations mostly near the interface. As observed in Figure 74(b), GeSn curves for Sample A and B are symmetric, indicating that the defective Sn gradient layer is not grown for the strain relaxation in the top GeSn layer. For Sample C and D, the strain relaxation is occurred by growing defective Sn gradient layer in interior GeSn. Figure 74(c) displays the asymmetric GeSn curve for Sample C, meaning that the bottom GeSn layer serves as the Sn gradient layer. Thus, many dislocations/defects at the GeSn interface extended into GeSn. Various trap levels in bulk GeSn are created by forming the 90° Lomer and 60° mixed dislocations [147].

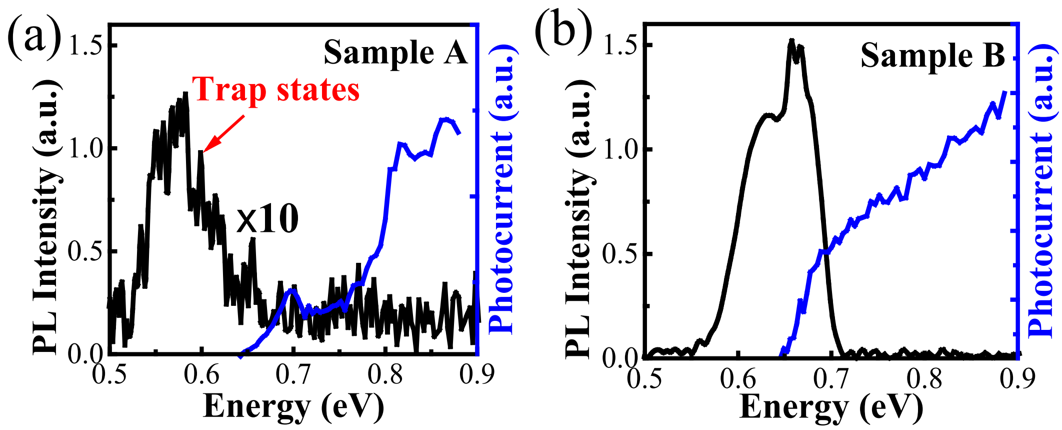

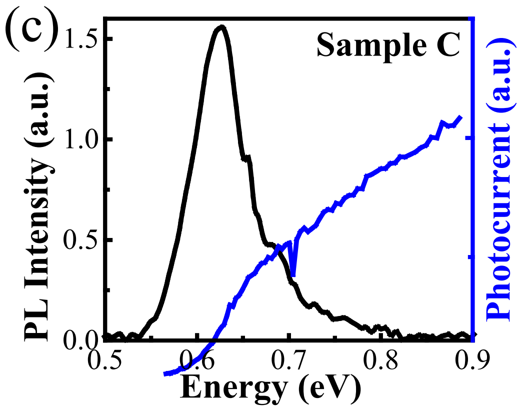

Figure 74. PL spectra for (a) Sample A, (b) Sample B, and (c) Sample C in comparison with the PC spectra at 300 K.

5.3 Summary

Alloying Sn with Ge is a promising material choice for the MIR range photodetection in the new technological advances. The cut-off wavelength can be tunable by adjusting the Sn contents. Although numerous efforts have been made for high-performance GeSn photodetectors, high density of dislocations/defects in GeSn films restrict photodetector performances in terms of dark current and optical responsivity. Therefore, a systematic study on trap-related carrier dynamics should be carefully investigated to further provide future directions for high efficient photodetection in GeSn material systems.

In order to investigate the carrier dynamics related to defects, GeSn films with varying Sn contents and different thicknesses were grown and studied electrically and optically in Chapter 5.3. Through the temperature-dependent I_{dark}-V study, ϕ_b for thick GeSn (Sample B and D) is improved in comparison with ϕ_b for thin GeSn (Sample A and C). This is because the thermionic emission process is dominant for thick GeSn, while two-step TAT and VBH mechanisms affect the carrier dynamics, leading to ϕ_b of -0.04 eV.

The photocurrent transient study for thin GeSn (Sample A) shows that the trap states near the interface induce overshoot I_{photo}, resulting in low EQE. The overshot I_{photo} effect is suppressed for Sample B, C, and D. For thick GeSn (Sample B and D) the defective interface region is far from the electrodes so that generated EPHs are collected efficiently via electrodes. As a result, EQE for Sample B is improved by 10×. For Sample C, although GeSn is thin, various types of defects are formed in GeSn, leading to the suppression of trap-related carrier dynamics near the interface. The trap-related PL peak for Sample A was observed at 0.57 eV. For thick GeSn (Sample B), the PL peak of the direct band emission was observed while the interface-related peak is suppressed. Taking account into the discovered carrier dynamics at room temperature, lower Sn content and thick GeSn thickness would improve photo-emission and detection performances in GeSn material systems.

Chapter 6. Metal-semiconductor-metal Waveguide Photodetectors on a GeSn-on-insulator Platform for the 2 μm photodetection

In this chapter, MSM waveguide photodetectors will be demonstrated on a GeSnOI platform. Chapter 6.1 describes the reported GeSn photodetectors the advantages of waveguide photodetectors. Chapter 6.2 will introduce the demonstration of the GeSnOI platform and the photodetector fabrication. Chapter 6.3 discusses the characterization of the GeSnOI platform and of the waveguide photodetectors. Chapter 6.4 will summarize the contents in Chapter 4.

6.1 GeSn Waveguide Photodetectors

Diverse GeSn photodetectors have been developed in the past decades. The low responsivity for GeSn photodetectors was improved by high optical confinement from SOI platforms. The enhanced optical confinement led to the high responsivity of 0.376 A/W at 1820 nm despite a thin *i*-GeSn of 440 nm [42]. Responsivity for GeSn photodetectors is further enhanced with photon-trapping hole structures, improving responsivity by 1.5× at 1,630 nm [78].

Waveguide photodetectors are one of the promising devices for high optical performances. A waveguide photodetector can vanish a trade-off between 3dB bandwidth and responsivity, which is typically observed for normal incidence photodetectors, by separating optical and electrical paths. As a result, the 3dB bandwidth of 10 GHz was achieved at -7 V for MQW GeSn waveguide photodetectors, showing the responsivity of ~0.1 A/W at 2,000 nm [154]. In addition, other GeSn waveguide photodetectors have been demonstrated on Ge buffer layers on Si substrate [155]. However, the main interests of 2,000 nm for waveguide photodetectors have not been thoroughly studied yet. Also, an insulator platform has not been realized for responsivity improvement.

The theoretical expectation of a GeSn waveguide photodetector has not been achieved experimentally [158]. As described in Chapter 5, the trap states near the GeSn/Ge interface largely restrict the optical and electrical properties. By growing thick GeSn, the trap-related carrier dynamics are suppressed, resulting in low leakage current and improved EQE. In another way, a GeSn layer on insulator platforms, isolated from Ge and Si layers, could potentially provide low dark current and enhanced responsivity due to the electrical isolation and high optical confinement of the insulator platforms.

Recently, a GeSnOI platform via DWB and layer transfer techniques were introduced to remove a defective GeSn/Ge interface that can potentially improve photodetector performances [133]. In Chapter 6, GeSn waveguide photodetectors are demonstrated on the GeSnOI platform. The systematic characteristics of a GeSnOI platform reveal that GeSn is isolated from the Ge buffer and Si layers. Waveguide MSM photodetectors on the GeSnOI platform are characterized. The dark current for the photodetector is 550 nA.

The optical responsivity is revealed to be 0.24 and 0.06 A/W at 1,600 and 2,003 nm, respectively, under normal incidence illumination.

6.2 Demonstration of GeSnOI Waveguide Photodetectors

In this section, GeSnOI waveguide photodetectors will be demonstrated. Chapter 6.2.1 will describe the demonstration of GeSnOI. The demonstration of waveguide photodetectors will be addressed in Chapter 6.2.2. This section aims to demonstrate waveguide photodetectors on a GeSn/Ge interface-free GeSnOI platform.

6.2.1 Demonstration and Characterization of GeSnOI Platforms

GeSn and Ge buffer layers were grown on an 8-inch Si wafer via RPCVD. Two insulator layers of SiN and SiO_2 were deposited on handle and donor Si wafers. CMP and O_2 plasma exposure were conducted for successful DWB. After that, DWB and transfer technologies were performed using a pair of the Si wafers at 300°C in N_2 ambient, preventing Sn segregation/precipitation. After that, mechanical grinding and wet etching were implemented to remove the Si donor layer. Figure 75(a)-(c) displays the schematic images of fabrication flows for the GeSnOI platform. Figure 75(d) represents the schematic image of completed waveguide photodetectors on the GeSnOI wafer.

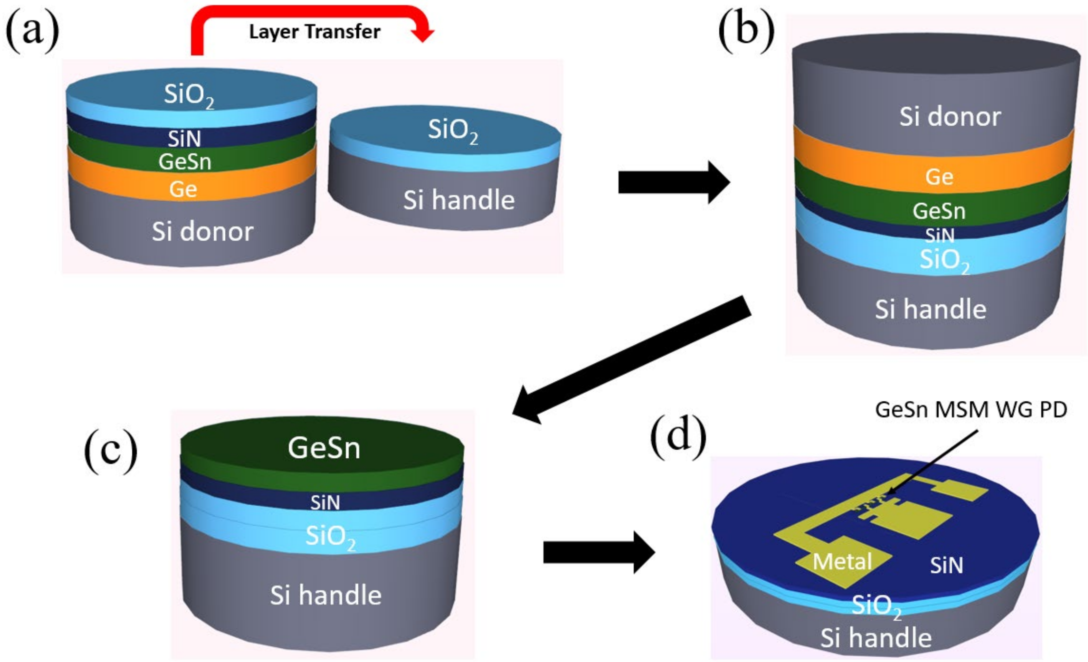

Figure 75. The fabrication steps for waveguide photodetectors via DWB and layer transfer techniques. (a) preparation of the wafer pair, (b) DWB process, (c) the removal of the Ge and Si donor layer, and (d) the MSM waveguide photodetector on the GeSnOI wafer.

HRXRD in the *2θ-ω* direction and RSM (224) analysis for the demonstrated GeSnOI platform were obtained in Figure 76(a) and (b), respectively. In Figure 76(a), GeSn and Si curves are observed, indicating the GeSn/Ge intermixed layer was removed. Figure 76(b) displays the RSM image of GeSn and Si without Ge, indicating a GeSn/Ge interface-free GeSnOI platform is successfully demonstrated. The estimated Sn content was ~9%. The GeSn layer is under compressive strain.

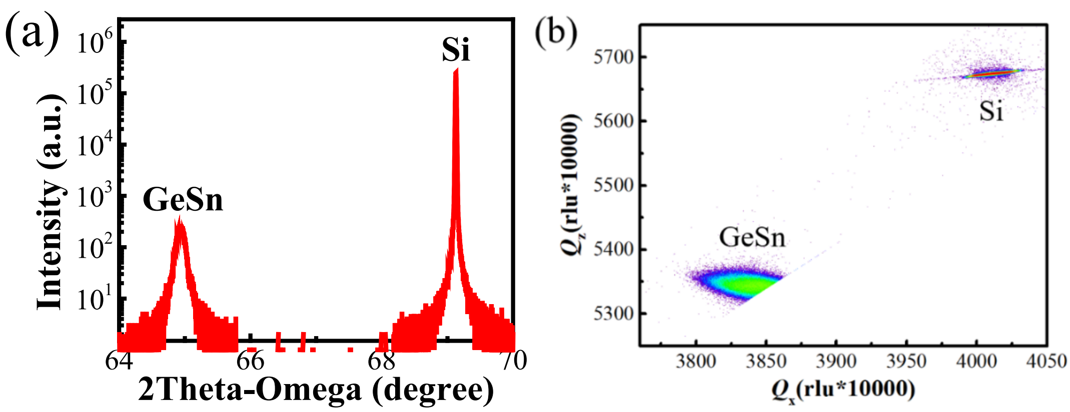

Figure 76. (a) The HRXRD curve of GeSnOI in the *2θ-ω* scan. (b) The RSM image in (224) plane for GeSnOI.

A cross-sectional view of the TEM image of GeSnOI is shown in Figure 77(a). A GeSn thickness is ~133 nm. A thickness of SiN/SiO_2 was ~500 nm. A PL measurement was performed in temperature range from 5 to 300 K in Figure 77(b). A sharp PL peak is observed at ~2,200 nm at 5 K. At 300 K, the broad emission peak is obtained near 2,400 nm [159]. The PL peak at 5 K is attributed to direct bandgap emission. This indicates that the cut-off wavelength of photodetectors could be beyond 2,200 nm at room temperature. Figure 77(c) represents various element SIMS profiles. A uniform Sn content of 8.9% was distributed, signifying that a wafer-scale GeSnOI platform can be realized via the DWB and layer transfer techniques. Figure 77(d) displays Raman spectroscopy for the GeSnOI platform. A GeSn peak is observed at 294.4 cm^{-1}, which is lower than Ge bulk (300.6 cm^{-1}). The Raman peak shift can tell Sn content and strain by using the following equation [162],

$$\Delta\omega = -88x + 521\varepsilon_{Strain}, \quad (36)$$

where $\Delta\omega$ and ε_{strain} are Raman spectral shift and strain, respectively. Given the Sn content of ~8.9%, strain was estimated to be -0.23%. This strain value is relaxed in comparison with as-grown GeSn with a Sn content of 9% due to strain-relaxation during the bonding processes.

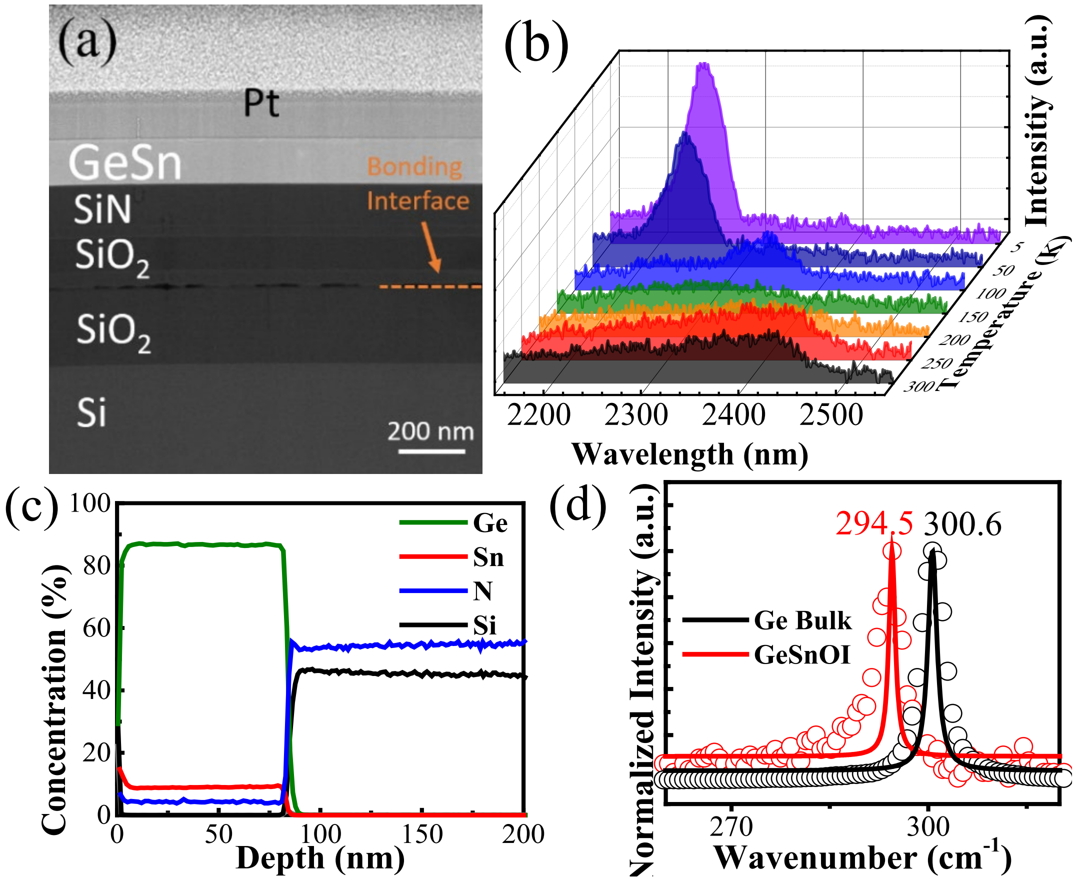

Figure 77. (a) The cross-view of the TEM image for the GeSnOI substrate. (b) SIMS content profiles for GeSnOI substrate. (c) PL measurements as a function of wavelength in temperature ranging from 5 to 300 K. (d) Raman spectroscopy for GeSnOI along with the one for Ge bulk as reference.

6.2.2 Demonstration of Waveguide Photodetectors on GeSnOI Platforms

MSM waveguide photodetectors were then demonstrated using the GeSnOI platform. A Cl_2-based RIE process was implemented to define waveguides with 1 µm width and varying waveguide lengths of 12, 36, 72, and 108 µm. A thin Al_2O_3 layer with 1 nm thickness was deposited via ALD for suppression on a Fermi pinning effect and for an etch stop layer [161]. After that, SiN was covered on the waveguides using PECVD. The SF_6-based RIE process was performed to open metal-contact holes. A metal deposition of 20nm Ti / 50nm TiN / 300nm Al was done via sputtering, followed by a lift-off process. The 3D schematic image of a demonstrated waveguide MSM photodetector on a GeSnOI platform is shown in Figure 78(a). The planer view of the SEM image of the photodetector is shown in Figure 78(b). The zoom-in image of a GeSn waveguide is displayed in the inset of Figure 78(b).

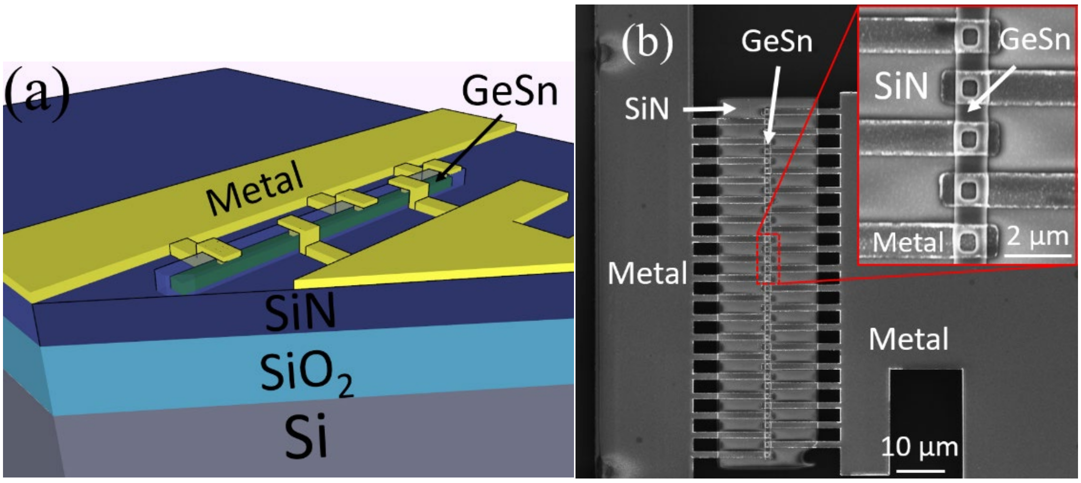

Figure 78. (a) The 3D schematic image of the GeSnOI MSM photodetector. (b) The planar view of the SEM image of GeSnOI MSM photodetector with a length of 72 µm. The inset in Figure 78(b) shows the zoom-in image of the GeSn waveguide.

6.3 Characterization of Waveguide Photodetectors on the GeSnOI Platform

The demonstrated waveguide photodetectors on the GeSnOI platform will be characterized in Chapter 6.3. A dark current analysis will be addressed in Chapter 6.3.1. Chapter 6.3.2 will describe temperature-dependent dark current and leakage current mechanisms. In Chapter 6.3.3, optical response for the photodetectors will be addressed. Frequency response for the photodetectors will be described in Chapter 6.3.4.

6.3.1 Dark Current Analysis

I_{dark}-V characteristics of the waveguide photodetectors were shown in Figure 79(a). Symmetric I_{dark} curves in forward and reverse bias ranges are attributed to equivalent electrode conditions. A non-linear shape of I_{dark} was observed, meaning that Schottky contact between metal and GeSn is formed. I_{dark} for the photodetectors was measured to be 550 nA with a waveguide length of 12 μm. I_{dark} increases to 6.5 μA with the length is 108 μm. Figure 79(b) displays I_{dark} for the GeSn waveguide photodetectors at 1 V as a function of the waveguide lengths. In order to further reduce the leakage current, GeSn with low Sn content can potentially reduce I_{dark} [128]. Also, the strain engineering can achieve high performance GeSn photodetectors. To reduce J_{surf}, the advanced surface passivation technique is necessary. J_{surf} was suppressed by ~100× using the Si surface passivation layer [74]. Second, the $GeSnO_x$ surface passivation is potentially promising to alleviate the surface defect density [162].

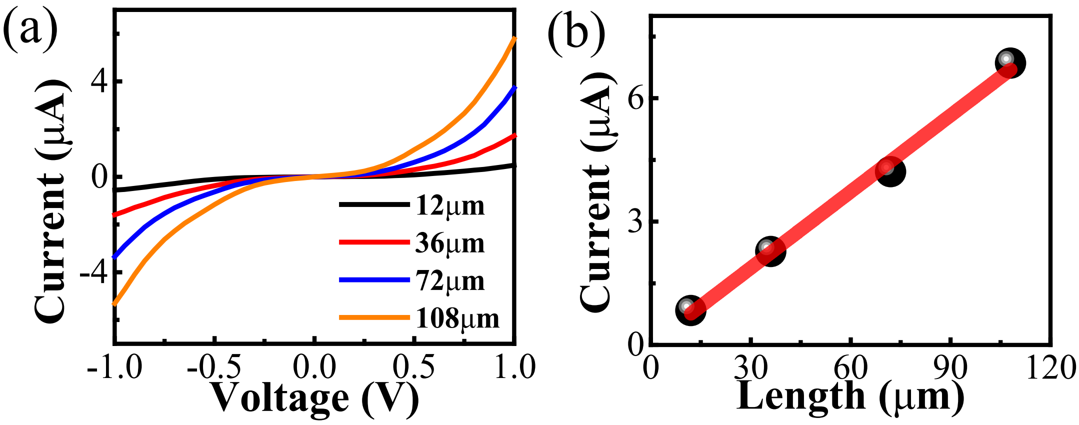

Figure 79. (a) I_{dark}-V characteristics for GeSnOI MSM photodetectors with varying lengths of waveguides. (b) I_{dark} for GeSnOI MSM photodetectors as a function of lengths at 1 V.

6.3.2 Temperature-dependent Dark Current Study

Temperature-dependent I_{dark}-V characteristics were performed in Figure 80(a). I_{dark}-V curves were measured in the temperature range from 293 to 353 K. I_{dark} increases with the temperature. The Arrhenius plot for the waveguide photodetector was extracted in Figure 80(b). The estimated ϕ_b is obtained to be 70 meV. The *C-V* curve for the waveguide photodetector was measured. And the $1/C^2$-V characteristic can be obtained by the following equation,

$$1/C^2 = \frac{2}{q\varepsilon N_D}(V_{bi} - V - kT/e), \qquad (37)$$

where V_{bi}, ε, and N_D are the built-in potential, the GeSn permittivity, and the doping concentration, respectively [163]. The estimated V_{bi} for the photodetector is 0.38 eV in Figure 80(c). The estimated ϕ_b for GeSn is lower than V_{bi} although no *ex-situ* or *in-situ* doping process was performed. Lower ϕ_b is attributed to the bandgap narrowing for GeSn. When the GeSn bandgap becomes narrow by adding Sn content, SBH between GeSn/metal is deformed. Second, the higher Sn contents, the higher defect density. Thus, the unintended *p*-type doping concentration increases with GeSn with high Sn contents, reducing SBH [164]. Last, many dislocations/defects in epi-GeSn enhance two-step TAT and VRG conduction mechanisms. Two-step TAT is described with the equation of $exp(-E_a/kT)$. Figure 80(d) displays the I_{dark}-$1/kT$ curve for the photodetector. The extracted E_a is 8 meV. The inset in Fig 75(d) shows the schematic image of the band diagram for the two-step TAT process. Based on the one-dimensional (1D)-VRH model, the conductivity (σ) can be described by the following equation [141],

$$\sigma = \sigma_0 exp\, [-(T_1/T)^{1/2}] \qquad (38)$$

where σ_0 is a fitting parameter of the conductance at temperature >> T_1. T_1 is the characteristic temperature. Fig. 75(e) displays the σ characteristic for the waveguide photodetector as a function of $1/T^{1/2}$. Comparing Figure 80(d) with Figure 80(e), there is no noticeable difference, implying that it is difficult to determine which mechanism the leakage current is governed by.

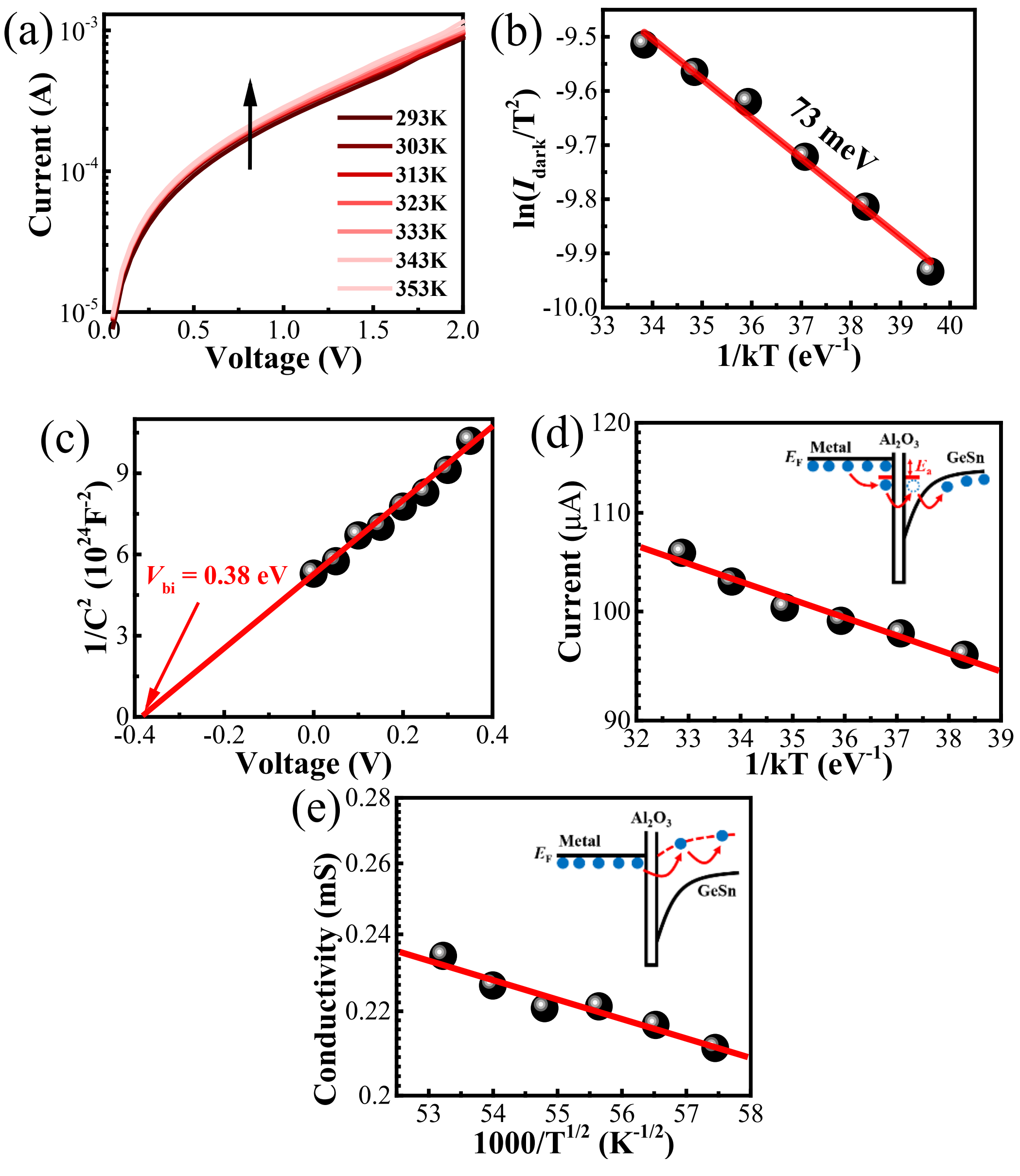

Figure 80. (a) Temperature-dependent I_{dark}-V characteristic for the waveguide photodetector. The arrow represents the temperature increasing from 293 to 353 K. (b) Arrhenius plot for the photodetector as a function of $1/kT$. (c) $1/C^2$-V characteristics for the photodetectors. (d) I_{dark}-$1/kT$ characteristics. The inset in Figure 80(d) represents the band diagram for the two-

step TAT process. (e) The conductivity of the photodetectors as a function of *1000/*$T^{1/2}$. The inset in Figure 80(e) represents the band diagram for the 1D-VRH process.

6.3.3 Photocurrent Analysis

The optical response was conducted under normal incidence illumination. Figure 81(a) displays the I_{dark}- and I_{photo}-V curves for photodetectors. I_{photo} is higher than I_{dark}, meaning that EHPs are generated under illumination, and they are collected to electrodes. The responsivity can be calculated by Eq. (7). An electrode shadowing effect was considered for the P_{in} calculation. Different wavelengths, i.e., 1,600, 1,934, 2,003, and 2,033 nm, were selected for optical responsivity measurements. The responsivity for the photodetector at each wavelength is shown in Figure 81(b). The responsivity increases with voltage because carrier mobility is improved by electric filed at high bias voltage. The responsivity was estimated to be 0.24 and 0.06 A/W at -2 V at 1,600 and 2,003 nm, respectively. The responsivity decreases with the increase in wavelength. Optical responsivity can be enhanced by using thick GeSn or by employing photon-trapping hole structures. As shown in Figure 77(b), the demonstrated photodetector is potentially acceptable to cover photodetection up to 2,200 nm. Ellipsometry is an attractive tool to determine the optical properties of thin films. Figure 81(c) displays the absorption coefficient spectra for GeSn as a function of wavelength in comparison with Ge bulk [117]. The GeSn absorption coefficient is extended beyond 2,000 nm. Based on the extracted absorption coefficient, the absorption spectra are calculated via the FDTD simulation Figure 81(d). A simulated structure is referred to the TEM image in Figure 77(a). The responsivity points are added in another *y*-axis as a reference. It should be noted that the absorption spectra are consistent with the responsivity.

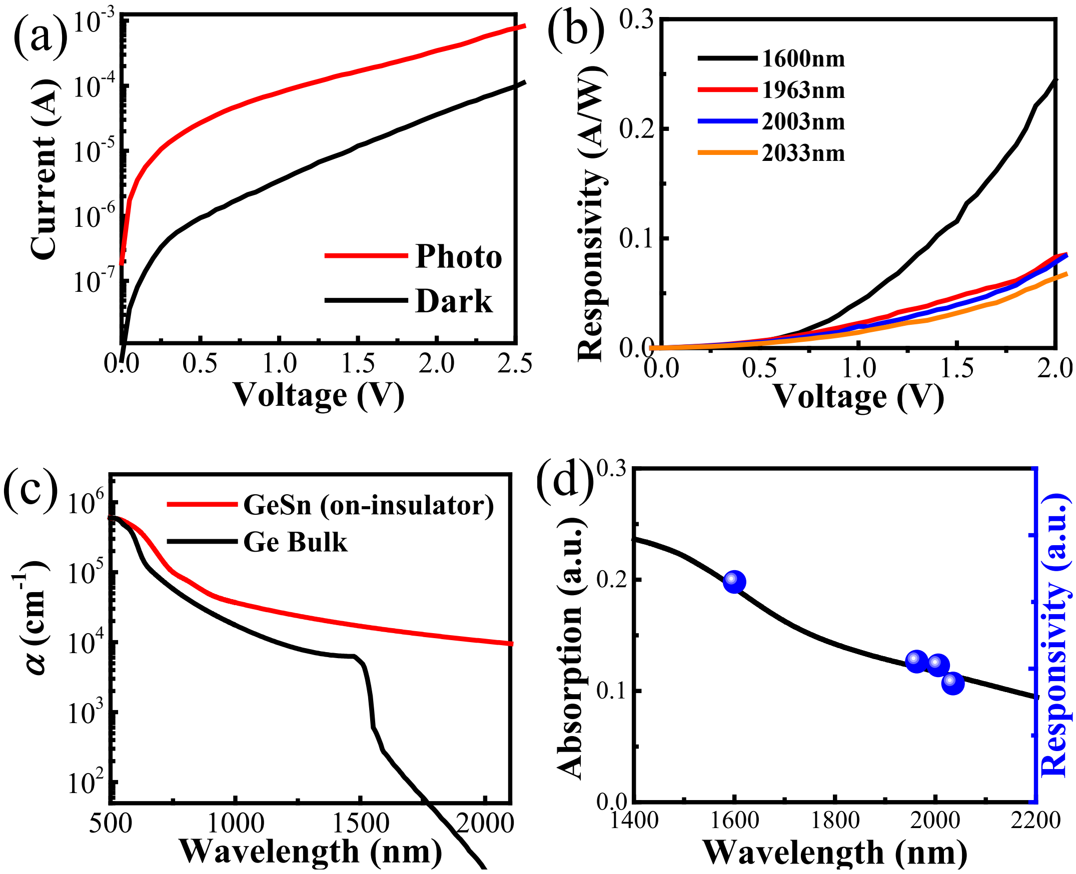

Figure 81. (a) I_{photo}-V characteristic for photodetectors at 1,933 nm. (b) The responsivity for photodetectors at different wavelengths. (c) Extracted α for GeSn and Ge bulk as a reference. (d) The calculated absorption spectra (black line) for the photodetectors along with the measured responsivity (blue dots).

Figure 82 displays benchmarked dark current densities for the reported GeSn waveguide-shape photodetectors [154]. Reducing dark current density is one of the important factors to improve the photodetector performance. A GeSn/Ge heterostructure was first suggested for GeSn waveguide photodetectors [157]. A GeSn waveguide photodetector partially separated from a Ge buffer layer was demonstrated in Ref. 155. GeSn/Ge MQW structures were introduced to suppress dark current density through suppressed strain relaxation [154]. Although the reported photodetectors displayed good performance in terms of responsivity 3dB bandwidth, they have suffered from high leakage current densities. In this Chapter, a GeSnOI platform is proposed to reduce dark current density by isolating the active region from the substrate. It should be noted that this platform takes advantage of high optical confinement [42].

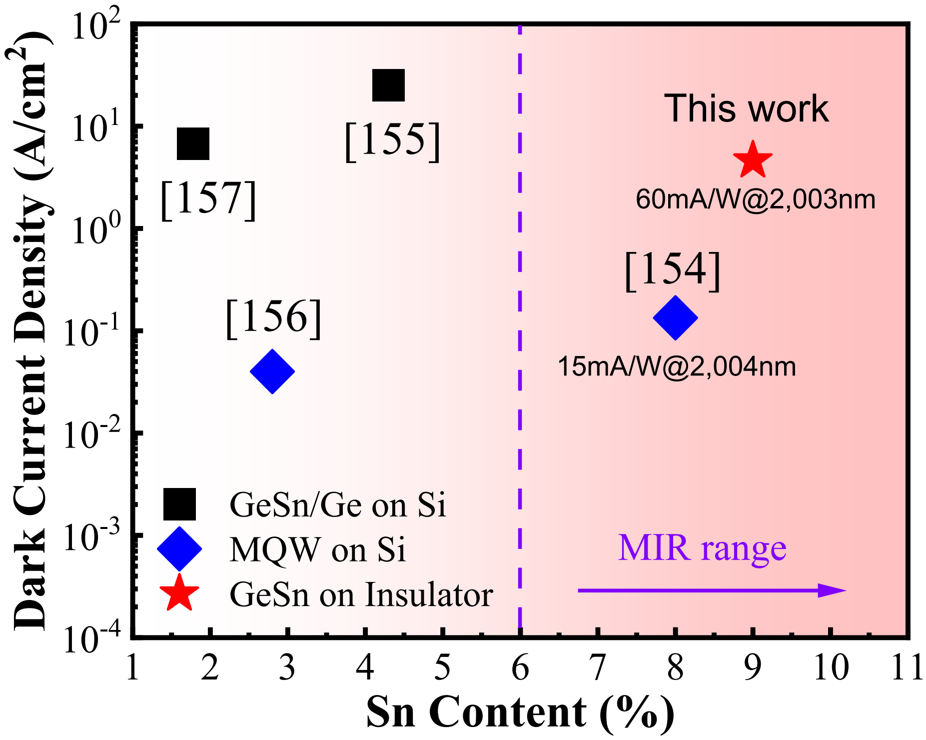

Figure 82. Benchmarking of the dark leakage current densities for the reported waveguide-shape GeSn photodetectors on the different platforms [154]. Dark current for each waveguide photodetector is benchmarked with respect to Sn content. Photodetectors in Ref 154,156 contain the GeSn MQW on Ge on Si substrate, and the photodetectors in Ref 155,157 have GeSn on Ge on Si substrate. The waveguide photodetectors were cleaved for the optical measurement in Ref 155-157. The photodetectors in this work were demonstrated on the GeSn/Ge interface-free GeSnOI platform.

6.3.4 Frequency Response

Experiments for frequency-response were conducted at 1,550 and 2,000 nm in Figure 83(a)-(b), respectively. f_{3dB} are 1.26 and 0.81 GHz at 1,550 and 2,000 nm at 0.5 V, respectively. f_{3dB} is determined by *RC* delay and carrier transit time. Typically, the *RC* delay bandwidth is not critical in a waveguide photodetector, while f_{3dB} is mainly attributed to f_T [155]. The measured capacitance for the photodetector was obtained to be 0.5 pF, meaning that f_{3dB} is limited by f_T. Depletion width and carrier velocity contribute to transit time. Where voltage is high, the strong electric field is distributed in a GeSn layer, increasing depletion width. Inset in Figure 85(a) displays 3dB bandwidth as a function of applied voltage. It should be noted that the voltage increase reduces f_{3dB}, meaning that a waveguide photodetector is restricted by f_T.

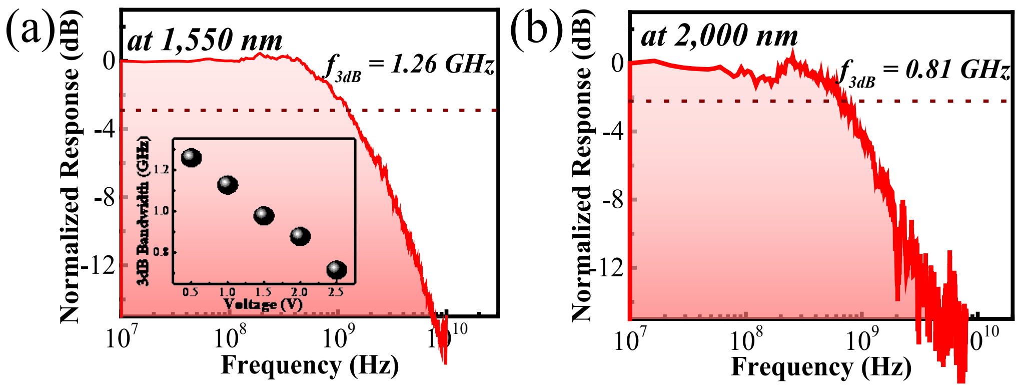

Figure 83. Frequency response for the photodetectors (a) at 1,550 nm and (b) at 2,000 nm at 0.5V. The inset in Figure 83(a) displays the 3dB bandwidth for the photodetector as a function of voltage.

6.4 Summary

MSM waveguide photodetectors were demonstrated on a GeSnOI platform, and they were characterized. The measured I_{dark} for photodetectors is 550 nA at -1 V with a waveguide length of 12 μm. Low I_{dark} results from the electrical isolation of an insulator substrate. The obtained responsivity was 0.24 and 0.06 A/W at 1,600 and 2,003 nm, respectively. According to the PL measurement and the extracted absorption coefficient, the demonstrated waveguide photodetector can potentially enable photodetection beyond

2,200 nm. 3dB bandwidth was obtained to be 1.26 GHz at 1,550 nm, restricted by carrier transit time. The demonstrated GeSnOI waveguide photodetectors are suitable for CMOS-compatible and low-cost Si-based PICs for the 2 μm applications.

Chapter 7. Conclusion and Future Work

7.1 Conclusion

The demand for optical sensing, imaging, and interconnects in NIR and MIR ranges has increased in past decades for the new technological advances. Ge and GeSn alloys are promising as material choices to cover the interesting wavelength ranges, thanks to their CMOS-compatible processes and considerable electrical/optical properties. Ge is attractive for NIR range photodetection. GeSn alloys are favorable for MIR range photodetection.

Optical/electrical devices have been demonstrated with on-insulator platforms, e.g., SOI, GOI, and GeSnOI, benefiting from electrical isolation and improved optical confinement. Especially for a photodetector, on-insulator platforms contribute to low dark current and improved responsivity. This thesis emphasized the importance of Ge/GeSn photodetectors/photoconductors on insulator platforms. GOI and GeSnOI platforms were mainly demonstrated for device demonstration via DWB and layer transfer techniques, facilitating advanced PICs.

Chapter 3 addressed vertical *p-i-n* photodetectors on a GOI platform with their dependence on defects and surface passivation. Huge dark current density, one of the key drawbacks of a Ge photodetector, was suppressed bu mitigating trap-related carrier dynamics. The TDD reduction and GeO_x passivation contributed to achieving the dark current of sub-mA/cm^2 for Ge photodetectors. The ~100× reduction in TDD was obtained via O_2 anneal and

HF etch processes, leading to the ~400× reduction in bulk leakage current. As TDD is reduced, surface leakage current is dominant. GeO_x surface passivation was adopted to suppress the huge surface leakage current. As a result, surface leakage current is reduced by ~10× due to the advanced passivation technique via O_3 oxidation.

Chapter 4 described hole-array vertical *p-i-n* photodetectors on a GOI platform. The improved responsivity of 0.74 A/W was achieved with the gourd-shaped hole array structures. The gourd-shaped hole array provided enhanced optical absorption in comparison with the cylinder-shaped hole array design. As a result, the estimated specific detectivity was 3.1×10^{10} $cm \cdot Hz^{1/2} \cdot W^{-1}$ at 1,550 nm, which is comparable to those of commercial Ge bulk and extended-InGaAs photodiodes.

Chapter 5 explored trap-related carrier dynamics in GeSn material systems. A systematic study on GeSn photoconductors revealed that trap states near a GeSn/Ge interface played the key role to degrade electrical and optical properties. By increasing the thickness from 180 to 900 nm, the trap-related characteristic was largely suppressed. The increases in thickness resulted in EQE improvement by 10×.

In Chapter 6, waveguide-shape photodetectors were demonstrated on a GeSnOI platform. A GeSn/Ge interface was successfully removed away via DWB and layer transfer techniques. The demonstrated photodetectors displayed the dark current of 550 nA. The responsivity of 0.24 and 0.06 A/W was achieved at 1,550 and 2,003 nm, respectively. The photodetectors could potentially enabled photodetection beyond 2,200 nm based on PL and the extracted *n* and *k* indies.

To summarize, Ge/GeSn photodetectors were demonstrated on insulator platforms, i.e., GOI and GeSnOI. For NIR range photodetection, vertical *p-i-n* Ge photodetectors were introduced with the excellent responsivity of 0.74 A/W and the ultra-low dark current density of sub-mA/cm^2. The estimated specific detectivity for the Ge photodetector is comparable to commercial Ge bulk/extended-InGaAs photodetectors. For MIR range photodetection, GeSn alloys were introduced. Trap states near the GeSn/Ge interface degraded the electrical and optical performances of GeSn-based optical devices. To remove the defective GeSn/Ge interface, a GeSnOI platform was introduced for the demonstration of photodetectors. Demonstrated GeSn waveguide photodetectors allowed the 2,000 nm photodetection, suitable for diverse applications. The proposed approaches in this thesis provide low-cost and CMOS-compatible photodetectors enabled for Si-based PICs in NIR and MIR ranges.

7.2 Future Directions

7.2.1 APD on GOI Platforms

To further enhance the optical responsivity for a Ge photodetector, the demonstration of APD is one of the promising approaches. Especially separated absorption and multiplication region avalanche photodiodes (SAM-APDs) have taken much attention due to low noise and high gain-bandwidth products. A proposed structure for SAM-APDs on a GOI platform is shown in

Figure 84. central region and side-ring structures serve as the absorption and multiplication regions, respectively. The light is shone on a central region. Photoexcited holes are transferred to a multiplication region and they are amplificated. The proposed APD structure on a GOI platform could benefit from low dark current density and low dark current count for single-photon avalanche photodiodes.

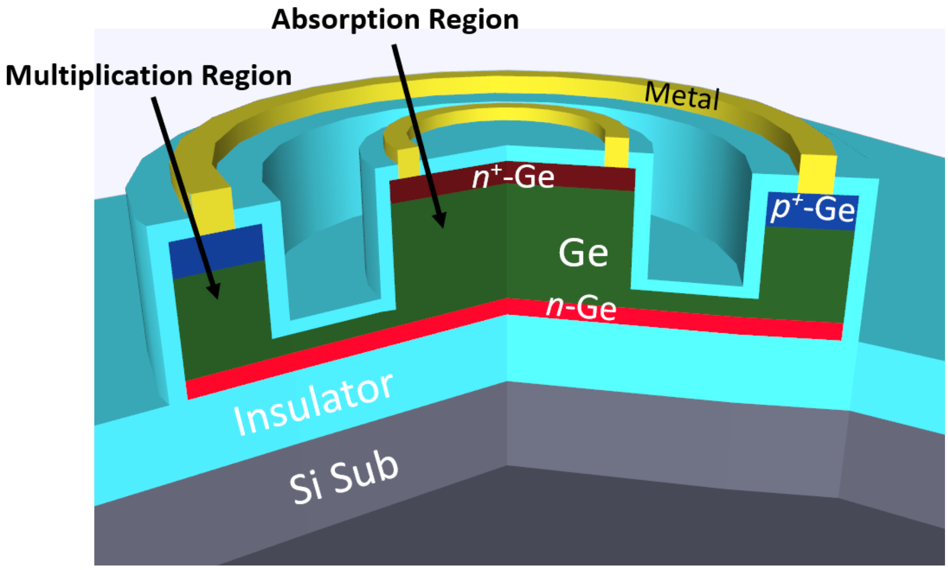

Figure 84. The 3D schematic image of APD on the GOI platform.

7.2.2 Tensile strained GeSn Photodetectors on the GeSnOI Platform

Recently, it has been reported strain engineering enabled realizing ultra-low optical threshold lasing. Similarly, employing strain engineering to GeSn photodetectors would be attractive for high performance GeSn photodetectors. Because GeSn photodetectors with high Sn contents suffer from a huge dark current, tensile-strained GeSn is desirable. Two following approaches below can achieve strained GeSn photodetectors.

First, a low Sn content film grown on a high Sn content film is prepared. A tensile-strained GeSn film is transferred on insulator platforms via DWB and layer transfer techniques. By removing high Sn content layers, the tensile strained GeSn on an insulator layer can be released on insulators. The tensile-strained GeSn can be fabricated into a waveguide photodetector, as shown in Figure 85(a). The tensile-strained GeSn photodetector is expected to show the extended cut-off wavelength due to bandgap shrinkable.

Second, employing SiN stressor on a GeSn waveguide can extend the cut-off wavelength. As-grown GeSn on a Ge SRB layer suffers from compressive strain. Although a GeSnOI platform contributes to strain-relaxation, GeSn is still under compressive strain. The SiN stressor deposition with self-aligned dry etching could potentially transit GeSn from compressive to tensile strain [67]. The schematic image of the stressed-GeSn waveguide is shown in Figure 85(b).

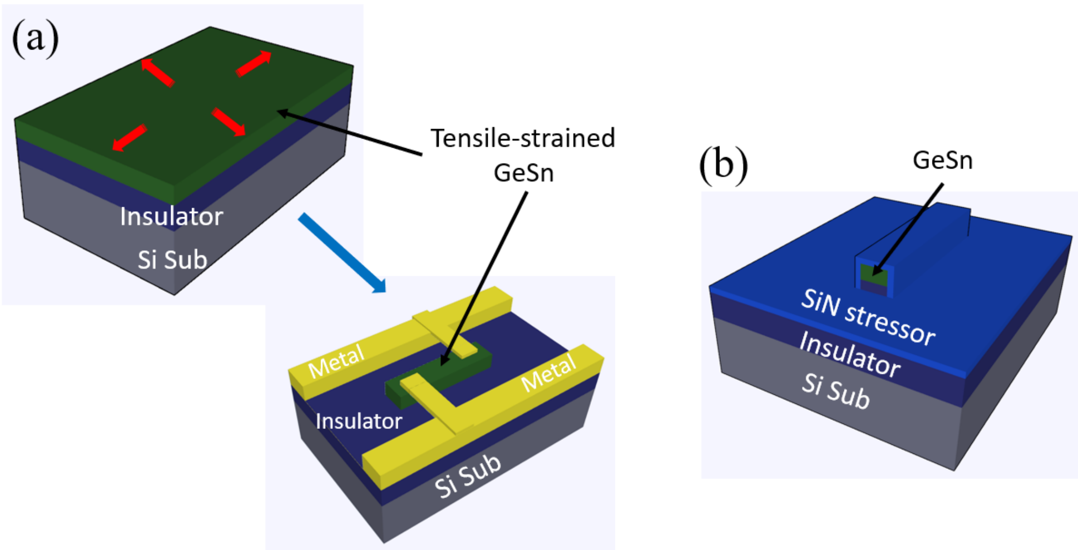

Figure 85. (a) The 3D schematic images of the tensile-strained GeSn on insulator and its waveguide-shape photodetector. (b) The 3D schematic image of the tensile-strained GeSn waveguide-shape photodetector on an insulator platform employed by a SiN stressor.

References

[1] R. Soref, and B. Bennett, “Eletrooptical effects in silicon,” *IEEE Journal of Quantum Electronics* **23**(1), pp. 123-129 (1987).

[2] S. Y. Siew, B. Li, F. Gao, H. Y. Zheng, W. Zhang, P. Guo, S. W. Xie, A. Song, B. Dong, L. W. Liu, C. Li, and X. Luo, “Review of Silicon Photonics Technology and Platform Development,” *Journal of Lightwave Technology* **39**(13), pp. 4374-4389 (2021).

[3] M. Smit, X. Liijtens, H. Ambrosius, E. Bente, J. van der Tol. B. Smalbrugge, T. de Vries, E.-J. Geluk, J. Bolk, R. van Veldhoven, L. Augustin, P. Thijs, D. D’Agostino, H. Rabbani, K. Lawniczuk, S. Stopinski, S. Tahvili, A. Corradi, E. Kleijn, D. Dzibrou, M. Felicetti, E. Bitincka, V. Moskalenko, J. Zhao, R. Santos, G. Gilardi, W. Yao, K. Williams, P. Stabile, P. Kuindersma, J. Pello, S. Bhat, Y. Jiao, D. Heiss, G. Roelkens, M. Wale, P. Firth, F. Soares, N. Grote, N. schell, H. Debregeas, M. Achouche, J.-L. Gentner, A. Bakker, T. Korthorst, D. Gallagher, A. Dabbd, A. Melloni, F. Morichetti, D. Melati, A. Wonfor, R. Penty, R. Broeke, B. Musk, and D. Robbins, “An introduction to InP-based generic integration technology,” *Semiconductor Science and Technology* **29**, 083001 (2014).

[4] C. Qiu, Z. Sheng, H. Li, W. Liu, . Li, A. Pang, A. Wu, X. Wang, S. Zou, and F. Gan, “Fabrication, Characterization and Loss Analysis of Silicon Nanowaveguides,” *Journal of Lightwave Technology* **32**(13), pp. 2303-2307 (2014).

[5] D. Benedikovic, C. Alonso-Ramos, P. Cheben, J. H. Schmid, S. Wang, D.-X. Xu, J. Lapointe, S. Janz, R. Halir, A. Ortega-Moñux, J. G. Wangüemert-Pérez, I. Molina-Fernández, J.-M. Fédéli, L. Vivien, and M. Dado “High-directionality fiber-chip grating coupler with interleaved trenches and subwavgelength index-matching structure,” *Optics Letters* **40**(18), pp. 4190-4193 (2015).

[6] W. Cao, D. Hagan, D. J. Thomson, M. Nedelijkovic, C. G. Littlejohns, A. Knights, S.-U. Alam, J. Wang, F. Gardes, W. Zhang, S. Liu, K. Li, M. S. Rouifed, G. Xin, W. Wang, H. Wnag, G. T. Reed, and G. Z. Mashanovich, “High-speed silicon modulators for the 2 μm wavelength band”, *Optica* **5**(9), pp. 1055-1062 (2018).

[7] T. Hu, B. Dong, X. Luo, T.-Y. Liow, J. Song, C. Lee, and G.-Q. Lo “Silicon photonic platforms for mid-infrared applications,” *Photonics Research* **5**(5), pp. 417-430 (2017).

[8] R. Nagarajan, C. H. Joyner, R. P. Schneider, J. S. Bostak, T. Butrie, A. G. Dentai, V. G. Dominic, P. W. Evans, M. Kato, M. Kauffman, D. J. H. Lambert, S. K. Mathis, A. Mathur, R. H. Miles, M. L. Mitchell, M. J. Missey, S. Murthy, A. C. Nilsson, F. H. Peters, S. C. Pennypacker, J. L. Pleumeekers, R. A. Salvatore, R. K. Schlenker, R. B. taylor, H.-S. Tsai, M. F. V. Leeuwen, J. webjorn, M. Ziari, D. Perkins, J. Singh, S. G. Grubb, M. S. Reffle, D. G. Mehuys, F. A. Kish, and D. F. Welch, "Large-scale photonic integrated circuits," *IEEE Journal of Selected Topics in Quantum Electronics* **11**(1), pp. 50-65 (2005).

[9] D. Lopez-Torres, C. Elosua, and F. J. Arregui, "Optical Fiber Sensors Based on Microstructured Optical Fibers to Detect Gases and Volatile Organic Compounds-A Review," *Sensors* **20**(9), 2555 (2020).

[10] S. Louvros, and D. Fuschelberger, "VLC Technology for Indoor LET Planning," System-Level Design Methodologies for Telecommunication. Springer, Cham (2013).

[11] E. Desurvire, C. Kazmierski, F. Lelarge, X. Marcadet, A. Scavennec, F. A. Kish, D. F. welch, R. Nagarajan, C. H. Joyner, R. P. Schneider, S. W. Corzine, M. Kato, P. W. Evanns, M. Ziari, A. G. Dentai, J. L. Pleumeekers, R. Muthiah, S. Bigo, M. Nakazawa, D. J. Richardson, F. Poletti, M. N. Petrovich, S. U. Alam, and W. H. Loh, "Science and technology challenges in XXIst century optical communications," *Comptes Rendus Phtsique* **12**, pp. 398-416 (2011).

[12] L. D. Smullin, and G. Fiocco, "Optical Echoes from the Moon," *Nature* **194**, 1267 (1962).

[13] I. Kim, R. J. Martins, J. Jang, T. Badloe, S. Khadir, H.-Y. Jung, H. Kim, P. Genevet, and J. Rho, "Nanophotonics for light detection and ranging technology," *Nature Nanotechnology* **16**, 508-524 (2021).

[14] C. Rogers, A. Y. Piggott, D. J. Thomson, R. F. Wiser, I. E. Opris, S. A. Fortune, A. J. Compston, A. Gondarenko, F. Meng, X. Chen, G. T. Reed, and R. Nicolaescu, "A universal 3D imaging sensor on a silicon photonics platform," *Nature* **590**, 256-261 (2021).

[15] A. Hänsel, and M. J. R. Heck, "Opportunities for photonic integrated circuits in optical gas sensors," *Journal of Physics: Photonics* **2**, 012002 (2020).

[16] D. Benedikovic, L. Virot, G. Aubin, J.-M. Hartmann, F. Amar, X. Le Roux, C. Alonso-Ramos, É. Cassan, D. Marris-Morini, J.-M. Fédéli, F. Boeuf, B. Szelag, and L. Vivien, "Silicon-germanium receivers for short-wave-infrared optoelectronics and communications," *Nanophotonics* **10**(3), 1059-1079 (2021).

[17] H. Tran, W. Du, S. A. Ghetmiri, A. Mosleh, G. Sun, R. A. Soref, J. Margetis, J. Tolle, B. Li, H. A. Naseem, and S.-Q. Yu, “Systematic study of $Ge_{1-x}Sn_x$ absorption coefficient and refractive index for the device applications of Si-based optoelectronics,” *Journal of Applied Physics* **119**, 103106 (2016).

[18] S. Luryi, A. Kastalsky, and J. Bean, “New infrared detector on a silicon chip,” *IEEE Transactions on Electron Devices* **31**(9), pp. 1135-1139 (1984).

[19] M. T. Currie, S. B. Samavedam, T. A. Langdo, C. W. Leitz, and E. A. Fitzgerald, “Controlling threading dislocation densities in Ge on Si using graded SiGe layers and chemical-mechanical polishing,” *Applied Physics Letters* **72**(14), 1718 (1998).

[20] Y. Bogumilowicz, J. M. Hartmann, F. Laugier, G. Rolland, T. Billon, N. Cherkashin, and A. Claverie, “High-temperature growth of very high germanium content SiGe virtual substrates,” *Journal of Crystal Growth* **290**(2), pp. 523-531 (2006).

[21] D. J. Eaglesham, and M. Cerullo, “Low-temperature growth of Ge on Si(100),” *Applied Physics Letters* **58**(20), 2276 (1991).

[22] H.-C. Luan, D. R. Lim, K. K. Lee, K. M. Chen, J. G. Sandland, K. Wada, and L. C. Kimerling, “High-quality Ge epilayers on Si with low threading-dislocation densities,” *Applied Physics Letters* **75**(19), 2909 (1999).

[23] J. M. Hartmann, A. Abbadie, N. Cherkashin, H. Grampeix, and L. Clavelier, “Epitaxial growth of Ge thick layers on nominal and 6° off Si(001); Ge surface passivation by Si,” *Semiconductor Science and Technology* **24**(5), 055002 (2009).

[24] A. Nayfeg, C. O. Chui, and K. C. Saraswat, “Effects of hydrogen annealing on heteroepitaxial-Ge layers on Si: Surface roughness and electrical quality,” *Applied Physics Letters* **85**, 2815 (2004).

[25] S. Kobayashi, Y. Nishi, and K. C. Saraswat, “Effects of isochronal hydrogen annealing on surface roughness and threading dislocation density of epitaxial Ge films grown on Si,” *Thin Solid Films* **518**(6), pp. S136-S139 (2010).

[26] K. H. Lee, S. Bao, B. Wang, C. Wang, S. F. Yoon, J. Michel, E. A. Fitzgerald, and C. S. Tan, “Reduction of threading dislocation density in Ge/Si using a heavily As-doped Ge seed layer,” *AIP Advances* **6**, 025028 (2016).

[27] S. G. Thomas, S. Bharatan, R. E. Jones, R. Thoma, T. Zirkle, N. V. Edwards, R. Liu, X. D. Wang, Q. Xie, C. Rosenblad, J. Ramm, G. Isella, and H. von Känel, “Structural characterization of thick, high-quality epitaxial Ge on Si substrates

grown by low-energy plasma-enhanced chemical vapor deposition," *Journal of Electronic Materials* **32**, pp. 976-980 (2003).

[28] H. Ye, and J. Yu, "Germanium epitaxy on silicon," *Science and Technology of Advanced Materials* **15**(2), 024601 (2014).

[29] Y. M. Haddara, P. Ashburn, and D.M. Bagnall, "Silicon-germanium: properties, growth and applications," in Springer Handbook of Electronic and Photonic Materials. Springer Bandbooks (2017).

[30] J. Taraci, J. Tolle, J. Kouvetakis, M. R. McCartney, D. J. Smith, J. Menendez, and M. A. Santana, "Simple chemical routes to diamond-cubic germanium-tin alloys," *Applied Physics Letters* **78**, 3607 (2001).

[31] M. Bauer, J. Taraci, J. Tolle, A.V. G. Chizmeshya, S. Zollner, D. J. Smith, J. Menendez, C. Hu, and J. Kouvetakis, "Ge-Sn semiconductors for band-gap and lattice engineering," *Applied Physics Letters* **81**, 2992 (2002).

[32] R. Roucka, J. Tolle, C. Cook, A. V. G. Chizmeshya, and J. Kouvetakis, "Versatile buffer layer architectures based on Ge1-xSnx alloys," *Applied Physics Letters* **86**, 191912s (2005).

[33] F. Gencarelli, B. Vincent, L. Souriau, O. Richard, W. Vandervorst, R. Loo, M. Caymax, and M. Heyns, "Low-temperature Ge and GeSn Chemical Vapor Deposition using Ge_2H_6," *Thin Solid Films* **520(**8), pp. 3211-3215 (2012).

[34] J. Margetis, S. A. Chetmiri, W. Du, B. R. Conley, A. Mosleh, R. A. Soref, G. Sun, L. Domulevicz, H. A. Naseem, S.-Q. Yu, and J. Tolle, "Growth and Characterization of Epitaxial Ge1-xSnx Alloys and Heterostructures Using a Commercial CVD System," *ECS Transactions* **64**(6), pp. 711-720 (2014).

[35] S. Su, W. Wang, B. Cheng, G. Zhang, W. Hu, C. Xue, Y. Zuo, and Q. Wang, "Epitaxial growth and thermal stability of Ge1-xSnx alloys on Ge-buffered Si(001) substrates," *Journal of Crystal Growth* **317**(1), pp. 43-46 (2011).

[36] M. Oehme, D. Buca, K. Kostecki, S. Wirths, B. Holländer, E. Kasper, and J. Schulze, "Epitaxial growth of highly compressively strained GeSn alloys up to 12.5% Sn," *Journal of Crystal Growth* **384**, pp. 71-76 (2013).

[37] P. L. de Guevara, A. G. Rodríguez, H. Navarro-Contreras, and M. A. Vidal, "$Ge_{1-x}Sn_x$ alloys pseudomorphically grown on Ge(001)," *Applied Physics Letters* **83**, 4942 (2003).

[38] J. Zheng, L. Li, T. Zhou, Y. Zuo, C. Li, B. Cheng, and Q. Wang, "Growth of Crystalline $Ge_{1-x}Sn_x$ Films on Si (100) by Magnetron Sputtering," *ECS Solid State Letters* **3(**9), P111 (2014).

[39] M. Miyao, and T. Sadoh, “Novel growth techniques of group-IV based semiconductors on insulator for next-generation electronics,” *Japanese Journal of Applied Physics* **56**, 05DA06 (2017).

[40] S. Zaima, O. Nakatsuka, N. Taoka, M. Kurosawa, W. Takeuchi, and M. Sakashita, “Growth and applications of GeSn-related group-IV semiconductor materials,” *Science and Technology of Advanced Materials* **16**, 043502 (2015).

[41] S. Ghosh, K.-C. Lin, C.-H. Tsai, K. H. Lee, Q. Chen, B. Son, B. Mukhopadhyay, C. S. Tan, and G.-E. Chang, “Resonant-cavity-enhanced responsivity in germanium-on-insulator photodetectors,” *Optics Express* **28**(16), 23739-23747 (2020).

[42] B.-J. Huang, J.-H. Lin, H. H. Cheng, and G-E. Chang, “GeSn resonant-cavity-enhanced photodetectors on silicon-on-insulator platforms,” *Optics Letters* **43(**6), 1215-1218 (2018).

[43] B.-J. Huang, C.-Y. Chang, Y.-D. Hsieh, R. A. Soref, G. Sun, H.-H. Cheng, and G.-E. Chang, “Electrically injected GeSn Vertical-Cavity Surface Emitters on Silicon-on-Insulator Platforms,” *ACS Photonics* **6**, 1931-1938 (2019).

[44] U. Younis, X. Luo, B. Dong, L. Huang, S. K. Vanga, A. E.-J. Kim, P. G.-Q. Lo, C. Lee, A. A. Bettiol, and K.-W. Ang, “Towards low-loss waveguides in SOI and Ge-on-SOI for mid-IR sensing,” *Journal of Physics Communications* **2**(4), 045029 (2018).

[45] W. Li, P. Anantha, K. H. Lee, H. D. Qiu, X. Guo, S. C. K. Goh, L. Zhang, H. Wang, R. A. Soref, and C. S. Tan, “Spiral Waveguides on Germanium-on-Silicon Nitride Platform for Mid-IR Sensing Applications,” *IEEE Photonics Journal* **10**(3), 2201107 (2018).

[46] R. E. Camacho-Aguilera, Y. Cai, N. Patel, J. T. Bessette, M. Romagnoli, L. C. Kimerling, and J. Michel, “An electrically pumped germanium laser,” *Optics Express* **20**(10), 11316-11320 (2012).

[47] Y. Zhou, Y. Miao, S. Ojo, H. Tran, G. Abernathy, J. M. Grant, S. Amoah, G. Salamo, W. Du, J. Liu, J. Margetis, J. Tolle, Y.-H. Zhang, G. Sun, R. A. Soref, B. Li, and S.-Q. Yu, “Electrically injected GeSn lasers on Si operating up to 100 K,” *Optica* **7**(8), 924-928 (2020).

[48] A. Elbaz, D. Buca, N. von den Driesch, K. Pantzas, G. Patriarche, N. Zerounian, E. Herth, X. Checoury, S. Sauvage, I. Sagnes, A. Foty, R. Ossikovski, J.-M. Hartmann, F. Boeuf, Z. Ikonic, P. Boucaud, D. Grǜtzmacher, and M. E.

Kurdi, “Ultra-low-threshold continuous-wave and pulsed lasing in tensile-strained GeSn alloys,” *Nature Photonics* **14**, 375-382 (2020).

[49] K. H. Lee, S. Bao, G. Y. Chong, Y. H. Tan, E. A. Fitzgerald, and C. S. Tan, “Fabrication and characterization of germanium-on-insulator through epitaxy, bonding, and layer transfer,” *Journal of Applied Physics* **116**, 103506 (2014).

[50] H. Li, Y. X. Cui, K. Y. Wu, W. K. Tseng, H. H. Cheng, and H. Chen, “Strain relaxation and Sn segregation in GeSn epilayers under thermal treatment,” *Applied Physics Letters* **102**, 251907 (2013).

[51] Y.-C. Tai, P.-L. Yeh, S. An, H.-H. Cheng, M. Kim, and G.-E. Chang, “Strain-free GeSn nanomembranes enabled by transfer-printing techniques for advanced optoelectronic applications,” *Nanotechnology* **31**, 445301 (2020).

[52] S. Bao, Y. Wang, K. Lina, K. Zhang, B. Wang, W. A. Sasangka, K. E. K. Lee, S. J. Chua, J. Michel, E. Fitzgerald, C. S. Tan, and K. H. Lee, “A review of silicon-based wafer bonding processes, an approach to realize the monolithic integration of Si-CMOS and III-V-on-Si wafers,” *Journal of Semiconductors* **42**, 023106 (2021).

[53] S. Xu, K. Han, Y.-C. Huang, K. H. Lee, Y. Kang, S. Masudy-Panah, Y. Wu, D. Lei, Y. Zhao, H. Wang, C. S. Tan, X. Gong, and Y.-C. Yeo, “Integrating GeSn photodiode on a 200 mm Ge-on-insulator photonics platform with Ge CMOS devices for advanced OEIC operating at 2 μm band,” *Optics Express* **27**(19), 26924-26939 (2019).

[54] K. R. Khiangte, J. S. Rathore, J. Schmidt, H. J. Osten, A. Laha, and S. Mahapatra, “Wafer-scale all-epitaxial GeSn-on-insulator on Si(111) by molecular beam epitaxy,” *Journal of Physics D: Applied Physics* **51**, 32LT01 (2018).

[55] J. N. Shive, “The Properties of Germanium Phototransistors,” *Journal of the Optical Society of America* **43**(4), pp. 239-244 (1953).

[56] H. Melchior, and W. T. Lynch, “Signal and Noise Response of High Speed Germanium Avalanche Photodiodes,” *IEEE Transactions on Electron Devices* **13**(12), 829-838 (1966).

[57] S. B. Samavedam, M. T. Currie, T. A. Langdo, and E. A. Fitzgerald, “High-quality germanium photodiodes integrated on silicon substrates using optimized relaxed graded buffers,” *Applied Physics Letters* **73**, 2125 (1998).

[58] L. Colace, G. Masini, and G. Assanto, “Efficient high-speed near-infrared Ge photodetectors integrated on Si substrates,” *Applied Physics Letters* **76**, 1231 (2000).

[59] S. Famà, L. Colace, G. Masini, G. Assanto, and H.-C. Luan, "High performance germanium-on-silicon detectors for optical communications," *Applied Physics Letters* **81**, 586 (2002).

[60] S. Klinger, M. Berroth, M. Kaschel, M. Oehme, and E. Kasper, "Ge-on-Si p-i-n Photodiodes With a 3-dB Bandwidth of 49 GHz," *IEEE Photonics Technology Letters* **21**(13), 920-922 (2009).

[61] P. Vines, K. Kuzmenko, J. Kirdoda, D. C. S. Dumas, M. M. Mirza, R. W. Millar, D. J. Paul, and G. S. Buller, "High performance planar germanium-on-silicon single-photon avalanche diode detectors," *Nature Communications* **10**, 1086 (2019).

[62] H.-Y. Xue, C.-L. Xue, B.-W. Cheng, Y.-D. Yu, and Q.-M. Wang, "High-Saturation-Power and High-Speed Ge-on-SOI p-i-n Photodetectors," *IEEE Electron Device Letters* **31**(7), 701-703 (2010).

[63] H. Cansizoglu, C. Bartolo-Perez, Y. Gao, E. P. Devine, S. Ghandiparsi, K. G. Polat, H. H. Mamtaz, T. Yamada, A. F. Elrefaie, S.-Y. Wang, and M. S. Islam, "Surface-illuminated photon-trapping high-speed Ge-on-Si photodiodes with improved efficiency up to 1700 nm," *Photonics Research* **6**(7), 734-742 (2018).

[64] J. Song, S. Yuan, C. Cui, Y. Wang, Z. li, A. X. Wang, C. Zeng, and J. Xia, "High-efficiency and high-speed germanium photodetector enabled by multiresonant photonic crystal," *Nanophotonics* **10**, 1081-1087 (2020).

[65] X. Li, L. Peng, Z. Liu, X. Liu, J. Zheng, Y. Zuo, C. Xue, and B. Cheng, "High-power back-to-back dual-absorption germanium photodetector," *Optics Letters* **45**(6), 1358-1361 (2020).

[66] Y. Lin, K. H. Lee, S. Bao, X. Guo, H. Wang, J. Michel, and C. S. Tan, "High-efficiency normal-incidence vertical p-i-n photodetectors on a germanium-on-insulator platform," *Photonics Research* **5**(6), 702-709 (2017).

[67] Y. Lin, D. Ma, R.-T. Wen, K. H. Lee, X. Guo, J. Zhou, H. Wang, C. S. Tan, and J. Michel, "Uniformly Tensile-strained Germanium Enabled by a Recessed Nitride Stressor for Efficient Integrated Photodetectors at Longer Wavelengths," *In conference on Lasers and Electro-Optics, OSA Technical Digest (Optical Society of America)*, STh40.2 (2019).

[68] G.-E. Chang, S.-Q. Yu, J. Liu, H. H. Cheng, R. A. Soref, and G. Sun, "Achievable Performance of Uncooled Homojunction GeSn Mid-infrared Photodetectors," *IEEE Journal of Selected Topics in Quantum Electronics*, DOI:10.1109/JSTQE.2021.3065204 (2021).

[69] S. Su, B. Cheng, C. Xue, W. Wang, Q. Cao, H. Xue, W. Hu, G. Zhang, Y. Zuo, and Q. Wang, "GeSn p-i-n photodetector for all telecommunication bands detection," *Optics Express* **19**(7), 6400-6405 (2011).

[70] K. Ye, W. Zhang, M. Oehme, M. Schmid, M. Gollhofer, K. Kostecki, D. Widmann, R. Körner, E. Kasper, and J. Schulze, "Absorption coefficients of GeSn extracted from PIN photodetector response," *Solid-State Electronics* **110**, 71-75 (2015).

[71] B. R. Conley, Y. Zhou, A. Mosleh, S. A. Ghetmiri, W. Du, R. A. Soref, G. Sun, J. Margetis, J. Tolle, H. A. Nassem, and S.Q. Yu, "Infrared spectral response of a GeSn p-i-n photodiode on Si," *11th International Conference on Group IV Photonics (GFP)*, 14760980 (2014).

[72] C. Fang, Y. Liu, Y. Wang, J. Wu, G. Han, Y. Shao, J. Zhang, and Y. Hao, "Buffer-free GeSn with High Relaxation Degree Grown on Si(001) Substrate for Photodetection," *IEEE Photonics Journal* **10**(6), 5501909 (2018).

[73] T. Pham, W. Du, H. Tran, J. Margetis, J. Tolle, G. Sun, R. A. Soref, H. A. Naseem, B. Li, and S.-Q. Yu, "Systematic study of Si-based GeSn photodiodes with 2.6 μm detector cutoff for short-wave infrared detection," *Optics Express* **24**(5), 4519-4531 (2016).

[74] Y. Dong, W. Wang, D. Lei, X. Gong, Q. Zhou, S. Y. Lee, W. K. Loke, S.-F. Yoon, E. S. Tok, G. Liang, and Y.-C. Yeo, "Suppression of dark current in germanium-tin on silicon p-i-n photodiode by a silicon surface passivation technique," *Optics Express* **23**(14), 18611-18619 (2015).

[75] W. Wang, D. Lei, Y.-C. Huang, K. H. Lee, W.-K. Loke, Y. Dong, S. Xu, C. S. Tan, H. Wang, S.-F. Yoon, X. Gong, and Y.-C. Yeo, "High-performance GeSn photodetector and fin-field-effect transistor (FinFET) on an advanced GeSn-on-insulator platform," *Optics Express* **26**(8), 10305-10314 (2018).

[76] S. Xu, W. Wang, Y.-C. Huang, Y. Dong, S. Masudy-Panah, H. Wang, X. Gong, and Y.-C. Yeo, "High-speed photo detection at two-micron-wavelength: technology enablement by GeSn/Ge multiple-quantum-well photodiode on 300 mm Si substrate," *Optics Express* **27**(4), 5798-5813 (2019).

[77] C.-H. Tan, B.-J. Huang, R. A. Soref, G. Sun, H. H. Cheng, and G.-E. Chang, "GeSn resonant-cavity-enhanced photodetectors for efficient photodetection at the 2 μm wavelength band," *Optics Letters* **45**(6), 1463-1466 (2020).

[78] H. Zhou, S. Xu, Y. Lin, Y.-C. Huang, B. Son, Q. Chen, X. Guo, K. H. Lee, S. C. K. Goh, X. Gong, and C. S. Tan, "High-efficiency GeSn/Ge multiple-quantum-

well photodetectors with photon-trapping microstructures operating at 2 μm," *Optics Express* **28**(7), 10280-10293 (2020).

[79] Thorlabs. Ge Photodiode: FDG03. [Online]. Available: https://www.thorlabs.de/drawings/de9bb1b30ddedb94-C9E9A63EB4E8-C68C-A0D7654AD574955B/FDG03-SpecSheet.pdf (2018).

[80] M. B. Gonzalez, E. Simoen, G. Eneman, B. D. Jaeger, G. Wang, R. Loo, and C. Claeys, "Defect assessment and leakage control in Ge junctions," *Microelectronic Engineering* **125**, 33-37 (2014).

[81] B. Son, Y. Lin, K. H. Lee, and C. S. Tan, "Dark Current Analysis of Vertical p-i-n Photodetectors on a Germanium-on-Insulator Platform," *2019 IEEE 16th International Conference on Group IV Photonics (GFP)*, pp. 1-2 (2019).

[82] H. Chen, P. Verheyen, P. D. Heyn, G. Lepage, J. D. Coster, S. Balakrishnan, P. Absil, G. Roelkens, and J. V. Campenhout, "Dark current analysis in high-speed germanium p-i-n waveguide photodetectors," *Journal of Applied Physics* **119**, 213105 (2016).

[83] N. A. DiLello, D. K. Johnstone, and J. L. Hoyt, "Characterization of dark current in Ge-on-Si photodiodes," *Journal of Applied Physics* **112**, 054506 (2012).

[84] M. B. Gonzalez, G. Eneman, G. Wang, B. De Jaeger, E. Simoen, and C. Claeys, "Analysis of the Temperature Dependence of Trap-Assisted Tunneling in Ge pFET Junctions," *Journal of Electrochemical Society* **158**(10), H955-960 (2011).

[85] E. Simoen, F. D. Stefano, G. Eneman, B. D. Jaeger, C. Claeys, and F. Crupi, "On the Temperature and Field Dependence of Trap-Assisted Tunneling Current in Ge p+n Junctions," *IEEE Electron Device Letters* **30**(5), 562-564 (2009).

[86] G. Eneman, M. B. Gonzalez, G. Hellings, B. D. Jaeger, G. Wang, J. Mitard, K. D. Meyer, C. Claeys, M. Meuris, M. M. Heyns, T. Y. Hoffmann, and E. Simoen, "Trap-Assisted Tunneling in Deep-Submicron Ge PFET Junctions," *ECS Transactions* **28**(5), 143-152 (2010).

[87] A. Ghosh, M. B. Clavel, P. D. Nguyen, M. A. Meeker, G. A. Khodaparast, R. J. Bodnar, and M. K. Hudait, "Growth, structural, and electrical properties of germanium-on-silicon heterostructure by molecular beam epitaxy," *AIP Advances* **7**, 095214 (2017).

[88] D. Kuzum, T. Krishnamohan, A. J. Pethe, A. K. Okayay, Y. Oshima, Y. Sun, J. P. McVittie, P. A. Pianetta, P. C. McIntyre, and K. C. Saraswat, "Ge-Interface

Engineering With Ozone Oxidation for Low Interface-State Density," *IEEE Electron Device Letters* **29**(4), 328-330 (2008).

[89] R. Zhang, T. Iwasaki, N. Taoka, M. Takenaka, and S. Takagi, “Al2O3/GeOx/Ge gate stacks with low interface trap density fabricated by electron cyclotron resonance plasma postoxidation,” *Applied Physics Letters* **98**, 112902 (2011).

[90] J. Kang, R. Zhang, M. Takenaka, and S. Takagi, “Suppression of dark current in GeOx-passivated germanium metal-semiconductor-metal photodetector by plasma post-oxidation,” *Optics Express* **23**(13), 16967-16976 (2015).

[91] Y. Xu, G. Han, H. Liu, Y. Wang, Y. Liu, J. Ao, and Y. Hao, “Ge pMOSFETs with GeOx Passivation Formed by Ozone and Plasma Post Oxidation,” *Nanoscale Research Letters* **14**, 126 (2019).

[92] R. D. Mahyavanshi, G. Kalita, A. Ranade, P. Desai, M. Kondo, T. Dewa, and M. Tanemura, "Photovoltaic Action With Broadband Photoresponsivity in Germanium-MoS2 Ultrathin Heterojunction," *IEEE Transactions on Electron Devices* **65**(10), 4434-4440 (2018).

[93] L. Virot, D. Benedikovic, B. Szelag, C. Alonso-Ramos, B. Karakus, J. Hartmann, X. Le Roux, P. Crozat, E. Cassan, D. Marris-Morini, C. Baudot, F. Boeuf, J. Fédéli, C. Kopp, and L. Vivien, "Integrated waveguide PIN photodiodes exploiting lateral Si/Ge/Si heterojunction," *Optics Express* **25**(16), 19487-19496 (2017).

[94] G. Isella, J. Osmond, M. Kummer, R. Kaufmann, and H. von Känel, “Heterojunction photodiodes fabricated from Ge/Si (100) layers grown by low-energy pasma-enhanced CVD,” *Semiconductor Science and Technology* **22**, S26-S28 (2007).

[95] Z. Liu, F. Yang, W. Wu, H. Cong, J. Zheng, C. Li, C. Xue, B. Cheng, and Q. Wang, "48 GHz High-Performance Ge-on-SOI Photodetector With Zero-Bias 40 Gbps Grown by Selective Epitaxial Growth," *Journal of Lightwave Technology* **35**, 5306-5310 (2017).

[96] K. H. Lee, S. Bao, G. Y. Chong, Y. H. Tan, E. A. Fitzgerld, and C. S. Tan, “Defects reduction of Ge epitaxial film in a germanium-on-insulator wafer by annealing in oxygen ambient,” *APL Materials* **3**, 016102 (2015).

[97] Y. Wang, B. Wang, D. F. S. Eow, J. Michel, K. E. K. Lee, S. F. Yoon, E. A Fitzgerald, C. S. Tan, and K. H. Lee, “Performance of AlGaInP LEDs on silicon

substrates through low threading dislocation density (TDD) germanium buffer layer," *Semiconductor Science and Technology* **33**, 104004 (2018).

[98] D. Benedikovic, L. Virot, G. Aubin, J.-M. Hartmann, F. Amar, B. Szelag, X. L. Roux, C. Alonso-Ramos, P. Crozat, É. Cassan, D. Marris-Morini, C. Baudot, F. Boeuf, J.-M. Fédéli, C. Kopp, and L. Vivien, "Comprehensive Study on Chip-Integrated Germanium Pin Photodetectors for Energy-Efficient Silicon Interconnects," *IEEE Journal of Quantum Electronics* **56**(1), pp. 1-9 (2020).

[99] Y. Lin, B. Son, K. H. Lee, J. Michel, and C. S. Tan, "Sub-mA/cm^2 Dark Current Density, Buffer-Less Germanium (Ge) Photodiodes on a 200-mm Ge-on-Insulator Substrate," *IEEE Transactions on Electron Devices* **68**(4), 1730-1737 (2021).

[100] Y. Lin, "Quantum efficiency enhancement of germanium-on-insulator photodetectors for integrated photonics on silicon," PhD dissertation, Nanyang Technological University (2019).

[101] Q. Zhang, N. Wu, T. Osipowicz, L. K. Bera, and C. Zhu, "Formation and Thermal Stability of Nickel Germanide on Germanium Substrate," *Japanese Journal of Applied Physics* **44**(45), 1389-1391 (2005).

[102] S. Zhum, M. B. Yu, G. Q. Io, and D. L. Kwong, "Enhanced thermal stability of nickel germanide on thin epitaxial germanium by adding an ultrathin titanium layer," *Applied Physics Letters* **91**, 051905 (2007).

[103] L. Zhou, X. Wang, X. Ma, K. Han, Y. Wang, J. Xiang, H. Yang, J. Zhang, C. Zhao, T. Ye, and W. Wang, "Identification of interfacial defects in a Ge gate stack based on ozone passivation," *Semiconductor Science and Technology* **33**, 115005 (2018).

[104] X. Wang, J. Xiang, W. Wang, Y. Xiong, J. Zhang, and C. Zhao, "Investigation on the dominant key to achieve superior Ge surface passivation by GeOx based on the ozone oxidation," *Applied Surface Science* **357**, 1857-1862 (2015).

[105] Z. Zhao, J. Zhang, X. Wang, S. Wei, C. Zhao, and W. Wang, "Angle-resolved x-ray photoelectron spectroscopy study of GeOx growth by plasma post-oxidation," *Chinese Physics B* **26**(10), 108201 (2017).

[106] F. Suo, J. Tong, L. Qian, and D. H. Zhang, "Study of dark current in mid-infrared InAsSb-based hetero n-i-p photodiode," *Journal of Physics D; Applied Physics* **51**, 275102 (2018).

[107] X. Ma, Y. Huang, J. Fei, Q. Chen, T. Liu, K. Liu, X. Duan, X. Yan, and X. Ren, “Analysis of dark current considering trap-assisted tunneling mechanism for In GaAs PIN photodetectors,” *Optical and Quantum Electronics* **49**, 407 (2017).

[108] J. Kang, R. Zhang, M. Takenaka, and S. Takagi, “Suppression of dark current in GeOx-passivated germanium metal-semiconductor-metal photodetector by plasma post-oxidation,” *Optics Express* **23**(13), 16967-16976 (2015).

[109] P. Chakrabarti, A. Gawarikar, V. Mehta, and D. Garg, “Effect of Trap-assisted Tunneling (TAT) on the Performance of Homojunction Mid-Infrared Photodetectors based on InAsSb,” *Journal of Microwaves and Optoelectronics* **5**(1), ISSN 1516-7399 (2006).

[110] G. A. M. Hurkx, D. B. M. Klaassen, and M. P. G. Knuvers, “A new recombination model for device simulation including tunneling,” *IEEE Transactions on Electron Devices* **39**(2), 331-338 (1992).

[111] Z. Zhou, J. He, R. Wang, C. Li, and J. Yu, “Normal incidence p-i-n Ge heterojunction photodiodes on Si substrate grown by ultrahigh vacuum chemical vapor deposition,” *Optics Communications* **283**(18), 3404-3407 (2010).

[112] N. S. Patel, “Understanding Defects in Germanium and Silicon for Optoelectronic Energy Conversion,” Ph.D. Dissertation, Massachusetts Institute of Technology (2016).

[113] Y. Cai, “Materials Science and Design for Germanium Monolithic Light Source on Silicon,” Ph.D. Dissertation, Massachusetts Institute of Technology(2014).

[114] M. Schmid, M. Kaschel, M. Gollhofer, M. Oehme, J. Werner, E. Kasper, and J. Schulze, “Franz-Keldysh effect of germanium-on-silicon p-i-n diodes within a wide temperature range,” *Thin Solid Films* **525**, 110-114 (2012).

[115] H.-Y. Yu, S. Ren, W. S. Jung, A. K. Okyay, D. A. B. Miller, and K. C. Saraswat, "High-Efficiency p-i-n Photodetectors on Selective-Area-Grown Ge for Monolithic Integration," *IEEE Electron Device Letters* **30**(11), 1161-1163 (2009).

[116] J. Liu, D. D. Cannon, K. Wada, Y. Ishikawa, S. Jongthammanurak, D. T. Danielson, J. Michel, and L.C. Kimerling, “Tensile strained Ge p-i-n photodetectors on Si platform for C and L band telecommunications,” *Applied Physics Letters* **87**, 011110 (2005).

[117] D. E. Aspnes, and A. A. Studna, “Dielectric functions and optical parameters of Si, Ge, GaP, GaAs, GaSb, InP, InAs, and InSb from 1.5 to 6.0 eV,” *Physics Review B* **27**, 985 (1983).

[118] L. Colace, G. Assanto, D. Fulgoni, and L. Nash, "Near-Infrared p-i-n Ge-on-Si Photodiodes for Silicon Integrated Receivers," *Journal of Lightwave Technology* **26**(16), 2954-2959 (2008).

[119] C. Li, C. Xue, Z. Liu, B. Cheng, C. Li, and Q. Wang, "High-Bandwidth and High-Responsivity Top-Illuminated Germanium Photodiodes for Optical Interconnection," *IEEE Transactions on Electron Devices* **60**(3), 1183-1187 (2013).

[120] H.-Y. Xue, C.-L. Xue, B.-W. Cheng, Y.-D. Yu, and Q.-M. Wang, "Zero biased Ge-on-Si photodetector with a bandwidth of 4.72 GHz at 1,550nm," *Chinese Physics B* **18**(6), 2542 (2009).

[121] D. Suh, S. Kim, J. Joo, and G. Kim, "36-GHz High-Responsivity Ge Photodetectors Grown by RPCVD," *IEEE Photonics Technology Letters* **21**(10), 672-674 (2009).

[122] R. Zhang, X. Yu, M. Takenaka, and S. Takagi, "Impact of Postdeposition Annealing Ambient on the Mobility of Ge nMOSFETs With 1-nm EOT Al2O3/GeOx/Ge Gate-Stacks," *IEEE Transactions on Electron Devices* **63**(2), 558-564 (2016).

[123] X. Zhao, G. Wang, H. Lin, Y. Du, X. Luo, Z. Kong, J. Su, J. Li, W. Xiong, Y. Miao, H. Li, G. Guo, and H. H. Radamson, "High Performance p-i-n Photodetectors on Ge-on-Insulator Platform," *Nanomaterials* **11**(5), 1125 (2021).

[124] Y. Gao, H. C.ansizoglu, K. G. Polat, S. Ghandiparsi, A. Kaya, H. H. Mamtaz, A. S. Mayet, Y. Wang, X. Zhang, T. Yamada, E. P. Devine, A. F. Elrefair, S.-Y. Wang, and M. S. Islam, "Photon-trapping microstructures enable high-speed high-efficiency silicon photodiodes," *Nature Photonics* **11**, 301-308 (2017).

[125] L. Zhou, X. Yu, and J. Zhu, "Metal-Core/Semiconductor-Shell Nanocones for Broadband Solar Absorption Enhancement," *Nano Letters* **14**, 1093-1098 (2014).

[126] C. Beskici, "Extended short wavelength infrared FPA technology: status and trends," *Proceeding of SPIE 10540, Quantum Sending and Nano Electronics and Photonics XV*, 105400P (2018).

[127] S. Wirths, R. Geiger, N. von den Driesch, G. Mussler, T. Stoica, S. Mantl, Z. Ikonic, M. Luysberg, S. Chiussi, J. M. Hartmann,H. Sigg, J. Faist, D. Buca, and D. Grùtzmacher, "Lasing in direct-bandgap GeSn alloy grown on Si," *Nature Photonics* **9**, 88-92 (2015).

[128] M. Oehme, K. Kostecki, K. Ye, S. Bechler, K. Ulbricht, M. Schmid, M. Kaschel, M. Gollhofer, R. Körner, W. Zhang, E. Kasper, and J. Schulze, "GeSn-on-Si normal incidence photodetectors with bandwidths more than 40 GHz," *Optics Express* **22**(1), 839–846 (2014).

[129] S. Xu, Y.-C. Huang, K. H. Lee, W. Wang, Y. Dong, D. Lei, S. Masudy-Panah, C. S. Tan, X. Gong, and Y.-C. Yeo, "GeSn lateral p-i-n photodetector on insulating substrate," *Optics Express* **26**(13), 17312-17321 (2018).

[130] J. Aubin, J. M. Hartmann, A. Gassenq, J. L. Rouviere, E. Robin, V. Delaye, D. Cooper, N. Mollard, V. Reboud, and V. Calvo, "Growth and structural properties of step-graded, high Sn content GeSn layers on Ge," *Semiconductor Science and Technology* **32**(9), 094006 (2017).

[131] Y.-H. Miao, H.-Y. Hu, J.-J. Song, R.-X. Xuan, and H.-M. Zhang, "Effects of rapid thermal annealing on crystallinity and Sn surface segregation of $Ge_{1-x}Sn_x$ films on Si (100) and Si (111)," *Chinese Physics B* **26**, 127306 (2017).

[132] D. Lei, K. H. Lee, S. Bao, W. Wang, B. Wang, X. Gong, C. S. Tan, and Y.-C. Yeo, "GeSn-on-insulator substrate formed by direct wafer bonding," *Applied Physics Letters* **109**, 022106 (2016).

[133] A. Elbaz, R. Arefin, E. Sakat, B. Wang, E. Herth, G. Patriarche, A. Foti, R. Ossikovski, S. Sauvage, X. Checoury, K. Pantzas, I. Sagnes, J. Chrétien, L. Casiez, M. Bertrand, V. Calvo, N. Pauc, A. Chelnokov, P. Boucaud, F. Boeuf, V. Reboud, J.-M. Hartmann, and M. E. Kurdi, "Reduced Lasing Thresholds in GeSn Microdisk Cavities with Defect Management of the Optically Active Region," *ACS Photonics* **7**(10), 2713-2722 (2020).

[134] M. Oehme, M. Schmid, M. Kaschel, M. Gollhofer, D. Widmann, E. Kasper, and J. Schulze, "GeSn p-i-n detectors integrated on Si with up to 4% Sn," *Applied Physics Letters* **101**, 141110 (2012).

[135] H. V. Stanchu, A. V. Kuchuk, Y. I. Mazur, K. Pandey, F. M. D. Oliveira, M. Benamara, M. D. Teodoro, S.-Q. Yu, and G. J. Salamo, "Quantitative Correlation Study of Dislocation Generation, Strain Relief, and Sn Outdiffusion in Thermally Annealed GeSn Epilayers," *Crystal Growth and Design* **21**(3), 1666-1673 (2021).

[136] H. Li, Y. X. Cui, K. Y. Wu, W. K. Tseng, H. H. Cheng, and H. Chen, "Strain relaxation and Sn segregation in GeSn epilayers under thermal treatment," *Applied Physics Letters* **102**, 251907 (2013).

[137] C.-E. Tsai, F.-L. Lu, P.-S. Chen, and C. W. Liu, "Boron-doping induced Sn loss in GeSn alloys grown by chemical vapor deposition," *Thin Solid Films* **660**, 263-266 (2018).

[138] G. Dushaq, A. Nayfeh, and M. Rasras, "Metal-germanium-metal photodetector grown on silicon using low temperature RF-PECVD," *Optics Express* **25**, 32110-32119 (2017).

[139] J. Nicholls, S. Dimitrijev, P. Tanner, and J. Han, "Description and Verification of the Fundamental Current Mechanisms in Silicon Carbide Schottky Barrier Diodes," *Science Reports* **9**, 3754 (2019).

[140] X. Zhang, F. Li, C. Lù, X. Xie, Y. Li, and S. N. Mohammad, "High-temperature characteristics of AlxGa1-xN/GaN Schottky diodes," *Journal of Semiconductor* **30**(3), 034001 (2009).

[141] E. J. Miller, E. T. Yu, P. Waltereit, and J. S. Speck, "Analysis of reverse-bias leakage current mechanisms in GaN grown by molecular-beam epitaxy," *Applied Physics Letters* **84**, 55 (2004).

[142] Z. Li, W. Wang, N. C. Greenham, and C. R. McNeill, "Influence of nanoparticle shape on charge transport and recombination in polymer/nanocrystal solar cells," *Physical Chemistry Chemical Physics* **16**, 25684 (2014).

[143] I. Hwang, C. R. McNeill, and N. C. Greenham, "Drift-diffusion modeling of photocurrent transients in bulk heterojunction solar cells," *Journal of Applied Physics* **106**, 094506 (2009).

[144] R. McNeill, I. Hwang, and N. C. Greenham, "Photocurrent transients in all-polymer solar cells: Trapping and detrapping effects," *Journal of Applied Physics* **106**, 024507 (2009).

[145] L. Hu, X. Liu, S. Dalgleish, M. M. Matsushita, H. Yoshikawa, and K. Awaga, "Organic optoelectronic interfaces with anomalous transient photocurrent," *Journal of Materials Chemistry C* **3**, 5122-5135 (2015).

[146] Z. Li, G. Lakhwani, N. C. Greenham, and C. R. McNeill, "Voltage-dependent photocurrent transients of PTB7:PC70BM solar cells: Experiments and numerical simulation," *Journal of Applied Physics* **114**, 034502 (2013).

[147] F. Pezzoli, A. Giorgioni, D. Patchett, and M. Myronov, "Temperature-Dependent Photoluminescence Characteristics of GeSn Epitaxial Layers," *ACS Photonics* **3**, 2004-2009 (2016).

[148] S.-Q. Yu, S. A. Ghetmiri, W. Du, J. Margetis, Y. Zhou, A. Mosleh, S. Al-Kabi, A. Nazzal, G. Sun, R. A. Soref, J. Tolle, B. Li, and H. A. Naseem, "Si based GeSn light emitter: mid-infrared devices in Si photonics," *Proceeding of SPIE 9367, Silicon Photonics X*, 93670R (2015).

[149] S. V. Kondratenko, S. S. Derenko, Y. I. Mazur, H. Stanchu, A. V. Kuchuk, V. S. Lysenko, P. M. Lytvyn, S.-Q. Yu, and G. J. Salamo, "Impact of defects on photoexcited carrier relaxation dynamics in GeSn thin films," *Journal of Physics: Condensed Matter* **33**(6), 065702 (2021).

[150] T. Liu, L. Wang, G. Zhu, X. Hu, Z. Dong, Z. Zhong, Q. Jia, X. Yang, and Z. Jiang, "Dislocation-related photoluminescence of GeSn films grown on Ge (001) substrates by molecular bema epitaxy," *Semiconductor Science and Technology* **33**, 125022 (2018).

[151] S. Gupta, E. Simoen, R. Loo, Y. Shimura, C. Porret, F. Gencarelli, K. Paredis, H. Bender, J. Lauwaert, H. Vrielinck, and M. Heyns, "Electrical properties of extended defects in strain relaxed GeSn," *Applied Physics Letters* **113**, 022102 (2018).

[152] E. Rogowicz, J. Kopaczek, J. Kutrowska-Girzycka, M. Myronov, R. Kudrawiec, and M. Syperek, "Carrier Dynamics in Thin Germanium-Tin Epilayers," *ACS Applied Electronic Materials* **3**(1), 344-352 (2021).

[153] F. Pezzoli, F. Isa, G. Lsella, C. V. falub, T. Kreiliger, M. Salvalaglio, R. Bergamaschini, E. Grilli, M. Guzzi, H. von Känel, and L. Miglio, "Ge Crystals on Si Show Their Light," *Physics Review Applied* **1**, 044005 (2014).

[154] H. Wang, J. Zhang, G. Zhang ,Y. Chen, Y.-C. Huang, and X. Gong, "High-speed and high-responsivity p-i-n waveguide photodetector at a 2 μm wavelength with a $Ge_{0.92}Sn_{0.08}$/Ge multiple-quantum-well active layer," *Optics Letters* **46**, 2099-2102 (2021).

[155] C.-H. Tsai, K.-C. Lin, C.-Y. Cheng, K.-C. Lee, H. H. Cheng, and G.-E. Chang, "GeSn lateral p-i-n waveguide photodetectors for mid-infrared integrated photonics," *Optics Letters* **46**, 864-867 (2021).

[156] Y.-H. Huang, G.-E. Chang, H. Li, and H. H. Cheng, "Sn-based waveguide p-i-n photodetector with strained GeSn/Ge multiple-quantum-well active layer," *Optics Letters* **42**(9), 1652-1655 (2017).

[157] Y.-H. Peng, H. H. Cheng, V. I. Mashanov, and G.-E. Chang, "GeSn p-i-n waveguide photodetectors on silicon substrates," *Applied Physics Letters* **105**, 231109 (2014).

[158] X. Y. Li, J. Y. Wang, Y. F. Liu, J. J. chen, Y. Du, W. Wang, Y. Cai, J. P. Ma, and M. B. Yu, “Design of $Ge_{1-x}Sn_x$-on-Si waveguide photodetectors featuring high-speed high-sensitivity photodetection in the C- to U-bands,” *Applied Optics* **59**(25), 7646-7651 (2020).

[159] S. A. Ghetmiri, W. Du, B. R. Conley, A. Mosleh, A. Nazzal, G. Sun, R. A. Soref, J. Margetis, J. Tolle, H. A. Naseem, and S.-Q. Yu, “Shortwave-infrared photoluminescence from Ge1-xSn thin films on silicon,” *Journal of Vacuum Science & Technology B* **32**, 060601 (2014).

[160] A. Gassenq, L. Milord, J. Aubin, N. Pauc, K. Guilloy, J. Rothman, D. Rouchon, A. Chelnokov, J. M. Hartmann, V. Reboud, and V. Calco, “Raman spectral shift versus strain and composition in GeSn layers with 6%-15% Sn content,” *Applied Physics Letters* **110**, 112101 (2017).

[161] Y. Zhou, M. Ogawa, X. Han, and K. L. Wang, “Alleviation of Fermi-level pinning effect on metal/germanium interface by insertion of an ultrathin aluminum oxide,” *Applied Physics Letters* **93**, 202105 (2008).

[162] Y.-C. Fang, K.-Y. Chen, C.-H. Hsieh, C.-C. Su, and Y.-H. Wu, “N-MOSFETs Formed on Solid Phase Epitaxially Grown GeSn Film with Passivation by Oxygen Plasma Featuring High Mobility,” *ACS Applied Materials and Interfaces* **7**, 26374-26380 (2015).

[163] H. Fu, H. Chen, X. Huang, I. Baranowski, J. Montes, T.-H. Yang, and Y. Zhao, “A Comparative Study on the Electrical Properties of Vertical (201) and (010) β-Ga2O3 Schottky Barrier Diodes on EFG Single-Crystal Substrates,” *IEEE Transactions on Electron Devices* **65**(8), 3507-3513 (2018).

[164] C. Schilte-Braucks, E. Hofmann, S. Glass, N. von den Driesch, G. mussler, U. Breuer, J.-M. Hartmann, P. Zaumsell, T. Shröder, Q.-T. Zhao, S. Manti, and D. Buca, “Schottky barrier tuning via dopant segregation in NiGeSn-GeSn contacts,” *Journal of Applied Physics* **121**, 205705 (2017).

Author's Publications

Publications related to this thesis work.

Arsterisk (*) denotes equal contributions.

Journals

[1] **B. Son**, Y. Lin, K. H. Lee, J. Margetis, D. Kohen, J. Tolle, C. S. Tan, "Metal-semiconductor-metal photodetectors on a GeSn-on-insulator platform for the 2 μm applications," ***under review***.

[2] **B. Son**, L. Zhang, Y. Jung, H. Zhou, D. Nam, C. S. Tan, "Systematic Study on Photoexcited Carrier Dynamics Related to Defects in GeSn Films with low Sn Content at Room Temperature," *Semicond. Sci. Tech.* **36**(12), 125018 (2021).

[3] S. Wu, **B. Son**, L. Zhang, Q. Chen, H. Zhou, S. C. K. Goh, and C. S. Tan, "Effects of high-temperature thermal annealing on GeSn thin-film material and photodetector operating at 2μm," *Journal of Alloys and Compounds* **872**, 159696 (2021).

[4] **B. Son**, H. Zhou, Y. Lin, K. H. Lee, and C. S. Tan, "Gourd-shaped hole array germanium (Ge)-on-insulator photodiodes with remarkable responsivity and specific detectivity at 1,550 nm," *Optics Express* **29**(11), 16520-16533 (2021).

[5] Y. Lin*, **B. Son***, K. H. Lee, J. Michel, and C. S. Tan, "Sub-mA/cm^2 Dark Current Density, Buffer-less Germanium (Ge) Photodiodes on a 200-mm Ge-on-insulator Substrate," *IEEE Transactions on Electron Devices* **68**(4), pp. 1730-1737 (2021).

[6] H. Zhou, L. Zhang, J. Tong, S. Wu, **B. Son**, Q. Chen, D. H. Zhang, and C. S. Tan, "Surface plasmon enhanced GeSn photodetectors operating at 2 μm," *Optics Express* **29**(6), 8498-8509 (2021).

[7] C. K. Goh, L. L. Shiau, L. Zhang, **B. Son**, Q. Chen, J. Zhong, T. Salim, and C. S. Tan, "Monolithic Germanium-tin Pedestal Waveguide for Mid-infrared Applications," *IEEE Photonics Journal* **13**(2), 2500111 (2021).

[8] L. Yin, K. H. Lee, **B. Son**, and C. S. Tan, "Low-power and high-detectivity Ge photodiodes by in-situ heavy As doping during Ge-on-Si seed layer growth," *Optics Express* **29**(3), 2940-2952 (2020).

[9] S. Ghosh, K.-C. Lin, C.-H. Tsai, H. Kumar, Q. Chen, L. Zhang, **B. Son**, C. S. Tan, M. Kim, B. Mukhopadhyay, and G.-E. Chang, "Metal-Semiconductor-Metal GeSn Photodetectors on Silicon for Short-Wave Infrared Applications," *Micromachines* **11**(9), 795 (2020).

[10] S. Wu, L. Zhang, **B. Son**, Q. Chen, H. Zhou, and C. S. Tan, "Insights into the Origins of Guided Microtrenches and Microholes/rings from Sn Segregation in Germanium-Tin Epilayers," *The Journal of Physical Chemistry C* **124**(37), 20035-20045 (2020).

[11] **B. Son**, Y. Lin, K. H. Lee, Y. Wang, S. Wu, and C. S. Tan, "High speed and ultra-low dark current Ge vertical p-i-n photodetectors on an oxygen-annealed Ge-on-insulator platform with GeO_x surface passivation," *Optics Express* **28**(16), 23987-23990 (2020).

[12] S. Ghosh, K. C. Lin, C. H. Tsai, K. H. Lee, Q. Chen, **B. Son**, B. Mukhopadhyay, C. S. Tan, and G.-E. Chang, "Resonant-cavity-enhanced responsivity in germanium-on-insulator photodetectors," *Optics Express* **28**(16), 23739-23747 (2020).

[13] **B. Son**, Y. Lin, K. H. Lee, Q. Chen, and C. S. Tan, "Dark current analysis of germanium-on-insulator vertical p-i-n photodetectors with varying threading dislocation density," *Journal of Applied Physics* **127**(20), 203105 (2020).

[14] H. Zhou, S. Xu, Y. Lin, Y. C. Huang, **B. Son**, Q. Chen, X. Guo, K. H. Lee, S. C.-K. Goh, X. Gong, and C. S. Tan, "High-efficiency GeSn/Ge multiple-quantum-well photodetectors with photon-trapping microstructures operating at 2μm," *Optics Express* **28**(7), 10280-10293 (2020).

[15] Q. Chen, L. Zhang, H. Zhou, W. Li, **B. K. Son**, and C. S. Tan, “The effects of strain and composition on the conduction-band offset of direct band gap type-I GeSn/GeSnSi quantum dots for CMOS compatible mid-IR light source,” *Semiconductor Science and Technology* **35**(2), 025008 (2020).

Conferences

[1] H. Zhou, L. Zhang, S. Wu, Q. Chen, B. Son, C. S. Tan, “Plasmonic GeSn photodetectors for enhanced photo detection at 2 μm,” *2021 Conference on Lasers and Electro-Optics (CLEO)*, ATu1T. 5 (2021).

[2] H. Zhou, L. Zhang, J. Tong, S. Wu, Q. Chen, B. Son, D. H. Zhang, C. S. Tan, “High-efficiency plamon-enhanced GeSn photodetectors operating at 2 μm,” *2021 Conference on Lasers and Electro-Optics (CLEO)*, JW1A. 54 (2021).

[3] L. Zhang, Q. Chen, S. Wu, **B. Son**, K. H. Lee, G. Y. Chong, and C. S. Tan, “Growth and Characterizations of GeSn Films with High Sn Composition by Chemical Vapor Deposition (CVD) Using Ge2H6 and SnCl4 for Mid-IR Applications,” *ECS Transactions* **98**(5), 91 (2020).

[4] H. Zhou, S. Xu, Y. Lin, Y-C. Huang, **B. Son**, W. Li, X. Guo, L. Liu, K. H. Lee, X. Gong, and C. S. Tan, “High-Efficiency Photo Detection at 2 μm Realized by GeSn/Ge Multiple-Quantum-Well Photodetectors with Photon-Trapping Microstructure,” *2020 Conference on Lasers and Electro-Optics (CLEO)*, pp. 1-2 (2020).

[5] Q. Chen, L. Zhang, H. Zhou, W. Li, **B. K. Son**, and C. S. Tan, “Investigation of resonant-cavity-enhanced GeSn photodetectors in short-wavelength infrared regime,” *2019 IEEE 16th International Conference on Group IV Photonics (GFP)*, pp. 1-2 (2019).

[6] **B. Son**, Y. Lin, K. H. Lee, and C. S. Tan, “Dark current analysis of vertical pin photodetectors on a germanium-on-insulator platform,” *2019 IEEE 16th international Conference on Group IV Photonics (GFP)*, pp. 1-2 (2019).

[7] **B. Son**, Y. Lin, W. Li, K. H. Lee, J. Margetis, D. Kohen, J. Tolle, L. Zhang, T. G. Xin, H. Wong, and C. S. Tan, "Metal-semiconductor-metal photodetectors on a GeSn-on-insulator platform," *Proceeding of SPIE 10914, Optical Components and Materials XVI*, 109141A (2019).